# MAGNETORESISTANCE OF POLYMER DIODES IN PRESENCE OF OSCILLATING MAGNETIC FIELDS AT RADIO FREQUENCY

by

David P. Waters

A dissertation submitted to the faculty of
The University of Utah
in partial fulfillment of the requirements for the degree of

Doctor of Philosophy

in

Physics

Department of Physics and Astronomy

The University of Utah

December 2014

# The University of Utah Graduate School

## STATEMENT OF DISSERTATION APPROVAL

The following faculty members served as the supervisory committee chair and members for the dissertation of David P. Waters.

Dates at right indicate the members' approval of the dissertation.

| | | |
|---|---|---|
| Christoph Boehme | , Chair | 8/12/2014<br>Date Approved |
| Brian Saam | , Member | 8/12/2014<br>Date Approved |
| Dmytro Pesin | , Member | 8/12/2014<br>Date Approved |
| Benjamin Bromley | , Member | 8/12/2014<br>Date Approved |
| Ashutosh Tiwari | , Member | <br>Date Approved |

The dissertation has also been approved by Carleton DeTar

Chair of the Department of Physics and Astronomy

and by David Kieda, Dean of The Graduate School.

## ABSTRACT

This work focuses on the study of low-magnetic field (<10mT) magnetoresistance effects of organic polymer diodes based on the π-conjugated polymer MEH-PPV in presence of oscillating magnetic fields in the radio frequency range. In these conditions, the combination of static and ac fields can magnetic resonantly influence the electron-spin degree of freedom of localized charge-carrier states. As long as bipolar injection conditions influence the net current of the polymer diode, magnetic-resonance changes of the charge carrier spin state can affect spin-dependent charge carrier recombination rates and therefore the material's conductivity. Since the observed spin-dependent recombination currents are governed by the charge carrier pair's spin-permutation symmetry, magnetoresistance measurements under ac drive allow for the electrical detection of magnetic resonance under very low magnetic field conditions where inductive magnetic resonance detection schemes fail due to a lack of spin polarization. In this thesis, this effect was utilized for two effects.

Firstly, for the exploration of a magnetic resonance regime where the driving field $B_1$ approaches the same magnitude as the static magnetic field $B_0$. When $B_1$ approaches $B_0$, a regime where magnetic resonance effects become nonlinear emerges and interesting collective spin-phenomena occur. This includes spin-cooperativity, where the resonantly-driven spin ensemble assumes a macroscopically collective state. Experiments are presented that tested and confirmed previous theoretical predictions. When $B_1 \sim B_0$, the

emerging spin-cooperativity of recombining polaron pairs in organic semiconductors can be observed through magnetoresistance measurements. The experiments confirmed the theory in all aspects and demonstrated the emergence of the spin-Dicke effect.

Secondly, for the exploration of whether magnetic resonantly-controlled spin-dependent currents can be used for magnetometry of inhomogeneous magnetic fields. This work is a continuation of the previously introduced idea to utilize spin-dependent charge carrier recombination in organic semiconductors for an absolute low-magnetic field magnetometry that is robust against fluctuating environmental conditions. The work focuses on the measurement of magnetic field distributions in gradient magnetic fields. It is shown that organic semiconductor-based magnetic resonance magnetometers can reveal magnetic field distributions. However, this measurement approach can be compromised by inductive resonance artifacts introduced by the large-bandwidth RF stripline resonators needed to operate the magnetometer.

To my lovely wife, Sarah.

## TABLE OF CONTENTS

## LIST OF FIGURES

## ACKNOWLEDGEMENTS

As with any dissertation, the research and writing could not have been accomplished without the help of many others. In no particular order, I would like to take the time to acknowledge the help that I have received from many people during my time as a graduate student.

First of all, the time given by any advisor to a graduate student is incalculable. My advisor, Christoph Boehme, has proven this throughout the six years that I have been at the University of Utah. He allowed me to join his group without any knowledge of what I was or what I would accomplish. He led me through each project, helping me continue in the best direction and giving plenty of advice. When papers needed to be written or presentations to be prepared, Christoph has always been there to help me create the best possible result. Within this dissertation, his expertise and patience can be seen countless times, and this would not be possible without his guidance.

I would also like to thank the Boehme group as a whole for being a part of my learning process, both to past and present members. I would also like to recognize each group member or fellow graduate student who is on a paper of mine and explain the contributions that they provided. Within any interaction, there is always help that is provided that cannot be quantified, so for those of you that I mention, know that there is much more I thank you for and this is simply all I had room for.

To Hiroki Morishita, for creating the program to run the magnetometer setup. To Gajadhar, for setting up the low field setup and helping with the measurements that led to

Chapter 4 of this work. To Doug Baird, for ensuring a working glovebox and helping me learn how to make organic samples. To Marzieh Kavand, for the preparation of organic devices, especially the deuterated sample that allowed for some great measurements. To Kipp van Schooten, for advice and discussions about processes and theory and answering all the other questions I had. To Hans Malissa, for his help with the Matlab programming and overall low field setup help. For answering questions and giving guidance and advice. To Mark Limes, for his help with the Matlab program for Chapter 4, for countless discussions and advice about magnetic processes, and for his help with the Rabi oscillation measurements when nothing else was working. To Rachel Baarda, for helping in the clean room to speed up the processes and make templates faster. To Sang-Yun Lee, for training in the clean room and advice on my amorphous silicon project. To Will Baker, for all the help and advice and beginning my low-field measurement project.

For all of the added support with my papers and presentations and overall research, I would like to thank John Lupton.

I would also like the acknowledge the help of the entire Utah Nanofabrication staff, and especially Brian Baker, for all of their help with teaching and training of fabrication processes in order to create working templates and for fixing broken equipment as quickly as possible.

I would like to thank Brian Saam, Dmytro Pesin, Ben Bromley, and Ashutosh Tiwari for graciously participating on my supervisory committee and providing me with advice.

Although the advice and feedback with all of this research is very helpful, there is also the added support that comes from my family, who may not understand what I do

but care so much about how I am doing. For helping me through my time as a graduate student, I want to thank my mom and dad, for their endless love and support from beginning to end of this difficult process. I would also like to thank my sister, Sarah, not only for being supportive when I needed a friend, but also for her help learning how to use Adobe Illustrator and improving some of the figures in this document.

Finally, and especially, I want to thank my wife, Sarah, whose kindness and love motivated me to keep pushing on when everything seemed so difficult. I couldn't have done this without her help.

# CHAPTER 1

# INTRODUCTION

## 1.1 Magnetoresistance of condensed matter

In condensed matter systems, magnetoresistance defines a broad range of physical effects that account for conductivity changes when changes of the magnitude or the direction (or both) of externally applied magnetic fields occur. There is a broad range of magnetoresistance effects that occur in different materials [6-8], different semiconductor- [9-11] and conductor-device schemes [12], in different device geometries [13], and for different materials- and device-dimensionalities [14,15]. In general, any electric current response to magnetic field changes represents magnetoresistance. Historically, one of the first studies of magnetic field-induced conductivity effects goes back to William Thompson [16], who discovered that a magnetic field can influence the magnitude of an electric current via the Lorentz force. Since the Lorentz force depends on the mutual orientation of the current and the magnetic force, this first-discovered manifestation of magnetoresistance was highly anisotropic, nowadays referred to as anisotropic magnetoresistance (AMR). Related to this was the later work by Hall [17] who realized that an external magnetic field applied to a current also causes a transverse electric field. Possibly the most widely known aspect of this so-called Hall effect is the voltage that is caused by this electric field, the so-called Hall voltage. The Hall effect is in essence another expression of the same processes that cause AMR [17].

Since these early discoveries in the 19th century, many other manifestations of magnetoresistance have been found in metals and semiconductors. Not all of these are due to the interaction of the magnetic field with the angular momentum of the charge carriers. Many magnetoresistance phenomena are due to the interaction of the magnetic field with the magnetic dipolar moment, and thus the spin, of charge carriers. These spin-related magnetoresistance effects occur in spin-valves [18,19] and materials where spin-selection rules govern conductivity [20-22]. Others, such as magnetoresistance effects associated with the quantum Hall effect [23] and the fractional quantum Hall effect [24,25] do involve the angular momentum, but the dimensionality of the charge carrier motion has great significance as well.

Magnetoresistance gained interest [26] with the discovery of some technological applications. Giant magnetoresistance [19,27] and tunnel magnetoresistance [28] led to the development of magnetic memory [29-31] and, most importantly from a technological viewpoint, magnetoresistance-based hard disc-read heads, which have revolutionized computer technology. Current commercially available hard discs exceed storage densities of Tbit/in$^2$ [32] and such densities would be inconceivable without magnetoresistance-based spintronics devices. Magnetoresistance is present virtually any time an electric current exists in a condensed matter system. Knowing and understanding magnetoresistance is therefore important not only for technical application but also for scientific research, even if magnetoresistance itself is not the focus of research.

Much effort has been dedicated to the investigation of magnetoresistance effects involving charge transport in systems with delocalized charge carriers where band-mediated transport is dominant. This includes metals but also many semiconductors, e.g.,

crystalline silicon [33]. On the other hand, there has been comparatively little attention paid to magnetoresistance effects in systems where transport is governed by transitions through localized electronic states. These systems include many disordered semiconductors such as amorphous [20-22] and microcrystalline silicon [34,35], amorphous germanium [21,36], and derivatives of some of these materials like silicon rich silicon nitride [37] and others [12]. This group also includes the very broad range of organic semiconductors that encompasses thousands of different materials [38]. Many of these materials display very complex but also very pronounced magnetoresistance properties (with observed magnetoresistances of >10% at room temperature [39]), reflecting their overall structural and morphological complexity. Hence, since the first magneto-optoelectronic experiments showed photo-magnetoresistance [40] in 1967, the magnetoresistance of organic materials has evolved into a widely pursued research field.

## 1.2 Magnetoresistance of organic conductors and semiconductors

Over the past decades, there has been significant interest in the *magneto-optoelectronic* properties of organic semiconductor materials [11]. This also includes the observation of strong organic magnetoresistance responses [41-46]. Similarly, spin valves based on organic semiconductors have been reported [7,11,47-52], suggesting the existence of spin transport in these materials, and a number of innovative device concepts based on these effects have been proposed and demonstrated. Over the past decade, these research areas have formed the field of organic spintronics which generally deals with spin effects on electronic processes in organic materials [47,53,54]. With all of the excitement about this new research direction, one would expect that technical progress would come rapidly; however, there are still questions about the physical nature of the

fundamental processes responsible for these phenomena.

Magnetoresistance of organic semiconductors at low magnetic fields ($B < 10$ mT) is typically referred to in the literature as organic magnetoresistance (OMAR). In this context, the term "organic semiconductors" usually refers to electrically conducting hydrocarbon materials such as π-conjugated polymers [55,56], small molecules [48,57], and certain fullerene- [58] and carbon-nanotube [59,60] derivatives. Pure carbon compounds, including graphene, are usually not included as their electronic properties and their charge transport mechanisms differ profoundly. Most studies of these materials have taken place at low magnetic fields since the most pronounced conductivity changes occur within this regime. However, a few magnetoresistance studies conducted in the Tesla range have been published recently [61].

Figure 1.1 displays a measurement of the current in a polymer diode as function of an applied magnetic field. The details of the sample, its preparation, and the measurement procedures will be discussed in the following chapters. The data resemble the characteristic qualitative features of OMAR. A current minimum is occurring at small magnetic fields (<1mT) while the largest currents are attained when the applied magnetic field approaches the OMAR saturation regime beyond 10mT.

Many experimental OMAR studies found in the literature are phenomenological and conclusions drawn from these observations are hypothetical [62]. Because of this, there has been considerable controversy about the exact mechanisms through which the magnetic field controls conductivity in these materials [63]. While many of the existing hypothesis cannot be true (as they mutually contradict each other), there has been agreement throughout most of the existing work on OMAR about the involvement of

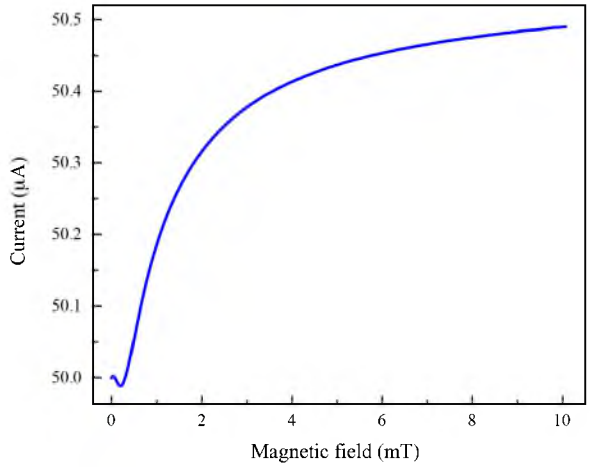


**Figure 1.1**. Plot of the absolute DC current of an MEH-PPV polymer diode in forward direction (bias 2.5 V) as a function of the applied magnetic field. This displayed data set resembles all characteristic features of OMAR. At very low magnetic field (< 0.5mT), the device current reaches a minimum beyond which the current increases with increasing magnetic field. Beyond 10mT, the OMAR effect approaches saturation. The magnetic field scales on which this characteristic OMAR behavior takes place are controlled by the magnitude of the local hyperfine fields in the given polymer material.

charge carrier spins (rather than orbital effects). Since models have been created from the existing phenomenological descriptions [64], OMAR measurements themselves are usually insufficient to exclude all models that do not account for the experimental observations. In most cases, this insufficiency is due to the ambiguities that arise from an overabundance of parameterization. Thus, the need for alternative experimental techniques to gain access to the nature of these spin-dependent electronic processes has arisen [63]. Magnetic resonance spectroscopy methods seem particularly well suited to provide the additional experimental information for the determination of the correct process. The most direct way to observe how electron spin states influence electric current is to manipulate these spin states in a very controlled manner (e.g., by use of electron spin resonance [ESR]) and to then observe how the electric current responds to

this manipulation. This experimental approach is typically referred to as electrically detected magnetic resonance (EDMR) spectroscopy. EDMR will play an important role in the work presented in the following.

At this time, there seems to be general consensus that charge transport in many organic semiconductors takes place through paramagnetic localized electronic states that have a polaronic nature [65]. In spite of this, there are still many unknowns about the qualitative and quantitative nature of transport and how it is controlled by spins [62,66,67]. In spin valve devices, spin transport in inorganic and crystalline materials has traditionally been investigated with Hanle effect measurements [68], where a spin current is measured as a magnetic field and is applied perpendicular to the polarization direction of injected spins. For organic spin valves, these measurements have been attempted, yet no Hanle effect has been observed [44,67,69,70].

Similarly, even the nature of elementary spin relaxation processes is not really understood for many paramagnetic species in organic materials [71]. Usually, in condensed matter systems, spin relaxation times can be measured by conventional, inductively-detected magnetic resonance experiments. In thin-film materials with weak spin-orbit coupling, which is what most organic semiconductors are, magnetic resonance spectroscopy is usually too insensitive due to its reliance on spin polarization, and since most paramagnetic systems have about the same Landé-factor, the different systems are difficult to resolve. Consequently, spin relaxation time measurements and estimates for the relevant paramagnetic centers in organic semiconductors are hard to obtain. Therefore, literature values are found to cover six to nine orders of magnitude [54,72,73] for the same spin relaxation process.

Arguably, the most significant challenge for this research field to overcome is the controversy about the fundamental nature of spin-dependent charge carrier transitions. The plethora of models that can be found in the literature [69,72] include single spin-½ processes [74], polaron pair recombination [75-85], bipolaron transport [69,86,87], triplet-exciton polaron recombination [43,88], trion processes [89], and triplet-triplet exciton annihilation [38]. This range of different hypotheses explaining identical phenomena provides little insight into the underlying mechanisms. Without intensive scrutiny with unambiguous experimental evidence that allows us to refute and therefore weed out models, progress within the research field will be limited.

As mentioned above, EDMR spectroscopy and similarly the optically detected magnetic resonance (ODMR) spectroscopy can provide important insights into the nature of spin-dependent processes. Both EDMR and ODMR experiments have been performed on organic semiconductors at least since the 1980s [80,89-99]. Most of these studies have been performed as adiabatic fields sweep experiments, which are continuous wave (cw) spectroscopies. Figure 1.2 displays data of a cwEDMR spectrum that was recorded under the same conditions as the data in Figure 1.1. It shows that in the presence of an AC magnetic field, $B_1$ that oscillates in the RF range, the OMAR function can change significantly at $B_0$ values that are close to the magnetic resonance condition when the RF photon energy $hf$, with $h$ being the Planck constant and $f$ the RF frequency, becomes equal to the Zeeman splitting of the charge carrier spin states $hf = g\mu_B B_0$.

One can see from Figure 1.2 that detection of spin-dependent processes influencing electrical transport and optical emission with regard to resolving different paramagnetic species and processes is straightforward with cwEDMR. However, similar

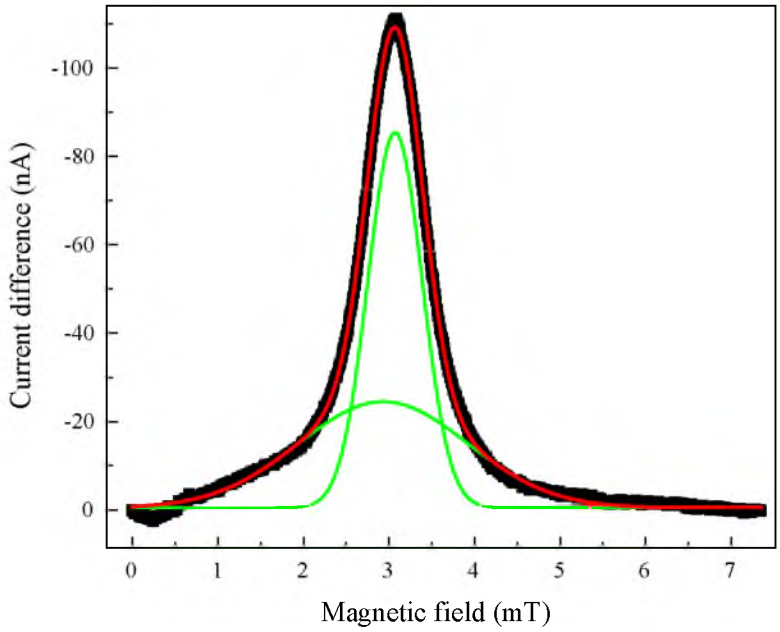


**Figure 1.2**. Plot of the absolute value of the change of the DC current of an MEH-PPV polymer diode, operated under identical conditions as for Figure 1.1, as a function of the applied magnetic field $B_0$ in the presence of an AC magnetic field $B_1$ that is perpendicular to $B_0$ and has a frequency of $f$ = 85MHz. This cwEDMR measurement reveals the magnetic resonant changes of charge carrier spins around $B_0$ = 3.03mT, corresponding to a Landé-factor of approximately 2. The data can be fit with two Gaussian broadened lines, shown as green lines, with a combined fit shown as the red line.

issues exist for these experiments as for conventional ESR spectroscopy and even direct magnetoresistance measurements. One issue is that for many of the existing models, there are just too many parameters involved to allow for an unambiguous discrimination of the different hypotheses that exist. In spite of the various attempts to identify the right models and refute the wrong models, these experiments have still left many questions unanswered. As an example, controversy comes from the resonance line-shapes of cwEDMR- and cwODMR-detected, spin-dependent signals. There are cases where several different, mutually contradicting models can all confirm the same data sets [69,80,100-103]. As a fit of the data in Figure 1.2 when a single Gaussian function

produces only weak agreement, we may be able to rule out a model which involves only a single spin-½ species. The data therefore provides proof that several spin species are involved. Good fits of these resonance lines are made with two Gaussian functions. However, since most other models involve various spin species (spin-pairs, bipolaron pairs, trions, triplet-polaron pairs) little insight has been gained from these cwEDMR and cwODMR experiments and many open questions have remained [44,69,71,104-106].

For some selected organic semiconductors such as PCBM and MEH-PPV, the controversy has been reduced significantly due to the application of transient, pulsed EDMR and ODMR. Here, magnetic resonance spectroscopy is combined with the time domain, an additional dimension that can greatly reduce ambiguity, especially when the time domain is short enough such that the observation of coherent spin propagation is possible. For instance, to probe the mechanisms behind spin-dependent processes, Rabi oscillations have been performed on PCBM [87,107] and MEH-PPV [1,62,106,108] devices. From the observed Rabi-frequency components and the observation of characteristic quantum mechanical effects such as spin-beat oscillations and their frequency domain analysis, clearer evidence for the nature of the involved spin-dependent processes can be obtained. These effects, first found for MEH-PPV by McCamey et al. [1] in 2010 and displayed in Figure 1.3, were the first unambiguous evidence for the involvement of pairs of two spins with s=½, since they refuted immediately all other model hypotheses. After this, similar effects were observed in blend materials involving MEH-PPV [87], which were attributed to unipolar transport, the so called bipolaron process. Thus, there is still an ongoing discussion about whether or not the two species with s=½ involved have identical or different charges [63]. Yet, at

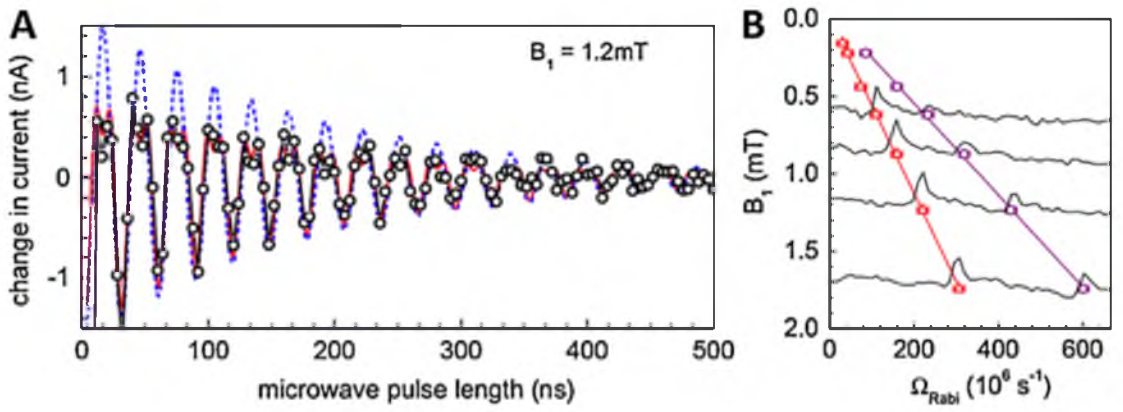


**Figure 1.3**. Rabi oscillations showing a beating component. (a) Coherent oscillations of the ensemble of spin pairs, observed by measuring the change in an MEH-PPV diode current 7.2 μs after application of resonant microwave pulses of increasing length. The fit with an exponentially damped sinusoidal function with components at both $\Omega_{Rabi}$ and $2\Omega_{Rabi}$ is shown (solid red line), as is a fit with only a single frequency component $\Omega_{Rabi}$ (dashed blue line). (b) Sample Fourier transform spectra of Rabi nutation traces obtained at different $B_1$ field strengths. The frequency of the two peaks was determined, and plotted as a function of $B_1$. Reprinted figure with permission from Physical Review Letters [1] as follows: D. R. McCamey, K. J. van Schooten, W. J. Baker, S.-Y. Lee, S. Paik, J. M. Lupton, and C. Boehme, Phys. Rev. Lett. **104**, 017601 (2010). Copyright (2014) by the American Physical Society.

this point it has become uncontroversial that s=½ spin pairs are responsible for these spin-dependent room temperature effects and therefore for the microscopic origin of OMAR.

When magnetic resonance of charge carrier spins is detected through optical emissions or electric currents in organic semiconductors using spin-dependent processes, the quantum mechanical observable is not polarization. Instead, permutation symmetry (i.e., the singlet content) is the accessible observable. Since permutation symmetry within a spin-pair ensemble does not depend on temperature and the magnetic field (in contrast to polarization) [109], the two s=½ spin-pair processes allow for the observation of magnetic resonance effects at very low magnetic fields.

When Baker et al. began measuring room temperature EDMR on MEH-PPV at low fields ($B_0$<10mT), a strong EDMR signal was observed at resonant driving frequencies of 350MHz and even below [3], which was nearly identical in magnitude to the EDMR signal observed at X-band (approx. 10GHz). This result alone, as displayed by the magnetic field dependence in Figure 1.4, was another important test of the polaron pair model. This model showed that permutation symmetry-detected magnetic resonance spectroscopy of Zeeman split states (not zero-field split states) can be conducted at very low magnetic fields. Such experiments would be prohibitive for conventional inductively-detected magnetic resonance methods. There are several dramatic implications of this realization: First, it allows for the execution of spin spectroscopy of those paramagnetic states involved in OMAR under the exact conditions where this effect

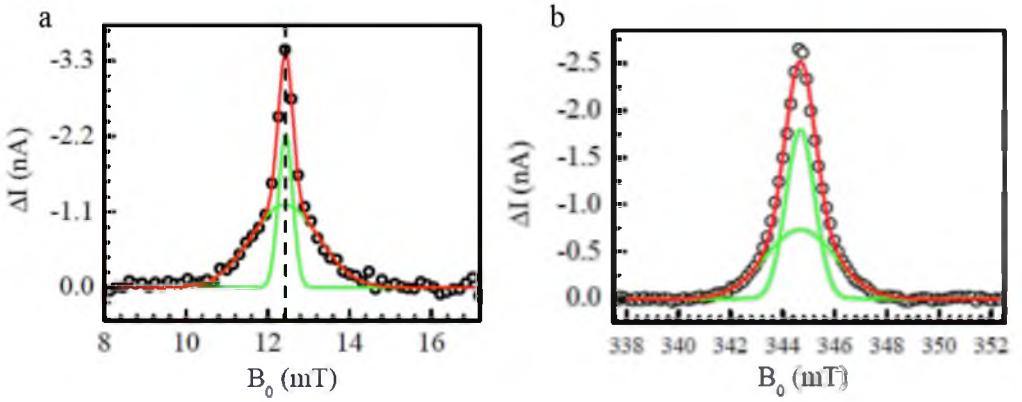


**Figure 1.4**. Plots of the EDMR signals (the current changes) in an MEH-PPV polymer diode as a function of the magnetic field in the presence of AC fields with (a) 350MHz and (b) 9.66GHz, respectively. In both cases, the two Gaussian magnetic resonance peaks are visible (the differences of the resonance line width will be discussed in Chapter 2) causing approximately equal current changes. This proves that in contrast to inductively-detected conventional ESR, spin polarization does not significantly influence these observed current changes. Reprinted from Physical Review Letters [2] and Nature Communications [3].

becomes most pronounced (approx. 0.1mT to 10mT). Second, the ability to observe low magnetic field magnetic resonance opens up the possibility to investigate magnetic resonance phenomena under very unconventional conditions such as when the strength of the resonant magnetic field $B_1$ exceeds the strength of the Zeeman field $B_0$. For conventional inductively detected resonance spectroscopy, $B_1$ is always much weaker than $B_0$. This is why the rotating frame approximation is usually applicable for the description of magnetic resonance experiments and why the resonant driving field can be treated as a perturbation. When $B_1 > B_0$, this treatment of the magnetic resonance effect does not apply anymore. One could refer to this regime as the nonlinear magnetic resonance regime. In the past, this regime has mostly been ignored in both the theoretical as well as experimental literature. Experimentally for $B_0$, where reasonable spin polarization exists (even at low temperature), the needed $B_1$ fields were technically not attainable. With OMAR-detected permutation symmetry measurements, this regime becomes accessible and a strong motivation is given to explore OMAR in the presence of AC magnetic fields.

### 1.3 OMAR in presence of an AC magnetic field

Figure 1.2 displays an example of how OMAR changes in a polymer diode in the presence of an oscillating magnetic field compared to its absence. Baker et al. showed that the magnetic field where this deviation is strongest depends linearly on the applied AC frequency, as shown in Figure 1.5. This was tested between 30MHz and X-band (≈10GHz) and it showed that the effect was due to the Zeeman splitting (and not due to a zero-field splitting effect) of charge carriers.

Following this discovery, a theoretical description of the ac-OMAR effect was

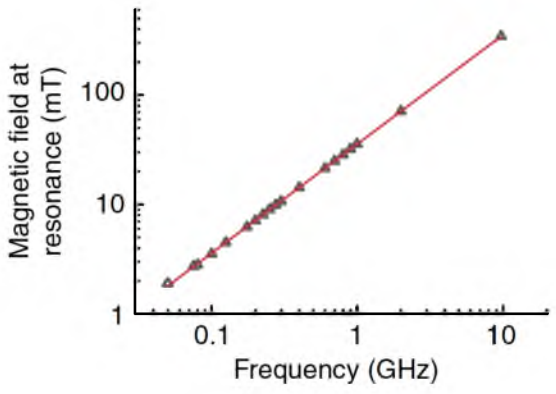


**Figure 1.5**. Plot of the peak magnetic field where maximal MR-induced current change is measured as a function of the applied excitation frequency, following a linear relationship (note that the error of the data points is below the size of the symbols). A linear fit of the above data yields a gyromagnetic ratio $\gamma = 28.03(4)$ GHz $T^{-1}$ and a corresponding $g$-factor $g = 2.0026(4)$. Thus, the electrically detectable electron gyromagnetic ratio can be used as an absolute magnetic field standard. Reprinted from Nature Communications [3].

developed by Roundy and Raikh [4], who derived quantitative predictions for the OMAR current as a function of the applied $B_0$ and $B_1$ fields that were based on the now well-corroborated assumptions that polaron pair recombination is the spin-dependent process that governs the OMAR effect. This work has several important implications. First, it provides predictions that can be scrutinized experimentally in a very straightforward way and with high accuracy. This in turn, allows for additional tests for the polaron pair model. Second, Roundy and Raikh's work confirmed results by Baker et al. [3], which showed that by increasing the power of the resonant driving field, the current response increases as well. The theory predicts a linear dependence of the current change to the amplitude of the driving fields (the square root of the power). For a resonant absorption experiment, this is a quite unexpected dependence. Third, the theory work revealed that at high driving powers when the nonlinear magnetic resonance regime is approached, a peculiar collective motion of the spin pairs could evolve, which leaves a distinct imprint

on the OMAR function. This spin-collective effect essentially constituted what is well known from electric dipole theory as the superradiant Dicke effect.

Figure 1.6 displays the dependence of the OMAR current change on the $B_1$ strength (in units of the hyperfine field strength $b_0$) as derived by Roundy and Raikh for the on-resonance case. The plot shows different qualitative behaviors of the OMAR current for different magnitude ranges of $B_1$. The linear current increase takes place at smallest $B_1$, while the spin-cooperativity regime becomes dominant at highest $B_1$ when the current change reverses its sign.

Some experimental tests of Roundy and Raikh's theory work have already been

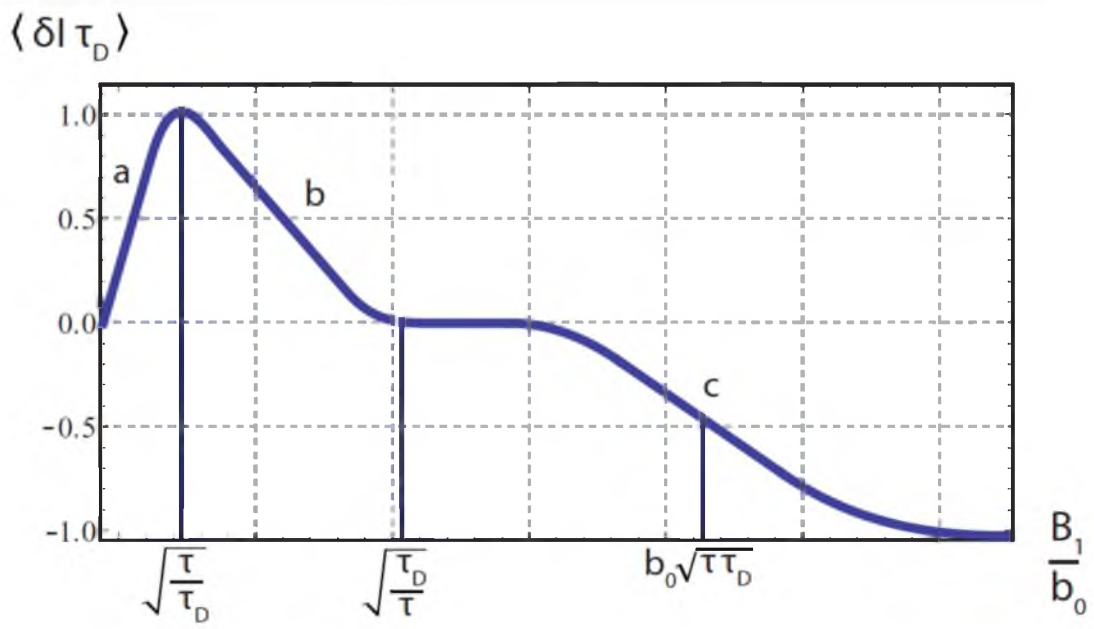


**Figure 1.6**. Schematic dependence of the radiation-induced change to the current on the amplitude $B_1$ of the ac magnetic field as predicted by the theory of Roundy and Raikh [4]. The quantitative nature of this function depends on parameters that characterize the polaron pair recombination processes that were the foundation for the calculation. For details see Chapter 2. Reprinted figure with permission from Phys. Rev. B [4] as follows: R. C. Roundy and M. E. Raikh, Phys. Rev. B **88**, 125206 (2013). Copyright (2014) by the American Physical Society.

given by the studies of Baker et al. [3] and Wedge et al. in 2013 [5]. Wedge et al. conducted reaction yield detected magnetic resonance (RYDMR) experiments, where a chemical reaction rate is optically measured that depends on the permutation symmetry of the weakly coupled spins of two nonrecombined radicals (chrysene and pyrene) in a solution. These experiments were executed at static magnetic fields below <4mT combined with an RF field, similar to the OMAR-based EDMR detection discussed above. The results of these experiments, some of which are displayed in Figure 1.7, confirm the general qualitative behavior of the Roundy and Raikh's predictions, yet they neither tested the detuning behavior for the linearity of the initial rate increase with $B_1$, nor did they scrutinize the presence of the Dicke effect. In fact, since the work by Wedge et al. and Roundy and Raikh were published at approximately the same time, the authors of both studies were mutually unaware of the respective other work.

The realization that this spin-cooperativity can evolve was the most unexpected result of Roundy and Raikh's paper and it is the main motivation behind the work that is presented in the following chapters. The experimental verification of spin-cooperativity in a polymer diode under room temperature operating conditions at low magnetic fields can have drastic implications for our understanding of how organic light emitting diodes (OLEDs) operate in a broad range of devices (e.g., mobile phone displays, lighting, television screens, etc.) for which they are utilized nowadays.

The primary goal of the work presented in this thesis was to develop and execute an experiment that scrutinizes various predictions by Roundy and Raikh [4]. This includes the linear amplitude dependence of the OMAR current changes, the saturation behavior, the behavior under detuning from the magnetic resonance condition, and the

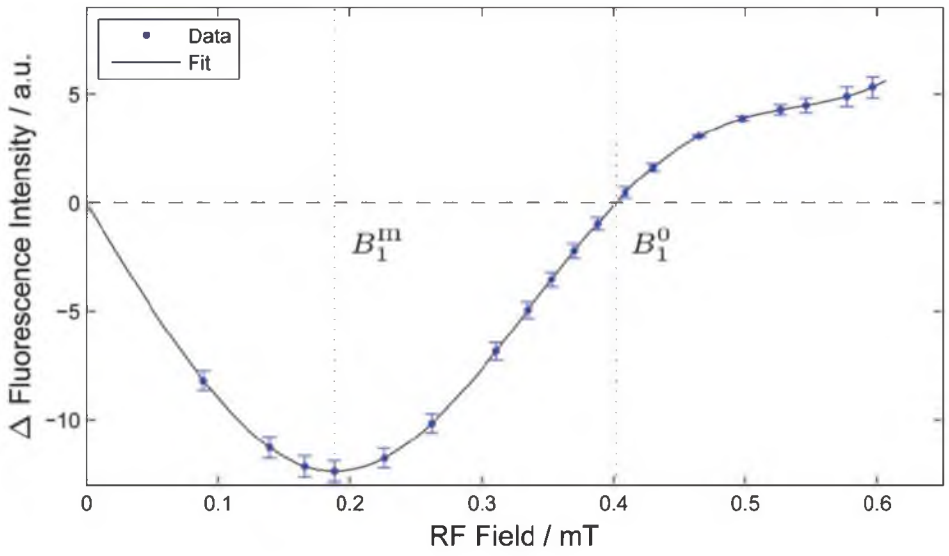


**Figure 1.7**. Experimental RYDMR signal strengths for a 36MHz-oscillating field applied orthogonal to a static magnetic field as a function of the RF field amplitude. The qualitative behavior confirms the theoretical predictions for permutation symmetry-controlled spin pair transitions rates made by Roundy and Raikh [4]. Reprinted with permission from Physical Chemistry Chemical Physics [5].

existence of the spin-cooperativity behavior when the Dicke effect sets in at very high magnitudes of $B_1$. The technical ideas for the implementation of this experiment are outlined in detail in the following chapters. They are based on using polymer diodes in order to observe permutation-symmetry controlled spin-dependent rates, specifically the recombination rate of polaron pairs in a π-conjugated polymer. As discussed in Chapter 2, hyperfine fields produced by the all-abundant hydrogen will play a quite significant role for this. The experiments therefore were designed to be conducted in the presence of different hyperfine field strengths by use of materials with different isotopical compositions.

# CHAPTER 2

# SPIN-DEPENDENT PROCESSES AND MAGNETORESISTANCE IN ORGANIC SEMICONDUCTORS

## 2.1 Organic semiconductors

### 2.1.1 The chemistry of polymer semiconductors

Organic materials are condensed matter systems that are based on organic chemistry, which means they consist predominantly of hydrocarbon compounds with other elements (oxygen, nitrogen and many other) occurring in much smaller numbers. Perhaps the simplest example for a hydrocarbon molecule is methane $CH_4$. Organic conductors and semiconductors are organic materials that are able to conduct electric charges. In general, this is because of their particular density of energy state structure, which is similar but not identical to those of inorganic conductors and semiconductors, respectively. Similar to inorganic semiconductors, organic semiconductors possess a band-gap structure with a range of unoccupied electronic states above the Fermi energy, the so-called lowest unoccupied molecular orbitals (LUMO). These are similar to the conduction band and another range of occupied electronic states below the Fermi energy, the so-called highest occupied molecular orbitals (HOMO), similar to the valence band. Between these two ranges of occupied and unoccupied electronic states is an energy range with a very low density of energy eigenstates that is analogous to a bandgap.

For an organic material to be an organic conductor or semiconductor, there has to

be a mechanisms that allow charges to be mobile. For most conductive organic materials, the dominant charge transport mechanisms are hopping or tunneling mechanisms, electronic transitions that take place between localized electronic states. Examples for charge transport via localized states in organic materials is the hopping within polymer materials [2]. Polymers that allow for charge transport are usually π-conjugated, which means that between the monomer units of the polymer chain, there are carbon double bonds (C=C) where two carbon atoms are connected via a σ- and a π-bond orbital. If the double bonds of carbon atoms within a polymer chain alternate with simple σ bonds (-C=C-C=C-…), spontaneous switches between the π-bond sites and the σ-bond sites can occur, which physically constitute spontaneous quantum mechanical transitions between different electronic orbitals. If such switches happen repeatedly and the net motion of the double bonds occurs towards a preferred direction, charge transport takes place [110]. Charge transport in organic materials is depicted in Figure 2.1. The molecules (chains) in most polymer materials are usually arranged in a disordered structure. When they form a solid, the microscopic structure on a molecular level resembles great structures similar to cooked spaghetti. Conjugated polymers can be prepared as thin semiconductor films and cover large areas at low cost [109]. They are used for a variety of electronic devices, predominantly in organic light emitting diodes (OLEDs). These OLEDs are used not just for lighting applications but also for displays due to their brilliant colors [111]. They can also be used to make organic solar cells and organic field-effect transistors [112-115].

### 2.1.2 Para-phenylene-vinylene

The type of π-conjugated organic polymer at the center of this dissertation is poly(p-phenylene vinylene) (PPV), which has been shown to have good mechanical

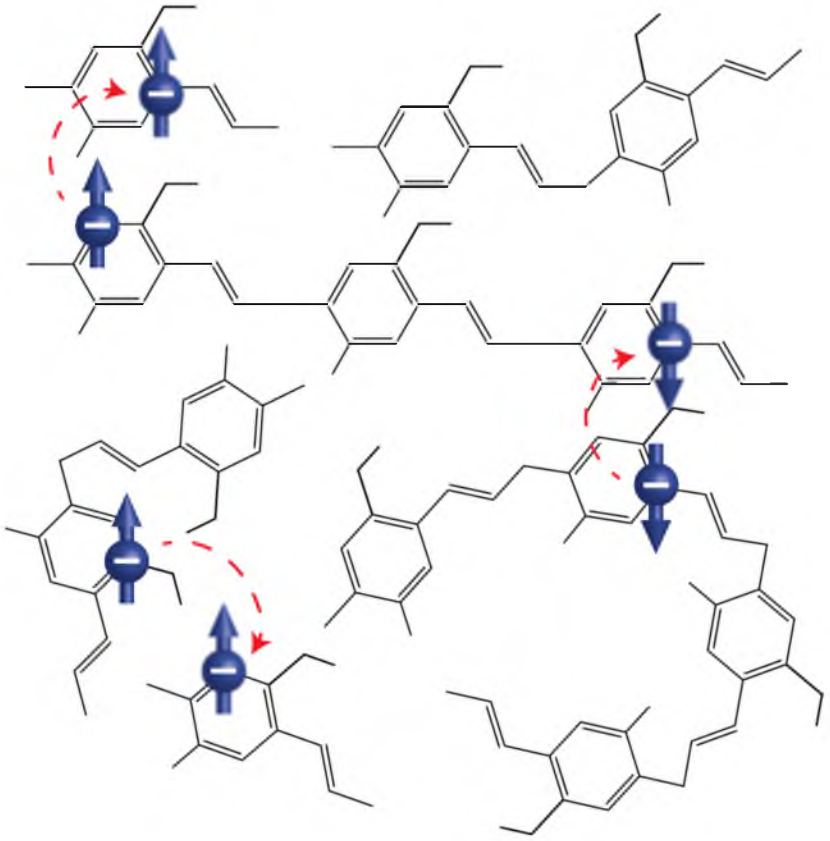

**Figure 2.1**. Illustration of the main charge transport mechanisms in a π-conjugated polymer material. Electric charge propagates due to spontaneous transitions between localized molecular π-orbitals.

flexibility and chemical stability [116]. The practicality of using PPV in OLEDs was first shown with electroluminescence experiments by Burroughes et al. in 1990 [117]. PPV has an alternating single and double bond structure (it is π-conjugated), and the phenyl groups are para to each other with respect to the double bonds. As with most polymers, PPV-materials are disordered and a broad range of defects exist, which greatly influences the optoelectronic properties of PPVs, including their charge mobilities, recombination times, photoconductivity, etc. Defects include chain ends, aggregates, impurities, and others.

The material used in this study is a form of PPV called poly[2-methoxy-5-(2'-ethyl-hexyloxy)-1,4-phenylene vinylene (MEH-PPV), where the MEH is a side chain of the PPV polymer. Side chains play an important role for the processability of polymer material. There are various types of PPV (with different side groups) that differ solely by their side groups. Because they interact differently with solutions during deposition, they develop different morphologies in the solid state and consequently lead to PPV materials with quite distinct electronic and optoelectronic properties.

Figure 2.2 represents the structures of the hydrogenated and deuterated MEH-PPV molecules used for the experiments presented in this dissertation. MEH-PPV was chosen as a model system because much has been known not only about its general optoelectronic [118] and magneto-optoelectronic [63] materials properties but also its spin-dependent electronic processes [62,108,109,119-125].

### 2.1.3 Band structure and doping of condensed matter systems

Many electronic properties of solid-state systems can be understood by studying material. The "bands" are energy ranges in which very high densities of states exist where electrons are spatially mobile. The conduction band (or LUMO) usually represents a band that is unoccupied or only marginally occupied in equilibrium while the valence band (or HOMO) represents the first band below the Fermi energy in which all or almost all of the states are occupied.

The band structures of solids can be categorized into three main types: metal, insulator, and semiconductor. These categories are based on the value of the band gap, which is the difference between the lowest conduction band energy and the highest

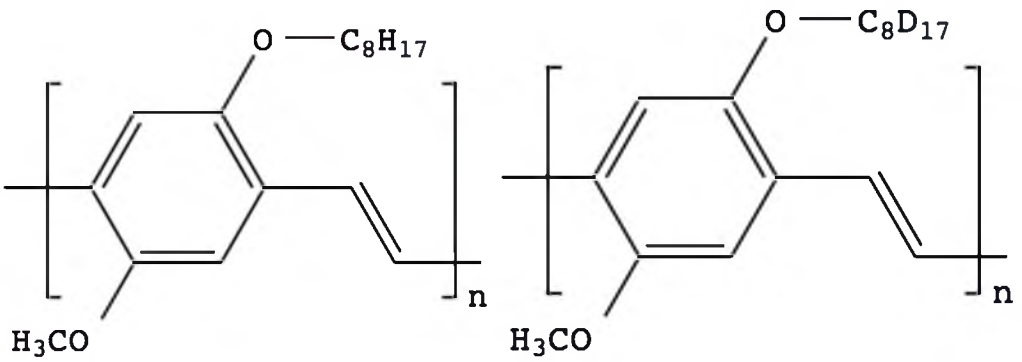


**Figure 2.2**. MEH-PPV molecular structures. The PPV molecule with a side chain of either (a) hydrogenated or (b) deuterated MEH.

valence band energy. For metals, the bandgap is negative, which means that there is a continuous spectrum of overlapping bands, and charge carriers are free to move between bands and thus move spatially through the material. Consequently, the electrical resistance of a metal is low. In an insulator, the bandgap is positive and much larger than the thermal energy.

Electrons in an intrinsic (=undoped) insulator cannot move between bands and the valance band is entirely occupied while the conduction band is entirely empty. The net charge flux within the material is consequently vanishing and the electrical resistance of an insulator is very large. Semiconductors are materials that range somewhere between metals and insulators. Their band structures, illustrated for both crystalline and disordered materials in Figure 2.3, exhibit a positive bandgap that is small enough for electrons to be excited from the valence into the conduction band and thus a current can flow through the material. While metals and semiconductors both conduct electric charge, metals usually display higher conductivities and have the opposite temperature dependence compared to

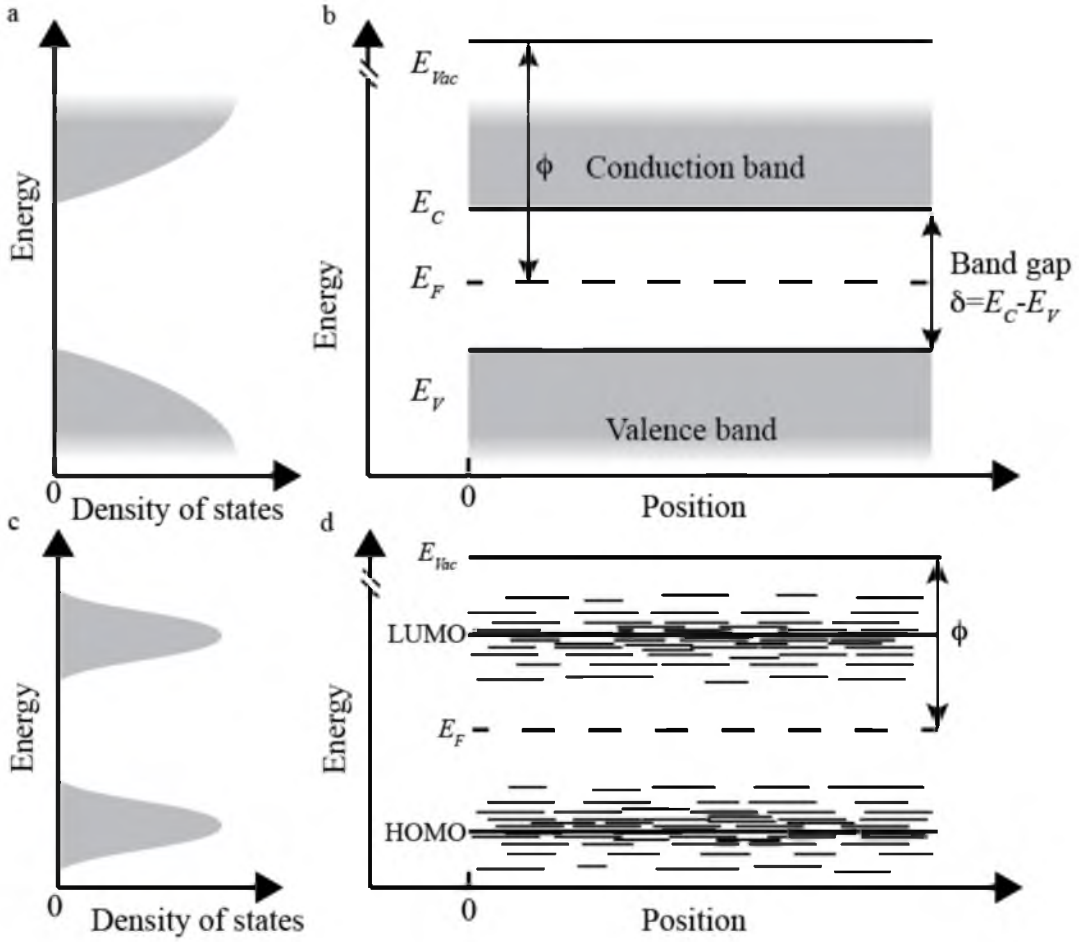


**Figure 2.3**. Illustration of the energy as a function of density of states and position for a crystalline semiconductor and an organic polymer. (a) Illustration of the density of states for a crystalline semiconductor. (b) Illustration of the band structure in a crystalline semiconductor including the conduction band, representing a high density of delocalized energy eigenstates above the conduction band energy $E_c$, a high density of delocalized energy eigenstates below the valence energy $E_v$, the band gap of width $E_c$- $E_v$ between the two bands, and the Fermi energy $E_f$ for an intrinsic (undoped) material. (c) Illustration of the density of states for an organic semiconductor. (d) Illustration of the band structure in an organic semiconductor. The conduction band and valence bands consists of disorder related randomly distributed localized states, these so called LUMO and HOMO state distributions. Charge carriers within these bands can be mobile due to spontaneous transitions such as tunneling or thermally induced hopping.

semiconductors. With decreasing temperatures, metals become better conductors while semiconductors become insulators.

In conventional semiconductors with delocalized electronic states, the valence band states result from a delocalization (i.e., a spread out hybridization) of the covalent chemical bonds that hold the materials together [126]. Similarly, the corresponding HOMO states in organic semiconductors are electrons bound in molecular bonds. When valence band states are emptied by excitation on an electron into the conduction band, an unoccupied valence band state appears that can move throughout the valence band continuum like a real particle with a positive elementary charge. These empty valence states are therefore called "holes." Macroscopically, holes can be treated like positive charge carriers [127,128].

Next to the thermal excitation (when the thermal energy $kT$ is greater than or equal to the band gap, with $k$ being the Boltzmann factor and $T$ the temperature), charge carriers can also be excited optically (when the photon energy $hf$ is greater than or equal to the band gap, with $h$ being the Planck constant and $f$ the photon frequency). In either case, any creation of a free electron in the conduction band (LUMO states) in undoped (intrinsic) semiconductors materials also creates a hole in the valence band (HOMO states). Both electrons and holes can be considered to be free charge carriers and can contribute to the macroscopic charge current. Electrons and holes are not only charge carriers with different charge but can also have significantly different mobilities.

The Fermi energy level $E_f$ represents an energy above which the probability of a state in a solid being filled is below 50% while below $E_f$ the probability is above 50%. The analytical representation of the probability $f(E)$ of a state with energy $E$ being

occupied is found by Fermi-Dirac statistics, $f(E) = \frac{1}{1+\exp\left(\frac{E-E_f}{kT}\right)}$ [17]. This equation is derived from the circumstance that charge carriers are fermions, which implies that their collective wave function must be antisymmetric. The statistics resulting from this property determines the occupation probability of a Fermi gas. The Fermi-Dirac statistic shows that at absolute zero, the probability of an energy eigenstate being occupied becomes a step function with the step being set by the Fermi energy. For intrinsic semiconductors, $E_f$ is between the valence band (HOMO) and the conductions band (LUMO). This is why all valence states are occupied (there are no holes) and all conduction band states are unoccupied (there are no free electrons), which is why these materials become insulators.

Semiconductor materials can possess very different Fermi levels due to both the intrinsic properties of a given material and the defect doping. The presence of point defects (added atoms or molecules or vacancies), which add or remove electrons from the materials and which therefore change the distributions of occupied electrons states without relevantly changing the band structure (i.e., the overall distribution of electron states) [129], will shift the magnitude of the Fermi energy in a given material. Thus, even approximately chemically identical materials with nearly identical band structure can exhibit different $E_f$. If $E_f < E_v$ in a material, unoccupied valence band states exist, but there will be no occupied conduction band states. Therefore, the material is a hole conductor. The holes are then called majority carriers while electrons are minority carriers and the material is referred to as a p-material. Similarly, when $E_f > E_c$, there will be no unoccupied valence band states, but occupied conduction band states will exist and the given material will be an electron conductor, an n-material. Holes will be minority

carriers while electrons become majority carriers [130].

### 2.1.4 Electronic junctions between condensed matter materials

When two materials with different Fermi energies are connected electrically (i.e., their interfaces are brought into close physical proximity on an atomic scale), charge carriers can shift between the two materials in order to generate a thermal equilibrium. The changes of the electrical potential induced by these shifted charges will then superimpose to the band structures of these materials. These changes of the band structure manifest themselves in changes to the densities of occupied energy states as well as an overall shift of the density of energy states as a function of position within regions close to the interface; a so-called electronic "junction" between the two materials is formed.

Prototypical examples for this are p-n-junctions, which form when p- and n-materials are bought into contact. The qualitative features of a p-n junction band structure (i.e., a junction based on a p-material that has an interface with an n-material) are shown in Figure 2.4. Most significant for a p-n-junction is the "build-in" potential that forms due to the formation of a thermal equilibrium between the two materials with different wave functions because of electron recombination with holes in the junction region. It is this potential that makes the p-n junction in equilibrium (in absence of a bias) electrically insulating. When small biases are applied (in either direction), the junction that is devoid of charge carriers prevents charge transport to occur and no current will form. When a positive bias is applied in the p-n direction, additional holes are injected into the p-region and additional electrons are injected into the n-region [104,131,132]. A steady thermal nonequilibrium state and accordingly a continuous recombination current will evolve.

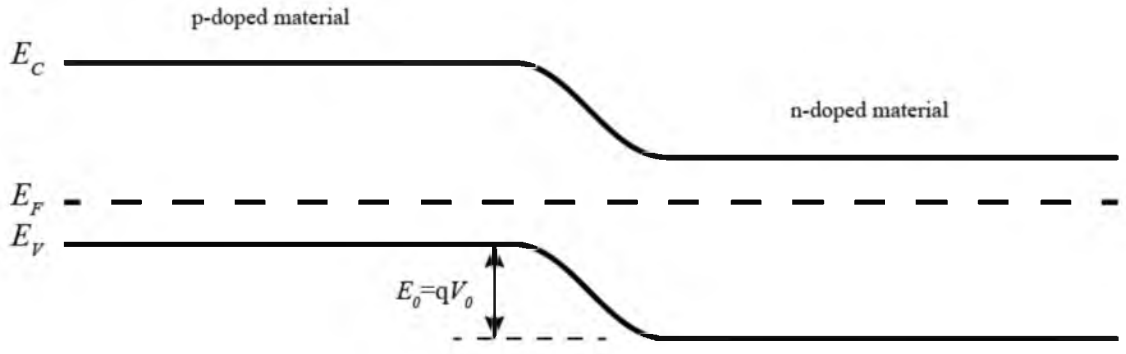


**Figure 2.4**. A p-n junction diode. The diode diagram shows a shift in the energy levels from a p-doped to an n-doped material due to the potential $V_0$ produced by shifted charges at the junction interface caused by the two materials with two different Fermi energies attaining a thermal equilibrium. This energy level shift can be changed by application of an external potential difference due to a bias voltage $V$, such that the total energy shift between the bands becomes $E=q(V_0+V)$.

This is what gives p-n junctions (a.k.a. diodes) their characteristic asymmetric current-voltage (I-V) behavior [126].

Many organic semiconductor materials can be used for the implementation of diodes as well. Organic diode devices are based on a similar band structure as shown in Figure 2.4, yet there are also significant differences. Most of these differences are related to the circumstance that the conductivity mechanisms in organic semiconductors are of a profoundly different physical nature than those of diodes based on delocalized band systems. Many organic conductors and semiconductors are so-called injection conductors, which means they do no exhibit significant intrinsic charge carrier densities but are able to build up charge carrier densities and thus charge transport when they are injected at appropriate energy levels. Thus, organic junction devices typically consist of one or more organic conductors and different organic or inorganic injector materials. The Fermi levels as well as the work functions (i.e., the difference between the vacuum

energy levels of electrons and the Fermi levels) will then determine whether these organic junction devices allow for electron injection, hole injection, or both, and thus whether the built devices act as diodes with asymmetric IV characteristic or as symmetric resistors.

Figure 2.5 displays the band structure of an organic diode based on MEH-PPV. The structure consists of a layer stack that was used extensively for the experiments presented in this dissertation. It has been investigated extensively before with regard to both the electronic properties [38] as well as with regard to the spin-dependent transitions within [106]. At the center of the diode is the disordered polymer semiconductor MEH-PPV whose bands consist of random distributions of localized electronic HOMO and LUMO states. The material is sandwiched between an electron (Ca) and a hole injector polystyrene sulfonate doped Poly(3,4-ethylenedioxythiophene, PEDOT:PSS) material. (Under forward bias conditions, the MEH-PPV will therefore conduct both electrons and

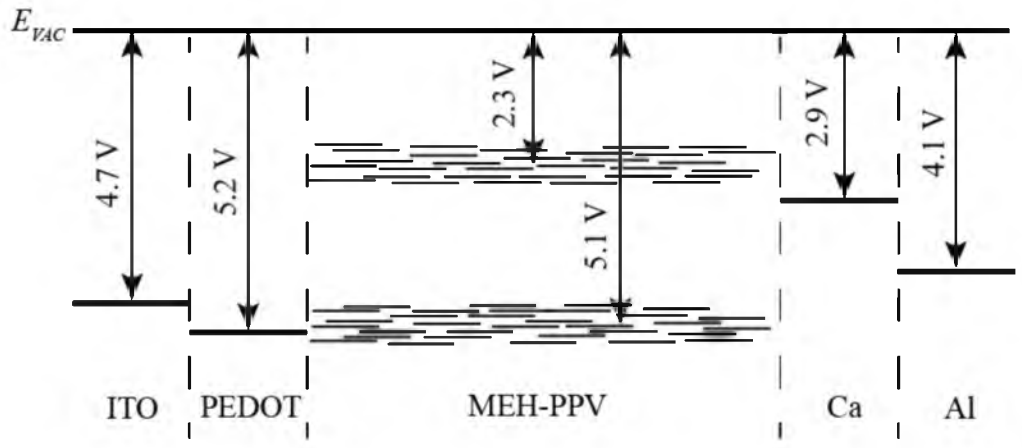


**Figure 2.5**. Equilibrium band structure of an MEH-PPV diode based on a stack of indium-tin oxide (ITO), PEDOT, MEH-PPV, calcium, and aluminum. The diagram shows all band offsets induced by the different material work functions. The PEDOT and calcium cause a shift in the energy levels in order to inject both electrons and holes to create a balanced diode device.

holes and recombination can occur. As a significant share of this recombination is radiative, the given band structure represents an OLED. Both the PEDOT:PSS and the Ca are connected to additional conducting layers, ITO and Al, which serve as transparent, high-conductivity contacts and capping layer contacts, respectively.

## 2.2 Polarons and polaron pair states

In many organic conductor and semiconductor materials, the localized charge carrier states are assumed to be of a polaronic nature, which means the physical nature of the local charge carrier state is strongly influenced by bonding distortions that occur when an elementary charge is present [110]. While one can question whether or not this picture is accurate for different types of materials within the broad range of organic conductors, it has almost become a standard to refer to localized charge carrier in organic semiconductors as polarons [69,99,103,119,122]. Microscopically, polarons are assumed to be mobile within and between molecular entities, yet more mobile within a molecule. For molecules with strong geometric anisotropies (e.g., polymers), this mobility implies that polarons with opposite charges can easily form Coulombically bound pair states across molecular boundaries without directly recombining. These strongly Coulombically bound but weakly wavefunction overlapped pairs are referred to as polaron pairs and were first described by Frankevich et al. [80,102]. The Coulomb interaction between the electron and hole polarons extends typically across neighboring chains. To form pairs, the polarons must therefore be sufficiently close (within the Onsager radius, which defines the distance where the Coulomb energy exceeds the thermal energy [133]), yet at the same time also far enough from each other such that spin-exchange and spin-dipolar coupling do not become too strong, as discussed in greater detail in section 2.5.

Compared to other electronic excitations in condensed matter systems, polaron pairs states can exist for periods of time in the micro- to millisecond regime. They can annihilate by thermal dissociation or by recombination, which typically does not take place by direct transitions into charge carrier ground states but by creation of strongly spin-coupled excitonic states. In excitonic states, when the polaron states of electrons develop strong overlap with the hole polaron, significant exchange interaction takes place without the complete loss of the energy contained in the pair system [62]. Similar to polaron pair states, excitons exist in various spin-manifolds. The variety of spin-interactions within polaron pairs and excitons as well as between polarons, polaron pairs, excitons, and combinations is responsible for spin-effects and therefore for the broad range of magnetic field effects, including magnetoresistance in organic semiconductors.

### 2.3 Magnetoresistance in organic semiconductors

OMAR effects have been described in the literature for decades [80,134] and many studies have been undertaken to understand the processes responsible for these effects [42,49,62,65,78,105,135,136]. Many hypothesis have been created [69,137-140] and many experimental and theoretical studies have been conducted in order to test these hypotheses. Much of the interest in OMAR has been due to the large magnitude of the observed relative resistance changes (corresponding to observed relative current change $\Delta I/I_0$, where $I_0$ is the current at zero magnetic field, exceeding 20%) at room temperature and low magnetic fields ($B_0$~10mT) [67]. The main fundamental question that these huge values raise is how magnetic field interactions with s=1/2 electron spins (the polarons) and/or s=1 spins (excitons) that take place on μeV energy scales can control ev-range charge transport processes in the presence of thermal energies in the mid-meV range.

## 2.4 Spin-dependent processes

The plethora of existing OMAR hypotheses agree about the assumption that spin interactions with the external magnetic field and not angular momentum effects are the main cause for OMAR. In spite of the minute energy scales of spin-states, this assumption becomes possible due to the weak spin-orbit coupling in organic semiconductor materials – weak spin-orbit coupling allows spin-selection rules to control electronic transitions, as electronic transitions in absence of spin-angular momentum transitions must be spin conserved. A spin-selection rule is given when the transition matrix element between two electronic states is governed by the spin-manifolds of the two states before and after the transition. With this understanding and the known variety of spin-species in organic materials (e.g., polarons, polaron-pairs, excitons), there has nevertheless been significant controversy about the specific microscopic nature of spin-dependent processes in these materials. Controversy has existed about which of those mechanisms described in the literature affect OMAR under which environmental and materials conditions. This controversy has made the pursuit of technical applications of OMAR difficult, as applications require the ability to control OMAR by materials design. In the following, some of the models for spin-dependent electronic transitions that are cited in the literature as causing OMAR are briefly summarized. These include the single spin-½ processes, polaron pair recombination, bipolaron transport, triplet-exciton polaron recombination, trion recombination, and triplet-triplet exciton annihilation:

- **Single spin-½ processes**. The single spin-½ charge carrier model is arguably the simplest model for spin control of electric charge transitions. In contrast to all other mechanisms discussed in the following, it does not necessarily have to

involve spin-selection rules, but instead it can solely be because of the energy difference of spin-states due to fluctuating local fields. Local fields include both spin-orbit fields, which, as stated above, are negligible in many organic materials and also hyperfine fields. This can be significant because of the all-abundant hydrogen in organic semiconductors. The qualitative features of the mechanism are illustrated in Figure 2.6, which illustrates how the spin-splitting of adjacent electronic states can be different and consequently the energy for an electron between the two states to overcome can be different as well [109]. Since the difference $\delta_1 - \delta_2$ between two splittings is typically minute and polarization is small due to $\delta_1$, $\delta_2 << k_BT$, this process is expected to have only a marginal influence on conductivity in many cases. Macroscopic observables such as OMAR are influenced by this mechanism and would greatly depend on equilibrium polarization and thus on temperature. However, this dependence is not observed [3], and therefore, no experimental reports exist which have confirmed this mechanism as the origin of OMAR.

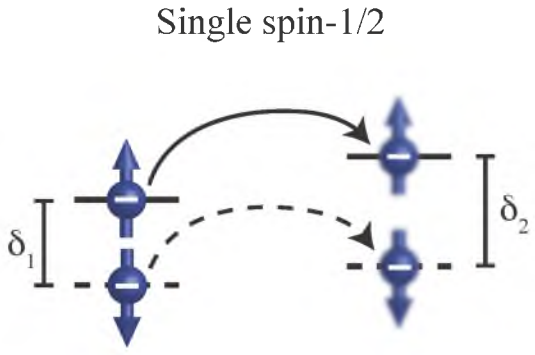


**Figure 2.6**. Illustration of single spin-½ transport model. The electronic transition probability between two spin states depends on the spin if the spin splittings of the two electronic states differ ($\delta_1 \neq \delta_2$).

- **Bipolaron transport**. The bipolaron pair model [69,86,87] describes spin-dependent transport due to the interaction of weakly spin-coupled pairs made up of like charges, electron-electron or hole-hole. The process is sketched in Figure 2.7. As charge transport takes place, one charge carrier can block the mobility of another, leading to a Pauli-blocking mechanism. If the charge carriers are in a singlet configuration, they can form an intermediate pair of two identical particles. If a triplet configuration exists, spin blocking takes place. Since the local hyperfine fields of each charge carrier differ from one another, there is a finite probability of creating a singlet state, lifting the blocking, and forming a bipolaron. The bipolaron model has been used extensively to explain OMAR, proposing that at low magnetic fields, local variations in the hyperfine field induces spin mixing and reduces the spin blockade of hopping transport. At its core, the spin-dependent bipolaron mechanism represents a spin-dependent intermediate pair process that goes back to a description of spin-dependent recombination described by Kaplan, Solomon and Mott [141].

  The essence of an intermediate pair model is that two electrons can create intermediate pairs, which can only undergo a transition into a pure singlet state. For the case of the bipolaron model, this is the actual bipolaron state; for the case of recombination, this is the singlet ground state when two charge carriers have either annihilated or dissociated into uncorrelated electrons. During the lifetime of the intermediate pair, the two electrons cannot undergo transitions into connecting electrons that are not part of the intermediate pair. At first, the distinction between an intermediate pair and a nonintermediate, random pair of two electron spins

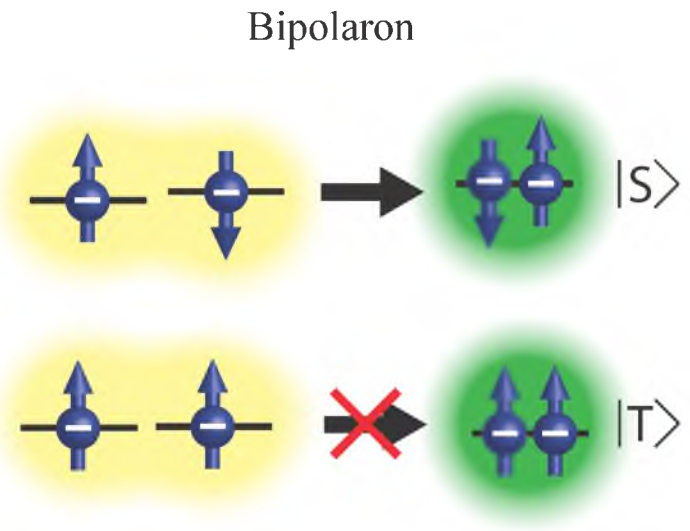


**Figure 2.7**. Illustration of bipolaron transport model. In the presence of two adjacent polaron states, the overall mobility of the two charges is higher when the pair state of the two spins has antisymmetric permutation symmetry as one charge carrier can transition through the other, forming a doubly occupied bipolaron state.

seems like pure semantics, but the implications of these intermediate pair processes versus nonintermediate pair processes for spin-dependent electronic transition rates are dramatic. In contrast to nonintermediate spin-dependent pair processes (e.g., as described by Lepine [142]), where spin-polarization is the all-determining observable, intermediate pair processes are solely spin-pair permutation-symmetry dependent. Thus, the observables controlled by these processes (e.g., OMAR) can be much stronger in magnitude and not directly dependent on temperature. As equilibrium polarization of electron spins at low magnetic fields and room temperature is all but negligible, weakly coupled intermediate spin-pairs are generated randomly but with roughly equal probability into any of the four eigenstates of weakly coupled pairs of spins with s=1/2. These eigenstates are combinations of up and down spin states. While the $|T_+\rangle = |\uparrow\rangle|\uparrow\rangle$

and $|T_-\rangle = |\downarrow\rangle|\downarrow\rangle$ are pure triplet states that forbid the formation of the bipolaron singlet state, the other two eigenstates $|\uparrow\rangle|\downarrow\rangle$ and $|\downarrow\rangle|\uparrow\rangle$ have singlet character and thus allow for a bipolaron formation. In a material in which a steady state current exists, a surplus of triplet spin pair configurations will have evolved. Since the application of an external magnetic field changes the spin-relaxation rates of these triplet pairs into singlet pairs and thus the formation rates of bipolarons, externally applied magnetic fields could influence the material's resistance.

At this time, there is still no unambiguous experimental confirmation of the bipolaron pair process in organic semiconductor materials. There has been the claim of experimental verification given by Behrends et al. [87], which was based on pulsed electrically detected magnetic resonance spectroscopy and unmistakably showed the involvement of pairs in spin-dependent pair processes in the polymer/Fullerene derivative blend material (MEH-PPV:PCBM). However, the conclusion that this shows the existence of bipolaron transport has been disputed as other spin-dependent intermediate pair processes such as spin-dependent polaron pair recombination (discussed below) could also explain the observed data [63,143].

- **Triplet-exciton polaron (TEP) recombination**. Instead of considering the interactions of weakly-coupled polaron pairs, Desai considers the mixing between strongly-coupled excitons [43,88]. Since the recombination of singlet excitons is much faster than the long lifetime of triplet excitons (≈25μs in $Alq_3$) [67], the spin population of triplet excitons is much greater than singlet excitons. Triplet excitons can weakly couple to polarons [144,145] as illustrated in Figure 2.8.

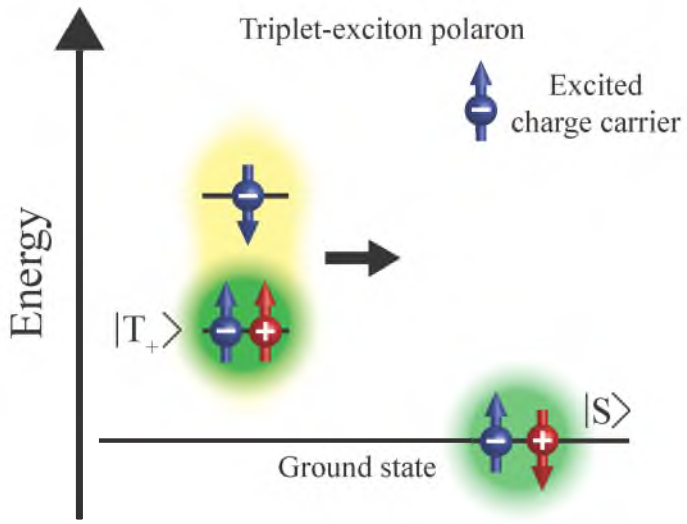


**Figure 2.8**. Illustration of triplet-exciton polaron recombination model. This mechanism involves the formation of weakly spin-coupled pairs of polaron states and triplet excitons that are already strongly coupled pairs of two charge carriers. The triplet-exciton polaron pairs can cause faster, polaron-assisted recombination of the triplet excitons into the ground state.

When the exciton recombines into the ground state, it transfers its energy to the charge carrier, called an exciton-charge interaction [144], a process similar to Auger recombination. This process is inherently spin-selection rule dependent: a magnetic field which induces a mixing between the singlet and triplet exciton states and lifts the degeneracy of the triplet states due to the Zeeman effect can change the polaron-assisted recombination rate. The singlet involvement will play only a minor role for this process since the energy splitting between singlet and triplet excitons is very large (0.7 to 1 eV for MEH-PPV [109]), compared to the Zeeman splitting of a typical hyperfine field (0.5μeV at 5mT [67]). The intersystem crossing between singlet and triplet excitons is therefore highly unlikely. However, the removal of the triplet degeneracy due to an applied magnetic field can also significantly change the recombination rate and thus cause

the OMAR effect.

While there has been clear spectroscopic evidence for the influence of triplet-exciton polaron recombination in MEH-PPV at low temperatures [106], which makes a role for this process for OMAR conceivable, there have been no reports for the observation of this process at room temperature. This is consistent with the dramatically reduced lifetimes of triplets at high temperatures. Also, the observation of the triplet-exciton process at low temperatures increases strongly when electrons become majority carriers [106], an observation that is understandable because this process requires three charge carriers and thus a majority and a minority charge.

- **Trion recombination.** Similar to the TEP model, the trion recombination model [89], shown in Figure 2.9, involves a triplet exciton coupled to a polaron. The difference is that the exciton and polaron now lie on the same molecular chain and thus are strongly bound. The three charges mutually interact very strongly, forming a three spin s=1/2 state referred to in the literature as trion [103,146]. The trion as a whole constitutes a paramagnetic spin s=3/2 particle. At this time, no spectroscopic evidence for the existence of the triplet-polaron process exists. The experiment that could provide the most unambiguous proof of trion-controlled recombination would be the electrical detection of spin-Rabi nutation under a pulsed magnetic resonance drive. The electrical observation of a coherent spin-Rabi nutation of an s=3/2 particle ought to take place under a Rabi frequency of $\Omega=\sqrt{3}\gamma B_1$ with $B_1$ being the amplitude of the driving field and $\gamma$ being the gyromagnetic ratio [147]. So far, no pulsed electrically detected magnetic

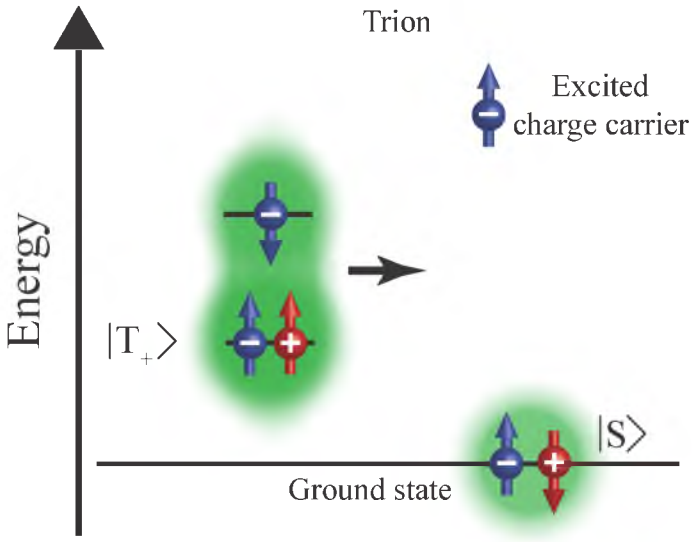


**Figure 2.9**. Illustration of the trion-recombination process. Strong exchange between a triplet exciton and a polaron leads to trion formation. The recombination of two of these polarons into a ground state along with the creation of a free polaron is spin-dependent and thus the net current, which depends on the free polaron density, is magnetic field dependent.

resonance (pEDMR) experiment has revealed the $\Omega/\gamma B_1=\sqrt{3}$ component.

- **Triplet-triplet exciton annihilation**. When the concentration of triplet excitons is high, coupling between them can become significant [38] and due to spin conservation, two triplet excitons can recombine (annihilate) by the formation of a singlet ground state along and a singlet exciton [109], illustrated in Figure 2.10. Similar to the triplet-exciton polaron process and the trion process, the two triplet excitons could form either strongly bound pairs of two s=1 spins or a tightly bound s=2 system. The spin-Rabi nutation frequencies of such spin systems are known to be $\sqrt{2}\gamma B_1$ and $\sqrt{6}\gamma B_1$ [147]. Since neither one of these nutation components has been observed through electrical detection of the spin-dependent

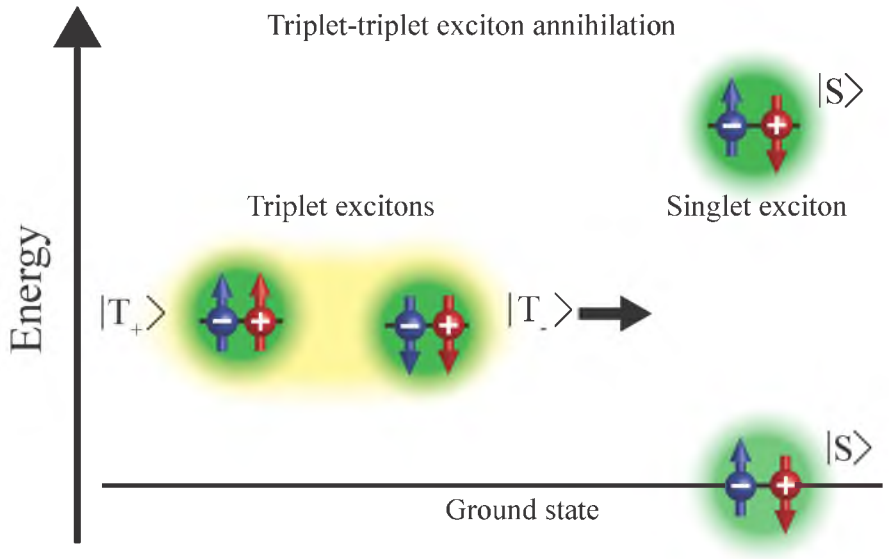


**Figure 2.10**. Illustration of the triplet-triplet exciton annihilation process. Depending on the spin state of two triplet excitons in close proximity, there are different probabilities for the pair to recombine into a singlet ground state and a fast decaying singlet exciton. Whether or not this spin-dependent process can affect conductivity and this magnetoresistance is not known.

- transition rates, there is currently no proof that triplet-triplet annihilation processes influence conductivity and thus OMAR.
- **Polaron (e-h) pair recombination**. Polaron pair recombination is spin-dependent recombination through the formation of Coulombically bound, weakly spin-coupled intermediate pairs which may or may not undergo transitions into singlet- or triplet-exciton states. The polaron pairs, also called excitonic precursor pairs, are intermediate pairs in the sense of Kaplan, Solomon, and Mott [141], similar to the intermediate pairs of unipolar charge carriers discussed above in the context of the bipolaron transport process. Figure 2.11 illustrates the qualitative nature of the polaron pair process.

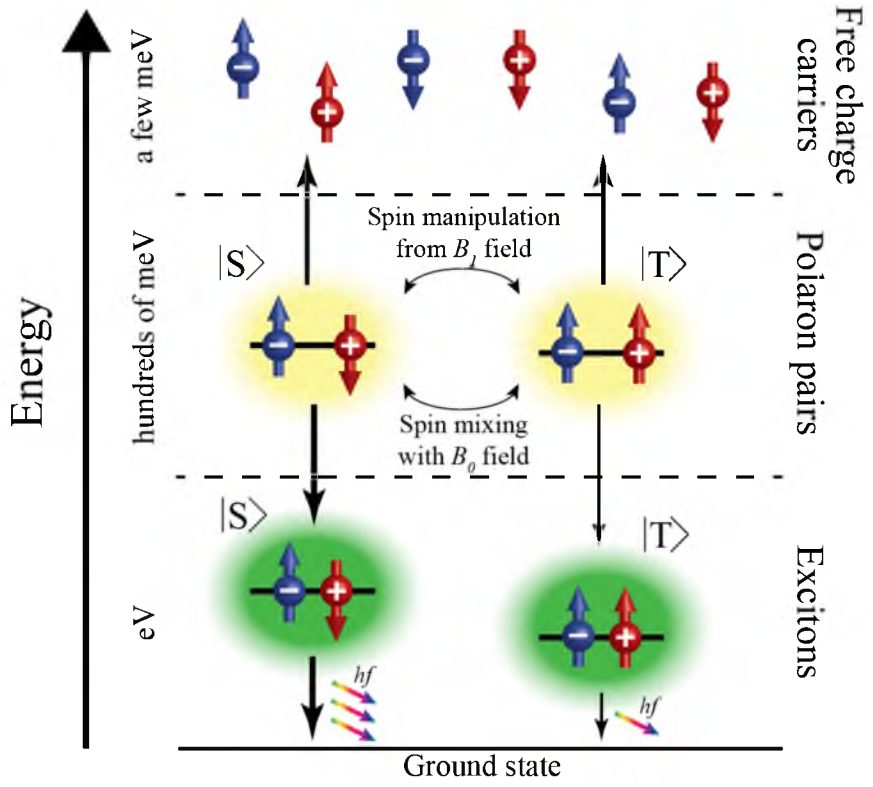


**Figure 2.11**. A simplified diagram of the polaron pair process. Once a polaron pair, made up of electrons (blue arrows) and holes (red arrows), is formed, it can exist either as a weakly spin-coupled pair state with (yellow halo, left side) or without (yellow halo, right side) high singlet content. Depending on the singlet content, polaron pairs recombine either into triplet or singlet excitons (green halos) or they dissociate back into the free charge carriers. A control of polaron pair spin-relaxation between singlet and triplet states can occur as a function of $B_0$, leading to a $B_0$ dependent dissociation rate of charge carriers. This makes the material resistance $B_0$ dependent, the cause of OMAR.

Historically, the idea that the polaron pair recombination process is the origin of OMAR and other spin-effects in organic semiconductors goes back to a proposal by Frankevich et al. [80], who applied the previously developed general Kaplan-Solomon-Mott model [141] to the organic materials.

In order to understand the polaron pair recombination process, we need to understand how charge carriers move through these materials. When electrons are excited (with light) or injected (with a voltage bias), they are free to move through

the LUMO states, creating a current. Next to the addition of electrons into the material through the electron injection layer (see Figure 2.5), there is also injection of holes into the valence band through the hole-injection layer. Due to Coulomb attraction, these electrons and holes can generate pairs with binding energies in the μeV to meV range. When the weakly coupled pairs form, their spin states align into energy eigenstates, which happen to be product states of two s=1/2 systems. Two of these [the $|\uparrow\uparrow\rangle$ and the $|\downarrow\downarrow\rangle$ states] are pure triplet states while the other two [the $|\uparrow\downarrow\rangle$ and the $|\downarrow\uparrow\rangle$ states] are states with singlet content. Thus depending on which of these states is assumed when a polaron pair forms, the polaron pair can recombine into singlet- or triplet-exciton states or dissociate into free charge carriers. For the formation of excitons, the polarons move onto a single molecular chain and their highly localized states will overlap. This also applies in principle to triplet excitons, but due to permutation symmetry, the two-particle wave function is anti-symmetric.

After the electron-hole pairs form excitons, there is a possibility for them to recombine either radiatively or nonradiatively. Since recombination within organic materials affects conductivity as it reduces charge carrier densities, we can observe recombination by observing a change in the current of the device.

OMAR due to polaron pairs takes place when an applied magnetic field influences spin relaxation of polaron pair states. Since the singlet polaron pair recombination rate is much faster than for triplets, the singlet and triplet polaron pair densities are different in the steady state. Thus, when singlet-to-triplet spin relaxation rates change, the steady state singlet-to-triplet ratios change as well.

This causes a change in the polaron pair dissociation rate, which causes the free charge carrier density and thus, the materials conductivity, to change as well.

Since the polaron pair mechanism was first proposed, several variations of this model have been developed [75-85] and the model has been experimentally scrutinized extensively [1,44,81,106,108]. While some of this work has led to controversial conclusions [63,87] as some experimental studies revealed OMAR behavior that could be explained by several of the spin-dependent mechanisms described above, an increasing number of studies in recent years has attributed room temperature spin-dependent processes to polaron pairs [106,122,143]. Most significantly in this regard has been the discovery that magnetic resonantly driven coherent spin-motion effects on conductivity have unambiguously identified the origin of room temperature spin-effects on resistance as being due to pairs of spins with s=1/2 [1,62,87,143,148-155]. This realization means that any process not involving pairs or involving spins other than s=1/2 can be excluded (single polaron process, triplet-triplet annihilation, triplet-polaron process, or even processes involving electronic magnetic field interactions). However, there is still some controversy with regard to the questions of whether these pairs of s=1/2 are unipolar or bipolar [146]. Yet many of these questions are irrelevant for predictions because they do not affect the quantum mechanical microscopic nature of the physical system responsible for OMAR, the weakly spin-coupled pairs of electron spins (note that hole spins are the spins of electrons, too). In essence, at this time it can be considered proven that polaron pairs in many polymer semiconductors (MEH-PPV, polyfluorene, superyellow-PPV, etc.)

control OMAR at room temperature.

## 2.5 The spin-Hamiltonian of charge carrier pairs

The spin-propagation of charge carrier pairs can be reduced to the spin-Hamiltonian because spin-orbit coupling makes electronic contributions nearly irrelevant. In the presence of a magnetic field, the spin-Hamiltonian of the spin pairs will include the interaction (Zeeman) terms $H_0$ with this field and the coupling terms $H_{coupling}$. In the presence of AC magnetic fields (e.g., under magnetic resonance), an additional perturbation Hamiltonian $H_1$ will appear. Combining all of the elements needed for the description of spin pairs, a single spin-pair Hamiltonian assumes the form

$$H = H_0 + H_{coupling} + H_1. \tag{2.1}$$

### 2.5.1 Zeeman interaction with externally applied magnetic fields

When a material is placed into a magnetic field, a splitting of the energy levels takes place, which is referred to as Zeeman splitting. The energy

$$\Delta E = h\nu = h\gamma B_0 \tag{2.2}$$

of the split spin-eigenstates that is proportional to the frequency $\nu$ of the transition is proportional to the strength of the externally applied magnetic field $B_0$ where $h$ is Planck's constant. The proportionality between the magnetic field and frequency can also be described by the effective Landé $g$-factor of the material since $\gamma = g\mu_B/h$, where $h$ is $h/2\pi$. The effective $g$-factor takes into account the small but distinct differences of the Zeeman splitting in a weakly spin-orbital coupled material from the electron's vacuum Landé-factor. This g-factor for free electrons is 2.0023193043615(5) [156]. For polaron states in organic semiconductors without impurities that artificially increase spin-orbit

coupling, the g-factor is typically shifted either higher or lower by values on the order of $10^{-3}$ [105]. The spin-orbit induced shift of the g-factor and the angular momentum state of the associated electronic state can reveal the chemical identity of a paramagnetic state in a condensed matter system [157].

The Zeeman splitting of the energy levels as a function of an applied magnetic field is shown in Figure 2.12. An increase in the magnetic field causes a greater splitting of the energy levels. The quantum number $m$ therein refers to the magnetic quantum number of the associated spin state, which can take integer values of $m=\pm j$ and $m=0$. The Zeeman interaction can be employed in order to probe spin states by bringing electromagnetic radiation in resonance with the energy splitting. Such an experiment is called magnetic resonance spectroscopy.

For the description of the Zeeman interaction with polaron pairs, we assign the two polarons within the polaron pair with labels a and b. They assume individual weakly

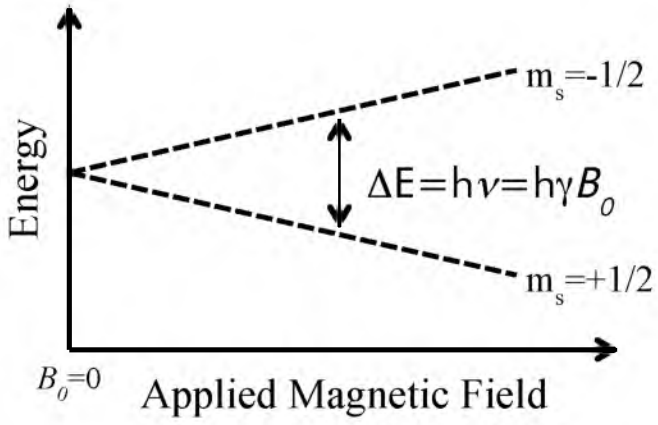


**Figure 2.12**. Zeeman-effect diagram. The diagram represents the absorption of electromagnetic radiation in order to induce a transition of a single spin-½ particle. The frequency of this transition is ν. When the electromagnetic radiation has a frequency $\nu$, the system is said to be at resonance and has a greater probability of inducing a transition. This energy is related to the permanent magnetic field $B_0$ as $\nu = \gamma B_0$.

coupled spin states $S_a$ and $S_b$, which interact with the permanent magnetic field $B_0$. This leads to an interaction Hamiltonian

$$H_0 = g_a\mu_B(\boldsymbol{S}_a \bullet \boldsymbol{B}_0) + g_b\mu_B(\boldsymbol{S}_b \bullet \boldsymbol{B}_0). \quad (2.3)$$

Here, $g_a$ and $g_b$ refer to the g-factors for polarons a and b, respectively, and $\mu_B$ is the Bohr magneton. Similarly, the Hamiltonian $H_1$ for the interaction between the polaron pair spins and the oscillating magnetic field $B_1$ assumes

$$H_1 = g_a\mu_B(\boldsymbol{S}_a \bullet \boldsymbol{B}_1) + g_b\mu_B(\boldsymbol{S}_b \bullet \boldsymbol{B}_1) \quad (2.4)$$

where, in contrast to the interaction with the static magnetic field $\boldsymbol{B}_0$, the magnetic field $\boldsymbol{B}_1$ is time dependent and potentially oriented in a different direction. This situation will be discussed in detail in section 2.6, which was about OMAR in the presence of an AC magnetic field.

### 2.5.2 Spin-spin interactions

Aside from the spin-interaction with externally applied magnetic fields, interactions within the charge carrier pairs or with other spin states (e.g., nuclear spin states) exist. These interactions include:

- **Exchange interaction** with Hamiltonian

$$H_{ex} = J\boldsymbol{S}_a \cdot \boldsymbol{S}_b \quad (2.5)$$

in which the exchange integral $J$ depends on the wave function overlap of the two interaction electron states. The wavefunctions of polarons are localized but usually beyond the size of monomer units. They can spread out over extended distances that are usually limited by kinks in the polymer chain [112] (which define so called chromophores). The absolute size (localization) of two interaction wavefunctions is not a sole measure for the exchange interaction strength as the

exchange integral is the convolution of two wavefunctions. (In essence, overlapping wavefunctions determine exchange interaction.) Exchange, an inherently quantum mechanical phenomenon that is due to the antisymmetric nature of Fermionic multiparticle systems, was discovered simultaneously by both Heisenberg and Dirac in 1926 [158,159].

Because exchange depends on overlap, its magnitude is determined by the separation and the localization of the charge carrier wavefunctions. As the electronic wavefunctions of singlet and triplet pairs must have significantly different permutation symmetries, singlet and triplet states experience different amounts of exchange coupling. A singlet state can be more compact, existing on the same molecular chain, increasing the exchange coupling between the pair partners. For a triplet state, where the Pauli exclusion principle makes pair partners more spread out on different molecular chains, exchange coupling is weaker and thus the energy for a triplet pair is lower. This effect becomes particularly pronounced for excitonic states in organic semiconductors whose singlet/ triplet splitting magnitudes range from hundreds of meV well into the eV range.

- **Dipolar coupling** with Hamiltonian

$$H_{dip} = D^d \frac{(S_a \cdot r)(S_b \cdot r)}{r^5} \tag{2.6}$$

in which the coupling constant $D^d = \frac{\mu_B^2 \mu_0 g_a g_b}{4\pi h}$ is determined by Bohr's magneton $\mu_B$ and the Landé-factors of the two pair partners $g_a$ and $g_b$ [147]. The constants $\mu_0$ and $h$ are the vacuum permeability constant and Planck's constant, respectively. The magnetic dipolar interaction is the Zeeman interaction of each

partner with the magnetic dipolar field of the respective other pair partner. The magnetic dipolar field arises from the magnetic moment of any charge particles (nucleus or electron) with its spin. The dipole contains a local magnetic field that drops off as $1/r^3$, where r is the distance between two magnetic dipoles. Two or more dipoles are coupled when they are close enough that their magnetic fields overlap. This can be a charge carrier with other charge carriers or a charge carrier with a nucleus. The dipolar coupling is weak in organic materials because it is dependent on $1/r^3$, so it drops off faster than the Coulomb force that binds the polarons. Here, only the interactions between charge carriers are referred to as the dipolar interaction. The interaction between the charge carrier and the nucleus are called hyperfine interactions, as discussed below.

- **Hyperfine interactions** with Hamiltonian

$$H_{hf} = \sum_{i=1}^{N} \left( \boldsymbol{I}_i \cdot \tilde{\boldsymbol{A}}_a \cdot \boldsymbol{S}_a + \boldsymbol{I}_i \cdot \tilde{\boldsymbol{A}}_b \cdot \boldsymbol{S}_b \right) \tag{2.7}$$

in which each of the surrounding $N$ nuclei couple with each of the two pair partners $a$ and $b$. The interaction matrices $\tilde{\boldsymbol{A}}_a$ and $\tilde{\boldsymbol{A}}_b$ are able to represent both the isotropic (Fermi contact) hyperfine interaction as well as the anisotropic (purely dipolar based) hyperfine terms. Hyperfine interaction causes an additional split in the paramagnetic states of the polarons, such that there is a separate resonance line for each $m_i$, the magnetic quantum number for the $i$th electron spin. Since there are $(2j+1)$ lines, a spin-½ particle is split by the hyperfine interaction into 2 lines while a spin-1 particle has 3 lines. The nucleus that is arguably most relevant in organic materials is the all-abundant hydrogen, which has a nuclear spin of ½. Deuterium, the second most abundant hydrogen isotope has a nuclear spin of 1.

Hyperfine fields have turned out to be integral for the development of an understanding of spin-dependent mechanisms in organic materials [1,66,81,108,138], in particular for OMAR [81,160]. The manipulation of hyperfine fields (by the choice of chemical compounds, deposition morphologies, or isotopic composition) has provided not only proof for their role on electronic processes [1,108,161], but also avenues for the optimization of technical (organic spintronics) applications. For instance, by replacing a hydrogenated polymer with a deuterated polymer, which has a smaller hyperfine fields, narrower OMAR curves were obtained by Nguyen et al. in 2007 [160]. This was one of the first direct demonstrations that hyperfine fields directly affect OMAR curves. Bergeson et al. in 2008 controlled the chemical composition of the material in order to change the hyperfine strength and found a significant change of the organic magnetoresistance curve [75], confirming previous results that the hyperfine field does in fact define the width of OMAR functions.

Note that the hyperfine interaction in general occurs between a single polaron spin and many ($N$) nuclei. For practical applications of $H_{hf}$, it has been shown that the assumption of hyperfine interaction with very few spins [162-164], and even a single nuclear spin, can lead to good predictions for the OMAR effect.

When all the spin-spin interactions that are relevant for charge carrier pairs in organic semiconductors are combined, the general Hamiltonian of spin pairs assumes the form

$$H_{coupling} = H_{ex} + H_{dip} + H_{hf}. \tag{2.8}$$

There are additional contributions that could be relevant for the spin Hamiltonian

of polaron pairs such as spin-interaction terms of pair partners with spin states of electronic states outside of the pair or the interaction with magnetic field contributions due to the nuclear quadrupole moment. However, at this time, no experimental evidence exists that these effects can significantly influence the conductivity in organic semiconductor materials, and they are therefore not further pursued.

## 2.6 OMAR in presence of alternating current magnetic fields

With the Hamiltonian $H = H_0 + H_{coupling}$ given, we can now consider how a radiation induced change of spin states, and thus the magnetoresistance, takes place. In order to describe this, we consider the additional contribution $H_1$ to the pair Hamiltonian that is given by Eq. 2.4. Therein, $\boldsymbol{B_1 = B_1^A \sin(\omega t)}$ is the harmonically oscillating driving field with amplitude $\boldsymbol{B_1^A}$ and frequency $\boldsymbol{\omega}$.

### 2.6.1 Electron spin resonance

As already indicted in section 2.5, electron spin resonance involves the application of a constant magnetic field $\boldsymbol{B_0}$, which lifts the degeneracy of spin states due to Zeeman splitting, while applying an oscillating field. When the photon energy of the oscillating field equals the Zeeman splitting ($\hbar\omega = \hbar\gamma B_0$, with $\gamma$ being the gyromagnetic ratio and ħ being the Planck constant), the magnetic resonance condition is met, and the applied oscillating magnetic field will change the spin state of the paramagnetic centers that are brought into magnetic resonance. For the example of X-band irradiation (~10GHz) and weakly coupled spins with s=1/2 and a Landé factor close to 2, (e.g., for polaron states in organic semiconductors like MEH-PPV whose gyromagnetic ratio is

$\gamma$=28.03 GHz/T [3]), this condition is met around $B_0 \approx 350$mT. For lower magnetic fields (< 10 mT), the Zeeman splitting is within the radio frequency (*RF*) range [165].

The argument for magnetic resonance solely based on the simple quantum mechanical Zeeman-to-photon-energy equivalence does not explain why magnetic resonance occurs only when the directions of $\boldsymbol{B_0}$ and $\boldsymbol{B_1}$ are mutually perpendicular. This requirement can be derived both quantum mechanically but also classically, following the application of Bloch's equations [128]. In the classical picture, the net-magnetic moment of a single spin or a spin-ensemble will interact with the applied $\boldsymbol{B_0}$- and $\boldsymbol{B_1}$-fields as illustrated in Figure 2.13. Therein, the four sketches display Bloch-sphere representations of the magnetization (green arrows) in absence (a, b) and presence (c, d) of $\boldsymbol{B_1}$ from the viewpoint of a laboratory frame (a, c) as well as the viewpoint of an observer who rotates at the Larmor precession frequency of the magnetization (b, d), the so-called rotating frame Bloch sphere representation. Bloch-spheres are used to represent spin-states graphically. Since spin states with s=1/2 are elements of the special unitary group SU(2) but any sphere represents rotations of the special orthogonal group SO(3), an implicit mapping of the SO(3) onto SU(2) is assumed. In the presence of a magnetic field $B_0$ pointing into a direction $\hat{z}$, the component of the magnetization perpendicular to $B_0$ ($\hat{z}$) will precess in the x-y-plane, a phenomenon called Larmor oscillation (a). When the same situation is observed from a rotating viewpoint, with the rotation frequency being equal to the Larmor frequency, a magnetization that does not precess at all is observed (b). Thus, in the rotating frame, there is no magnetic field $B_0$ and the static magnetic field is "transformed away." When both $B_0$ and $B_1$ are applied at the same time but with mutually perpendicular orientations and $B_1$ rotates also at the Larmor frequency, the

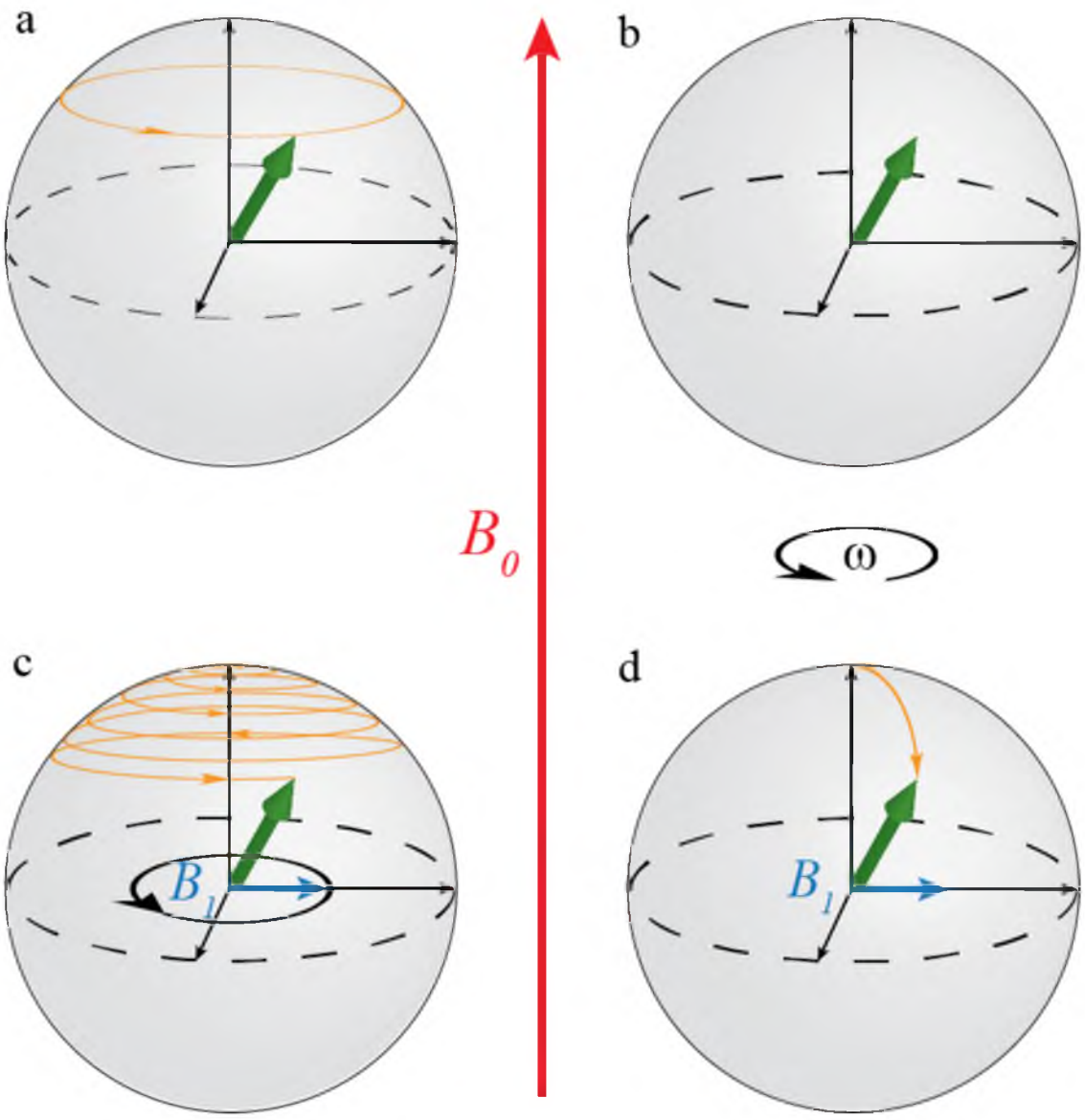


**Figure 2.13**. Illustrations of the propagation of magnetization (green arrow) in a Bloch sphere representation in absence (a, b) and presence (c, d) of magnetic resonance. For details see text.

rotating frame $K'$ will display a constant magnetic field $B_1$ within the $\hat{x}' - \hat{y}'$-plane (d). Thus, a Larmor precession around $B_1$ will take place, which looks from the laboratory viewpoint like a "cork-screw" propagation of the magnetization (c). The Larmor precession around $B_1$ in the rotating frame is called the Rabi nutation or Rabi oscillation [166]. It continues for as long as the magnetic resonance conditions are fulfilled and it is the reason for the resonant change of a spin state, e.g., from an up state to a down state during the application of magnetic resonance conditions.

Magnetic resonance spectroscopy is based on the manipulation of electron or nuclear spins through the effect illustrated in Figure 2.13. Traditionally, the detection of magnetic resonance is conducted through inductive coupling of the propagating macroscopic magnetization. This approach implies an inherent volume sensitivity of traditional magnetic resonance spectroscopy as absolute magnetization depends on the number of spins in a given sample. More importantly, thermal polarization usually also plays an important role. When magnetic resonance experiments are carried out on equilibrated spin ensembles, polarization can be very small if not minute as Zeeman energies even at intermediate to strong magnetic fields range from the μeV range for electrons all the way to the neV range for nuclei. For room temperature magnetic resonance spectroscopy of spin states in quasi-two-dimensional semiconductor thin films, this means traditional inductively detected spin spectroscopy becomes all but impossible. This problem with electron spin resonance (ESR) spectroscopy has been one of the most important reasons why semiconductor spectroscopy using spin-selection rule-governed spin detection techniques have been pursued for a long time [149, 139]. Electrically and optically detected magnetic resonance spectroscopies (EDMR and ODMR, respectively)

are based on the detection of electronic transitions rates (either charge current for EDMR or emissive recombination rates for ODMR), which are governed by spin-states. These methods are usually many orders of magnitude more sensitive than ESR to the point that the detection of individual electronic transitions is possible (both EDMR [167-170] and ODMR [171,172] have demonstrated single spin sensitivity). Moreover, many spin-dependent transitions do not depend on thermal polarization but other observables, such as permutation symmetry of spin-pairs [80,133].

### 2.6.2 Electrically detected magnetic resonance

Electrically detected magnetic resonance (EDMR) spectroscopy is based on the detection of magnetic resonance through changes in the current in a condensed matter device. The first EDMR experiment was reported by Maxwell and Honig in 1966 [173], and the first spin-dependent recombination signals were found by Lepine in the 1970s [142]. Also, many experimental [97,161,166,174] and theoretical [4,137,149,175] studies have either utilized this experiment for spectroscopy of paramagnetic defects or have aimed at developing an understanding of the mechanisms causing these signals. Most all of these experiments were conducted as continuous wave (cw) EDMR experiments. For cwEDMR, spin-dependent rates are monitored while the magnetic field $B_0$ is swept adiabatically in the presence of a cw (continuous irradiation at constant intensity) RF or microwave field. While for ESR spectroscopy, cw experiments had been mostly abandoned in favor of pulsed (p) experiments (transient, time-domain spectroscopy), the first transient EDMR experiments were not performed until 1999 when Hiromitsu et al. presented time domain EDMR [95] on phtalocyanine diodes. While these experiments provided insight into the dynamics of spin-dependent charge carrier recombination rates

during and after magnetic resonant excitations, the first pEDMR experiments that provided access to the dynamics of coherent spin motion were not reported until 2002 [176-178].

CwEDMR, similar to ESR, allows for the determination of Landé g-factors, spin relaxation rates, and coupling factors, yet dynamic information about a spin-dependent process is difficult to obtain. Basically, cwEDMR can reveal anything that can be determined from the line-shapes of the signal [179]. For the experiments in this dissertation, cwEDMR measurements are conducted either as adiabatic sweeps of the magnetic field with a constant frequency $\omega$ of the $B_1$ field or as sweeps of $\omega$ in the presence of a static field $B_0$. For some cwEDMR experiments in this dissertation, as for most cwEDMR reported in the literature, lock-in detection schemes are employed for which the nominally static field $B_0$ is modulated at a small amplitude (compared to $B_0$). This approach allows for a drastic noise reduction as well as a selective observation of harmonic components within the dynamics of the investigated process. Due to the finite frequency range of any modulation scheme, the frequency range that is accessible by these means is limited. For the study of the influence of magnetic resonance on OMAR, no lock-in detection will be employed and the change of the OMAR current in response to spin manipulation will be observed directly.

Because of the limitations of cwEDMR, pEDMR spectroscopy has gained increasing attention in recent years as this technique allows for access of the dynamics of the observed spin-dependent processes on a much broader frequency range, including the time domain where coherent spin-motion occurs. The first theoretical description of ns-domain pEDMR spectroscopy on spin-dependent processes based on intermediate pairs

was given by Boehme and Lips in 2003 [157]. They proposed the use of short (lower ns range) and powerful resonant electromagnetic pulses ($B_1$ field in the lower mT range) to coherently alter the investigated paramagnetic state. Following the magnetic resonance illustration given in Figure 2.13, the pulse rotates the spins within the rotating frame from the initial state within the plane perpendicular to $B_1$. The orientation of the magnetization at the end of the pulse depends on the length of time of the pulse and its strength (the amplitude $B_1$). On resonance, the changed currents after the pulse caused by the changed spin state will reveal the coherent spin motion during the pulse, when the current or the time-integrated current (= the amount of charge transmitted by the device in response to the pulse excitation) is measured as a function of the length of the applied pulse. Thus, measuring pulse-length dependencies with ns-resolution reveals the dynamics of coherent spin-motion with ns resolution. Measuring the dynamics of spins involved in spin-dependent processes with pEDMR opens up access not just to information about spin-dephasing and spin-relaxation times but also to the nature of the observed electronic transitions.

As pointed out above, the observation of spin states via spin-selection rules allows for spectroscopy with much greater sensitivity, down to the single spin level for both ODMR [171,172] and EDMR [167-170], while ESR is typically (for the widely used X-band regime) sensitive to only about $10^{10}$ spins [180]. Because of the small magnitude of nuclear magnetic moments, NMR is even less sensitive, usually to about $10^{15}$ spins. EDMR is also useful because it can be used at almost any magnetic field since its observable does not depend on polarization. Thus EDMR signals can be measured at very small magnetic fields down to Zeeman energies that are of the order of the magnetic

resonant line widths. An illustration of the advantage of EDMR can be given by the measurement of Zeeman splitting by EDMR shown in Figure 1.5 [3].

### 2.6.3 Conducting OMAR and EDMR measurements

Experimentally, it can be challenging to conduct the measurement of spin-dependent currents in semiconductor devices in the presence of strong high-frequency electromagnetic fields as these fields must not only be homogeneous in order to prevent a fast artificial dephasing of the probed spin-ensemble when coherent spin-motion is observed, but at the same time, they must not couple inductively to the electric sample because if they do, they will induce artifact currents that can bury the spin-dependent currents of interest. A distortion of the homogeneity of $B_1$ is created whenever a metal is placed into a microwave field. This effect is because free electrons in a metal move rapidly when exposed to a microwave field and create an electric potential, which is essentially the same effect that will cause a metallic object in a microwave oven (e.g., cutlery) to spark. In order to avoid this effect, one can fabricate metal layers within electric devices on size scales below the skin (penetration) depth of the given material. The skin effect describes the distribution of alternating currents in a conductor. The skin depth is the exponential penetration depth of electromagnetic fields into the conductor, it is the depth by which the wave amplitudes fall to 1/e of their surface magnitudes [181]. It is $\delta = \sqrt{2/\mu\sigma\omega}$, where $\mu$ is the permeability of the conductor, $\sigma$ is the conductivity, and $\omega$ is the frequency of the applied electromagnetic field [182]. For widely used aluminum contacts and X-band frequencies, the skin depth is on the order of microns, even at liquid $^4$He temperatues (~4K). This means that while very thin bonding wires (diameters on the

order of 20 microns) are still capable of significant distortions of $B_1$, lithographically prepared thin-film wires (~100nm thickness) will cause hardly any measurable distortion at all.

### 2.6.4 Electrically detected spin-Rabi oscillation

A simple pEDMR experiment that can be applied in order to investigate spin-dependent transitions is a single-pulse Rabi-oscillation measurement, an experiment similar to ESR-detected transient nutation measurements. This experiment involves measuring the single on-resonance pulse response of a spin-dependent current as a function of the pulse length $\tau$. When a short pulse is applied to the sample, the spin rotates by only a few degrees from the z-axis. As the pulse length increases, the spin rotates further from the +z–direction until it ultimately returns to its original position and then the process repeats. Eventually, the increasing pulse length leads to the imprint of the spin-Rabi nutation into the detected current changes after the pulse, and the Rabi frequency $\Omega$ is revealed. For the measurements reported in the following, this kind of experiment was utilized in order to accurately measure the field strength $B_1$ of the radio frequency coil used for the presented experiments.

While the electrical detection of spin-Rabi oscillations is one of the simplest pEDMR experiments [33], it can give us information about the spin coherence and coupling strengths involved in the detected spin-dependent process. While a single harmonic Rabi oscillation component $\Omega=\gamma B_1$ in the conductivity of a given sample is indicative of a spin-dependent process involving charge carriers with spin s=1/2, other harmonic components can exist that give information about the material and nature of the spin-dependent process responsible for the observed signal. For instance, a $2\gamma B_1$

contribution to a Rabi nutation corresponds to an in-phase double harmonic of a beat oscillation between two spins with s=1/2, while a frequency of nearly zero corresponds to the out-of-phase harmonic of the same process [154]. Both of these contributions are indicative of weakly spin-spin coupled intermediate pairs being responsible for the observed signal [149]. A frequency of $\sqrt{2}\,\gamma B_1$ is indicative of dipolar-coupled intermediate pairs [149,154]. Thus, determining the harmonic components of spin-Rabi oscillations allows for the identification of both the strength of the applied AC field $B_1$ as well as the coupling nature and coupling strengths of spins involved in the conductivity of a semiconductor sample.

### 2.6.5 Magnetic resonance line-shapes and EDMR

When the frequency of an AC field is off resonance with the Larmor frequency of paramagnetic states involved in spin-dependent transitions, the associated EDMR vanishes. The functional dependence of this signal on the Larmor frequency, or equivalently, the signal dependence on the static magnetic field $B_0$ is called the EDMR resonance line-shape. EDMR signals typically become maximal when $|\omega-\omega_0|$ is zero and their decrease when $|\omega-\omega_0|$ increases can depend on various parameters. When a material is entirely homogeneous, a long (longer than coherence times of the involved spin states) excitation will produce a Lorentzian whose width is solely governed by the magnitude of $B_1$ of the driving field [157], an effect called power broadening. However, as EDMR signals are typically due to many paramagnetic centers (materials inhomogeneities), the character of the involved spin species (e.g., pairs versus excitons or single carriers) as well as coupling types can affect line-shapes. When these properties are subject to disorder, the random nature usually leads to Gaussian distributions. For very short,

coherent spin excitation of length $\tau$, line-shapes also assume a Lorentzian shape whose width is determined by the excitations distribution of the applied pulse, which means that the Lorentzian line width is proportional to $\tau^{-1}$. Similarly, homogeneous broadening can also be caused by spin-relaxation times. Inhomogeneous broadening due to disordered local environments usually involves g-factor distributions and the presence of random local magnetic fields caused by the magnetic moments of nuclei with nonvanishing spins. In organic semiconductors, which are hydrocarbon compounds, these so called hyperfine fields are usually caused by hydrogen.

Similar to ESR spectra, line-shapes of EDMR spectra can strongly depend on the experimental conditions under which they are measured. Usually, several line-shape effects (homogeneous and inhomogeneous) exist at the same time and the actual resonance lines are determined by the broadest line-shape effect. When several line-shape effects cause broadening on similar scales, complicated line-shapes evolve, which typically result in convolutions of Gaussian and Lorentzian functions. These are so-called Voigt lines.

### 2.6.6 OMAR in presence of an AC magnetic field

As discussed in 1.2, when a $B_1$ field is applied to an organic semiconductor in which a spin-dependent spin s=1/2 pair process controls the current while $B_0$ is swept, a dip in the current around the resonant frequency can be observed because of the mixing between singlet and triplet polaron pair states. This effect is due to the random hyperfine fields [138] caused by hydrogen nuclei (protons) [183]. When polaron pairs experience this ac-driving field, the polaron spins rotate around the field. As the strength of the driving field increases, the indirect interactions between the pair partners and eventually

between pairs as controlled by the resonant driving field, evolve. At weak driving fields ($B_1 \ll B_{hyp}$), individual, weakly coupled spins rotate independently from each other, mixing singlet and triplet polaron pair states. As the intrinsic coupling between pairs is weak, a measurement of the FFT of a Rabi oscillation reveals a single nutation frequency. In a graphical representation of an EDMR spectrum, this regime is given when the Lorentzian line width caused by power broadening is much smaller than the Gaussian line-shape of the resonance signal that is due to materials inhomogeneities.

When the driving field strength increases such that $B_1 \approx B_{hyp}$, a beat signal appears in the FFT because the relative motions of pair partners within the individual pairs becomes significant. This simultaneous rotation occurs when $B_1$ is strong enough to be on resonance with the fields of both pair partners due to power broadening. Under these conditions, the Rabi oscillation displays a beat oscillation as mentioned above [1]. In a graphical representation, this regime is given when the Lorentzian line width caused by power broadening exceeds the spectral broadening due to disorder.

When the $B_1$ field increases even further such that $B_1 \approx B_0 > B_{hyp}$, another qualitatively distinct spin-motion regime evolves where all the pairs within the materials are indirectly coupled through the applied AC magnetic field. A simultaneous rotation of all spin in all pairs evolves, and a collective spin motion regime, the so-called spin cooperativity regime, appears [4]. This driving-field strength domain has only recently been explored theoretically by Roundy and Raikh [4] and the physics described therein is similar to the well-explored Dicke effect, known for electric dipole radiation. The experimental scrutiny of these theoretical predictions of polaron pair spin motion as well as their highly significant consequences on the polaron pair recombination dynamics are

at the focus of this dissertation.

### 2.6.7 Spin-cooperativity

The term "Dicke physics" refers to the description of a system of two atoms interacting via a common photon field [184] given by R. H. Dicke in 1954. While a single atom can spontaneously decay, the two interacting atoms have a different decay rate from two noninteracting atoms. Depending on the strength of the interaction, the decay splits into two channels, a fast superradiant mode and a slow subradiant mode, corresponding to a weak and strong interaction, respectively. Similar to this, the Dicke effect describes the collective decay of excited atoms when the interaction between the atoms is strong.

When Baker et al. began measuring EDMR of organic semiconductor devices at low magnetic fields ($B_0 \approx B_{hyp}$) [3], the most interesting observation was possibly the strongest confirmation of the polaron pair model, which predicted EDMR signals are nearly unchanged with weak spin polarization. Another insight made in the course of these experiments has been that this $B_0$-independence of the EDMR signal, which stretches over several orders of magnitude, is not given when $B_0 < B_{hyp}$, which was observed below $B_0 \sim 1.5$mT for the organic semiconductor (MEH-PPV). When $B_0 < B_{hyp}$, spin-relaxation rates increase strongly and the spin-flip rates induced by the resonant AC fields becomes comparatively weak. Thus, spin-flip rates in the presence and absence of magnetic resonance will not be different and the EDMR signal will disappear.

Similar to the change from $B_0 < B_{hyp}$ to the $B_0 > B_{hyp}$ regime, spin-flip rates change when $B_1 < B_{hyp}$ is changed to $B_1 > B_{hyp}$ and even more when $B_1 < B_0$ is changed to $B_1 > B_0$ so that $B_1 > B_0 > B_{hyp}$. When the driving field becomes larger than the hyperfine coupling, a

spin-blocking mode similar to the superradiant mode of the Dicke effect is formed. This leads to a strong increase of the triplet density throughout the spin-pair ensembles, which quenches the recombination rate. This collective response of the electrons and holes is analogous to a decrease in the singlet content, creating long-living modes that cannot recombine.

The prediction made by Roundy and Raikh about spin-dependent recombination in the presence of strong ac driving fields has been based firmly on the assumption that the electrically detected spin-dependent transitions are governed by polaron pairs. Roundy and Raikh's study does not address, however, whether spin-cooperativity effects, which undoubtedly could also exist for bipolaron pairs, would lead to identical spin-dependent rate effect. Thus, verifying the theoretical predictions at high powers provides another confirmation of the validity of the polaron pair model, yet it does not implicitly refute the bipolaron model. Nevertheless, it contributed to the settlement of the controversy over which pair model should be used for spin-dependent transitions in organic materials. Observation of the predicted rate quenching signal at high driving fields also provides access to a variety of quantitative parameters about the polaron pair systems such as spin-relaxation rates, recombination rates, and dissociation rates in the given organic semiconductor materials.

# CHAPTER 3

# SAMPLE PREPARATION METHODS AND EXPERIMENTAL TECHNIQUES

## 3.1 Sample preparation

### 3.1.1 Cleanroom techniques

The experiments presented in this dissertation required the availability of geometrically and chemically well-defined, clean, and reproducible organic semiconductor devices that had to allow for the application of homogeneous $B_0$ and $B_1$ fields. For the fabrication of these devices, the University of Utah Nanofabrication facilities were used and which provide class 100/1,000/10,000 cleanroom space as well as packaging and test areas. The recently (2012) commissioned 18,000 square foot facility offers all processes, equipment, and expertise needed to design and implement devices on the micro- and nanoscale. Capabilities of the University of Utah Nanofabrication facilities include lithography mask design and fabrication, a broad variety of thin-film deposition techniques, device patterning, and dicing capabilities. These facilities were utilized for all sample preparation steps that did not involve organic semiconductor layer depositions, including all lithography steps as well as the deposition steps of most metals and inorganic insulator layers using physical and chemical thin-film deposition techniques. All organic semiconductor layers were deposited in glove box facilities within the Department of Physics and Astronomy.

The preparation of the organic semiconductor diode sample templates involved the following preparation steps:

(i) **Substrate clean**. A glass substrate with a deposited, approximately 100nm thick layer of indium tin oxide (ITO) that was commercially acquired (Delta Systems) was cleaned in a bath of acetone, followed by a bath of isopropanol (IPA). For every bath of acetone mentioned in the following, assume a bath of IPA immediately after to wash away the acetone.

(ii) **Photolithography**. Since the active region of the device was determined by the bottom and top contacts, the ITO had to be removed from almost the entire substrate except for the active region. Photolithography was used to define this region. For this, a layer of photoresist was spin coated onto the entire substrate. Thereafter, UV light was used to expose the photoresist and a photolithography mask was used to block the light from exposing the regions where photoresist was to remain. Once the photoresist was exposed, the substrate was soaked in a developer, which washed off only the exposed photoresist while leaving the rest to cover the substrate. For the ITO removal, the photoresist covered the active region, which in turn ensured that the ITO in that region was not removed from the substrate during the ITO etch. A layer of Shipley Microposit S1813 photoresist was used for the lithography step, developed by the Shipley 352 developer.

(iii) **ITO etch**. To remove the ITO, an Oxford Plasmalab 80 etcher reactor was used. This instrument employs a reactive ion etching (RIE) process in which an Argon plasma removes the ITO from the surface everywhere except over the active

region where the photoresist is covering. In order to determine when the ITO had been removed, we measured the resistance of the surface. ITO has very low resistance when thick, while glass has near-infinite resistance. As the ITO layer thins, its resistance will increase. Not removing the ITO completely will allow for shorts between the anode and cathode. Note that photoresist has near-infinite resistance as well, so once the ITO is removed, the photoresist was washed off in a bath of acetone.

(iv) **Metal deposition**. Once the active region was defined by the ITO, the contact pads of the template needed to be created and subsequently connected to the sample active region. To do this, a layer of metal was deposited, usually aluminum. This again was accomplished by employment of another photolithography step. In contrast to the ITO structuring, a photolithography mask was used that allowed for the removal of the photoresist wherever the metal needed to remain on the substrate. The metal was deposited using either a Denton Sputterer or a Denton metal evaporator. The Sputterer uses an Argon plasma in order to eject atoms from a metal target, which are then bombarded onto the substrate where they form new bonds. The metal evaporator heats a crucible containing the metal until metal gas evaporates and again forms contact with the substrate surface.

After the metal deposition, the metal covers the entire surface of the substrate. In order to then geometrically define the desired metal contacts, the previously deposited photoresist was removed by using acetone, which caused the metal to remain only where there was no photoresist before the metal deposition.

This process is called lift off and was accomplished by placing the substrate into an acetone bath and then placing everything into a sonicator, which vibrates the acetone bath and greatly accelerates the lift off of the photoresist and the undesired metal areas. Once the lift-off was finalized, the contact pads and the wires connecting the pads to the active region were in place. Examples for sample templates after this fabrication step are shown in Figure 3.1 (a).

(v) **Silicon nitride deposition**. In order to create an insulating layer between the bottom and top contacts, a layer of silicon nitride ($SiN_x$) was deposited using a plasma enhanced chemical vapor deposition process (PECVD) as allowed by the Oxford Plasmalab 80 PECVD reactor. The layer had to be thick enough to be a good insulator, usually around 200nm. After deposition, the $SiN_x$ had to be removed over the contact pads and the active region. These $SiN_x$ layer "windows" then acted as the defining region for the active area of the device as well as the sample contacts. To create these "windows," another photolithography step was needed where a mask was used that had openings to expose the regions where no $SiN_x$ was allowed. After washing away the photoresist with the developer, the Oxford Plasmalab 80 was used again in order to etch the $SiN_x$, this time using a gas of SF6. After the $SiN_x$ "windows" had been created and tested using an ohmmeter ($SiN_x$ and photoresist have nominally infinite resistances and the ITO and metal have low resistances), the photoresist was washed away in an acetone bath.

(vi) **Dicing**. Once the templates had been completed, they were diced into the appropriate sizes using a Disco DAD641 diamond dicing saw. The saw uses a

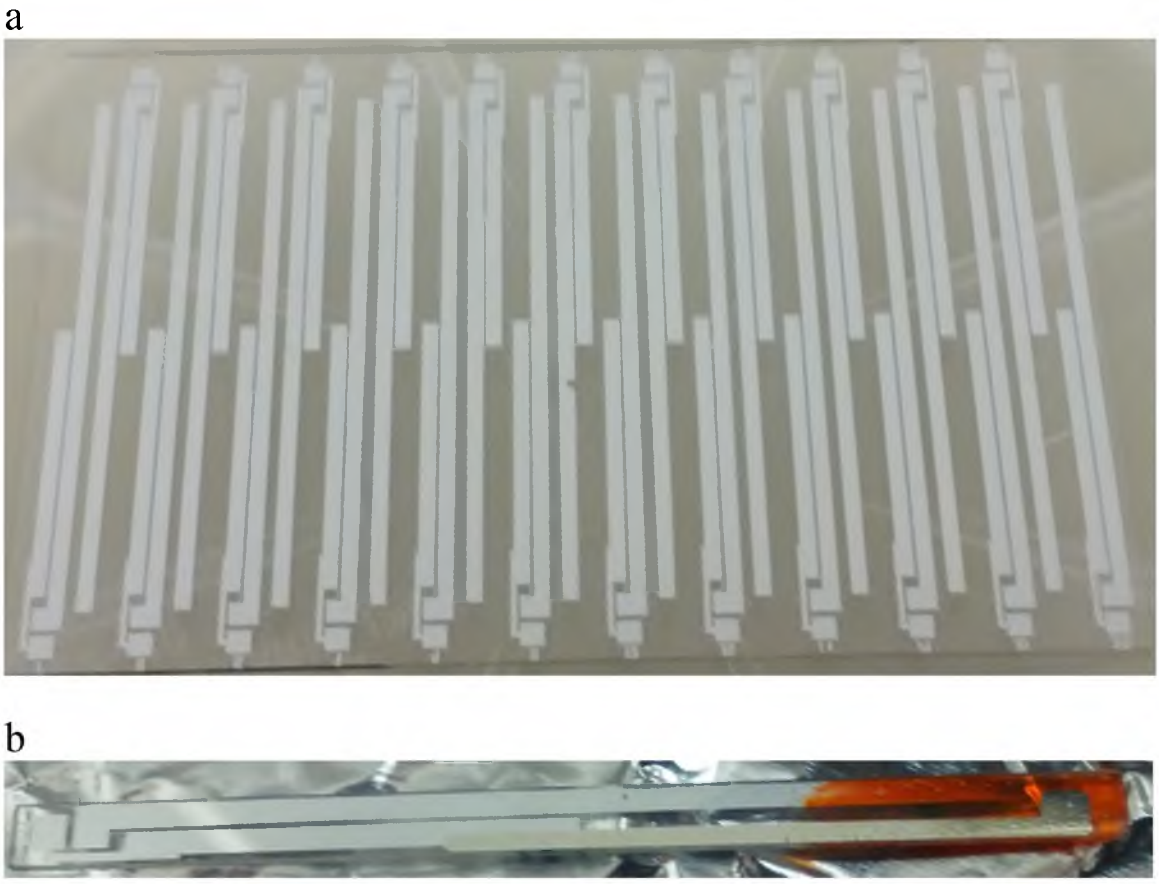


**Figure 3.1**. Sample templates and a processed sample for the "stick-like" sample geometry that can be used for pEDMR measurements in cylindrical X-band EPR resonators (as manufactured by Bruker Inc.) as well as in RF coils with small diameters used for the measurements presented in Chapter 4. (a) Photo of sample templates before the insulating layer deposition and dicing steps that displays a glass substrate of dimensions 50x75x0.5mm$^3$ deposited with layers of ITO and Al. (b) Photo of a finished MEH-PPV diode device with glass substrate size of 50x3.2mm$^2$ and sample size of 2X3mm$^2$ that fits into the sample contact/rod setup of the EPR laboratory. The stack of organic conductors and semiconductors was deposited onto the template in a glovebox environment with controlled inert atmospheric conditions.

diamond blade spinning at 30krpm and moves at about 3.5mm/s.

### 3.1.2 Deposition of organic semiconductor layers

For the organic diode samples used here, vertical (perpendicular to the substrate surface) device stacks of ITO/Poly(3,4-ethylenedioxythiophene) Polystyrene sulfonate (PEDOT:PSS)/MEH-PPV/Ca/Al were used. Following the template fabrication described in section 3.1.1, the sample substrates made in the Utah Nanofab, covered with the ITO layers, Al wires, and $SiN_x$ insulator, were subjected to the following processing steps:

(i) **Hole-injection layer deposition**. After a brief clean of the template surface, an approximately 100nm thick layer of Poly(3,4-ethylenedioxythiophene) Polystyrene sulfonate (PEDOT) was deposited onto the ITO. PEDOT:PSS dissolves in water and after deposition via a spin-cast process, must be baked at $150^0$C to remove the water. This step was done outside of the controlled glovebox environment in order to avoid excess water vapor.

(ii) **Insertion into Glovebox**. The deposition of most organic semiconductor thin films (in fact, all organic films used here expect for the PEDOT:PSS) requires a well-controlled inert glovebox environment because of the degradation that occurs when these materials encounter atmospheric oxygen. The glovebox used in this study for the preparation of the samples was filled with a nitrogen gas, and the $O_2$ as well as the $H_2O$ levels were carefully monitored and kept at less than 0.1ppm. For the introduction of the PEDOT:PSS covered sample templates into the glovebox, a load lock system that is attached to the glovebox was used as soon as the PEDOT:PSS films were dry.

(iii) **Deposition of active organic semiconductor layer**. Once the PEDOT:PSS films

were inserted into the glovebox, an approximately 100nm thick layer of poly[2-methoxy-5-(2-ethylhexyloxy)-1,4-phenylenevinylene] (MEH-PPV)[1], was deposited from a toluene solution using a spin-coating process. The deposition of the active organic layer was then again followed by a low-temperature ($100^0$C) baking step in order to remove the remaining solvent.

(iv) **Deposition of electron injection layer**. Following the MEH-PPV layer deposition, the top metal contact for electron injection was evaporated. The contact consisted of a thin (5nm) layer of Ca and then a thicker Al contact (125nm) to finish the process. An example of an OLED device is shown in Figure 3.1(b) for the stick-like substrate shape used for the AC magnetoresistance measurements discussed in Chapter 4. Other sample geometries as those used for the study of magnetic field inhomogeneities discussed in Chapter 5 and shown in Figure 3.2(a).

(v) **Electric verification of the diode devices**. Once devices were made, they were tested electrically through measurement of their I-V functions. These measurements yielded the overall device characteristics while allowing for an overall visual inspection of the light output of the OLED device, as shown in Figure 3.2(b).

(vi) **Encapsulation**. When a working device had been verified, a final encapsulation step was needed such that the device could be taken out of the inert glovebox environment into an oxygen-rich environment. For this step, two gels (Araldite 2011 A/B) were mixed to form an epoxy that hardened quickly and did not allow

[1] The hydrogenated MEH-PPV was provided by American Dye Source, Inc.

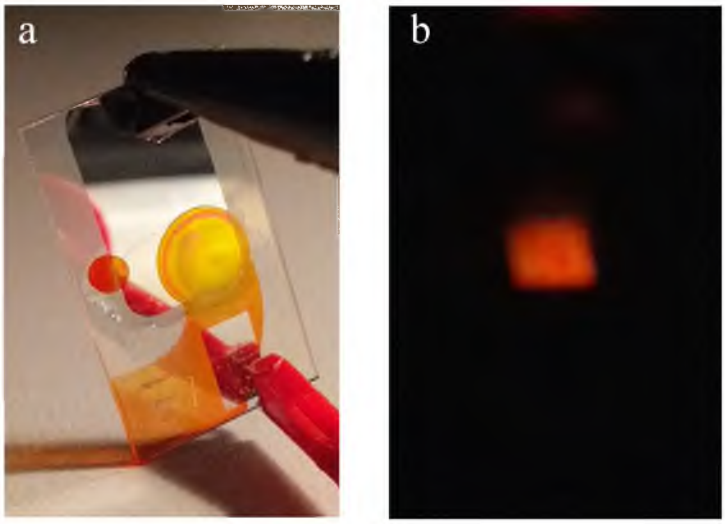


**Figure 3.2**. OLED template with organic device and photo of electroluminescence. (a) Device as used for the experiments discussed in Chapter 5 showing an organic semiconductor device stack deposited onto a glass substrate. The substrate size is $10x20mm^2$, the active device area in the center of the substrate is $1x1mm^2$. (b) The diode displays electroluminescence when an appropriate forward voltage is applied. For MEH-PPV diodes, the emitted light is orange.

air to penetrate into the device thereafter. The gels were carefully applied to the sample surfaces, covering the parts that contained the organic semiconductor layers without covering the sample's contact pads.

An example of a completed organic diode device sample under operating conditions is displayed in Figure 3.1(b). The electroluminescent emission from the rectangular active area of the sample is visible. For the experiments on spin-dependent currents presented in this dissertation as well as for other, previously published [106,153,155,166] work, the vertical diode stack devices described above have been used. In order to verify the successful preparation of a diode device, an electrical characterization was carried out. For this, current-voltage functions (also called I-V curves) were measured using a Keithley 2400 source meter and the Labview program Labtracer. Figure 3.3 displays a set of current-voltage (I-V) functions obtained for 7

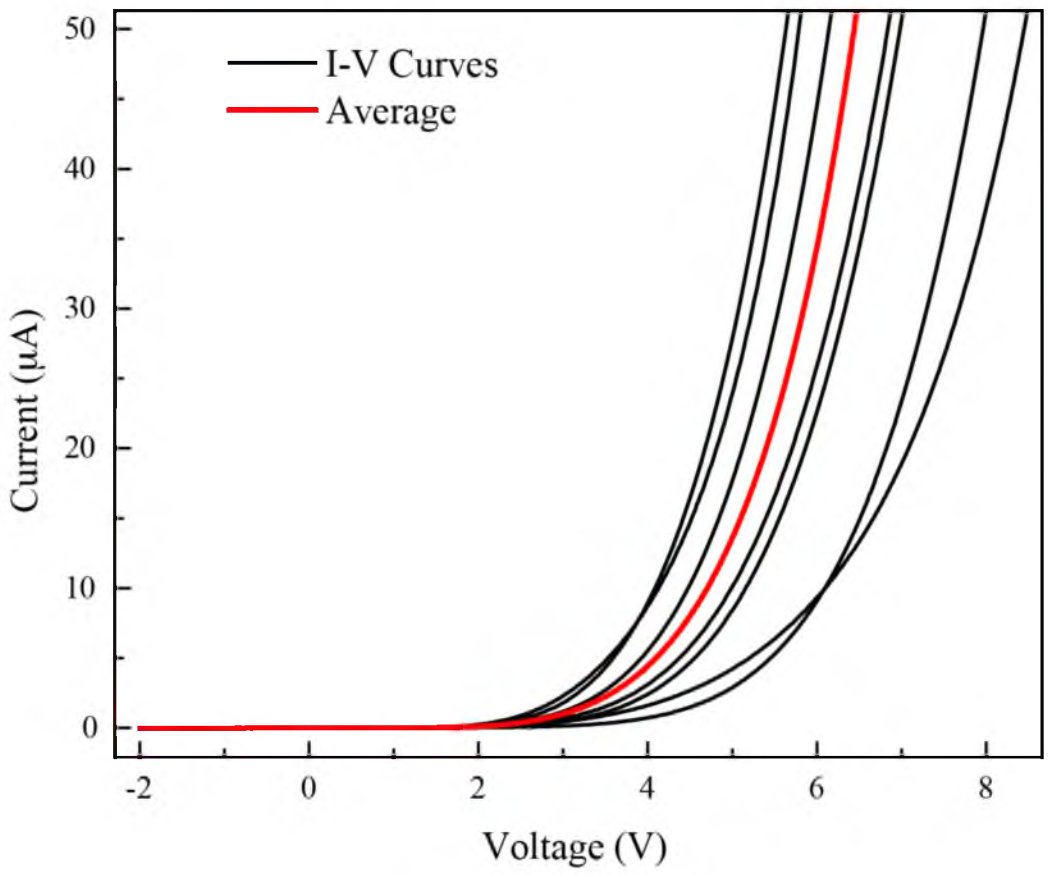


**Figure 3.3**. Room temperature current-voltage (I-V) characteristics of the OLED structures used for the experiments discussed in the following chapter. The OLEDs consisted of ITO/PEDOT:PSS/MEH-PPV/Ca/Al stack as described in detail in the text. The data shown for 7 OLEDs with 1 x 1mm$^2$ surface. The red curve represents the average I-V function obtained from the 7 data sets.

separately fabricated OLED structures used for the experiments discussed in the following chapter. The I-V data sets were recorded within less than 5 hours after deposition. They show significant spread between devices whose origin is likely due to layer inhomogeneities that can cause a spread of the band structure across the device ensemble. Most significant for all characterized devices is the exponential I-V behavior that is expected for the OLED under bipolar forward injection.

## 3.2 Experimental setup

To perform electrically detected magnetic resonance (EDMR) experiments, a static magnetic field $B_0$ and a perpendicularly polarized oscillating magnetic field $B_1$ are needed, along with a current source, a current amplifier, an analog/digital converter, and a computer for the current measurements. Various setups have been used for the experiments presented in this dissertation. In order to produce a homogeneous static field $B_0$ below 40mT, two electromagnetic coils connected to the computer-controlled constant current source were set up in a parallel Helmholtz configuration. For experiments above 40mT, a commercially acquired, larger ion-core, copper-coil Helmholtz magnet (made by Bruker Corp., Billerica) was used. In order to produce the oscillating field $B_1$, combinations of RF or microwave sources with respective amplifiers were connected to either a microwave resonating cavity (an X-band cylindrical dielectric resonator) or to copper coil resonators. In order to bias the device, a variable voltage source was used consisting of either a battery and a potentiometer or one or more Stanford Research Systems SRS SIM928 isolated voltage sources. The device current was measured by means of a Stanford Research Systems SRS570 current preamplifier.

### 3.2.1 EDMR experiments at low static magnetic field $B_0$

For EDMR experiments at low magnetic fields, a setup as sketched in Figure 3.4 was used. An *RF* signal was generated using an Agilent N5181A frequency generator and amplified by an ENI 5100L RF amplifier in order to generate the $B_1$ field. A Zurich Instruments ZF2 lock-in amplifier was used for the creation of a modulating magnetic field $B_{mod}$, the data acquisition, and the data processing before it was digitized and recorded by a computer. A Sony audio amplifier was used for the generation of the large

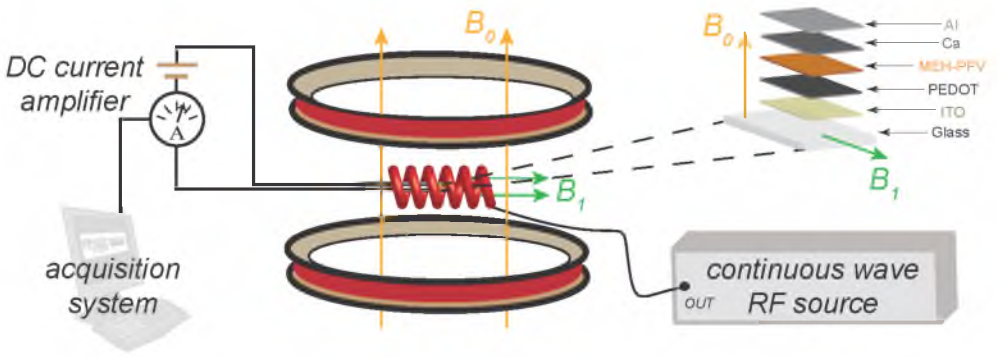


**Figure 3.4**. Sketch of the experimental setup for low-magnetic field EDMR experiments. An OLED stack consisting of MEH-PPV as well as layers for electron- and hole-injection is mounted on a narrow glass slide and contacted with thin ITO and metallic strips to minimize inductive coupling. It is driven by a battery as a constant voltage source, and the direct current is measured. A set of Helmholtz coils provides the static $B_0$ field, orthogonal to which the oscillating $B_1$ field is applied by an *RF* coil driven by an *RF* cw power source.

modulation current, which induced the modulation signal $B_{mod}$. A Keithley 2000 source meter measured the alternating current of the reference signal $B_{mod}$.

For EDMR experiments, the sample was mounted and electrically connected using a printed circuit board (PCB) located at the tip of a long plastic rod (the so-called sample rod) that could fit into the center of the *RF* coil, which itself was located at the center of the Helmholtz coil configuration that provided $B_0$. The sample plane was perpendicular to the direction of $B_0$ and parallel to $B_1$. The control of $B_0$ was accomplished by a Kepco ATE 100-10M constant current source. The continuous wave *RF* field was generated by an Agilent MXG N5181A generator whose output was connected to an ENI 5100L *RF* (50 dB, 100 W, 1.5-400 MHz) amplifier. The *RF* pulses used for $B_1$ calibration were triggered by a Pulseblaster DDS-I-300 pulse generator. Device bias was provided by a 9V battery connected to a potentiometer to minimize

electrical noise. The sample current was detected by an SRS570 amplifier (with a 10 Hz low-pass filter) linked to an AlazarTech ATS9462 analog/digital converter. MATLAB was used for data acquisition and processing.

### 3.2.2 Stripline EDMR setup for $B_0$-modulated frequency sweep experiments

Traditionally, most continuous wave magnetic resonance experiments reported in the literature have been performed by application of electromagnetic radiation with a constant and well defined frequency while magnetic resonance spectra are recorded by monitoring an observable (inductively detected radiation intensity [129], electric current [185], or optical emission [186]) as a function of an adiabatically swept magnetic field. The main advantage of this approach is that the facilities for the generation of the radiation field can be optimized (i.e., designed for a specific frequency where a resonating setup can be designed such that the power to amplitude conversation and/or the quality factor are maximized). This approach is the reason why magnetic resonance spectrometers are usually labeled with the wavelength domain for which they were built (e.g., X-, L-, Q-, or W-band). The opposite of this magnetic field sweep approach to magnetic resonance is the frequency domain magnetic resonance spectroscopy where the magnetic field is kept constant but the detected observables are monitored as functions of the applied frequency. The traditional way to implement this is by using pulsed, Fourier-transform magnetic resonance excitation where many frequencies are irradiated onto a sample at the same time by a radiation pulse or a pulse train [187].

Finally, a rarely employed but also feasible approach to conduct magnetic resonance spectroscopy is to adiabatically sweep the magnetic resonant excitation

frequency while the applied static magnetic field $B_0$ is kept constant. In this configuration, magnetic resonance spectroscopy is essentially conducted in the way most optical spectroscopy experiments on electric dipoles are performed. The splitting of spins is probed by an applied electromagnetic radiation that is swept into and out of the resonance condition. For magnetic resonance, the frequency sweep approach is rarely used since a broad frequency-range tuning of radiation generators from the RF into the microwave (MW) range is technologically difficult to implement, especially when a constant or at least only monotonically changing radiation intensity is needed. RF and MW generators have usually many strong inductive resonances either with themselves or due to coupling with their environment. The resulting intensity fluctuations as a function of the tuned frequency cause strong artifacts when this radiation is used for spectroscopy. These artifacts are then very hard to distinguish from the magnetic resonances that are to be investigated.

In Chapter 5, a frequency-domain EDMR experiment is discussed in the context of using a spin-dependent electric current for the detection of magnetic field gradients. The detection of a magnetic field distribution follows a recently reported magnetometry scheme [3], which allows for the detection a magnetic field by a radiation frequency sweep to which a spin-dependent charge carrier recombination current in an organic diode device is subjected. For the implementation of this frequency-domain EDMR experiment, a combination of a printed circuit board (PCB) and an organic diode structure was chosen, a setup displayed in the photos of Figure 3.5. Here, a Cu stripline for the generation of the oscillating magnetic field $B_1$ is directly mounted under an organic diode device.

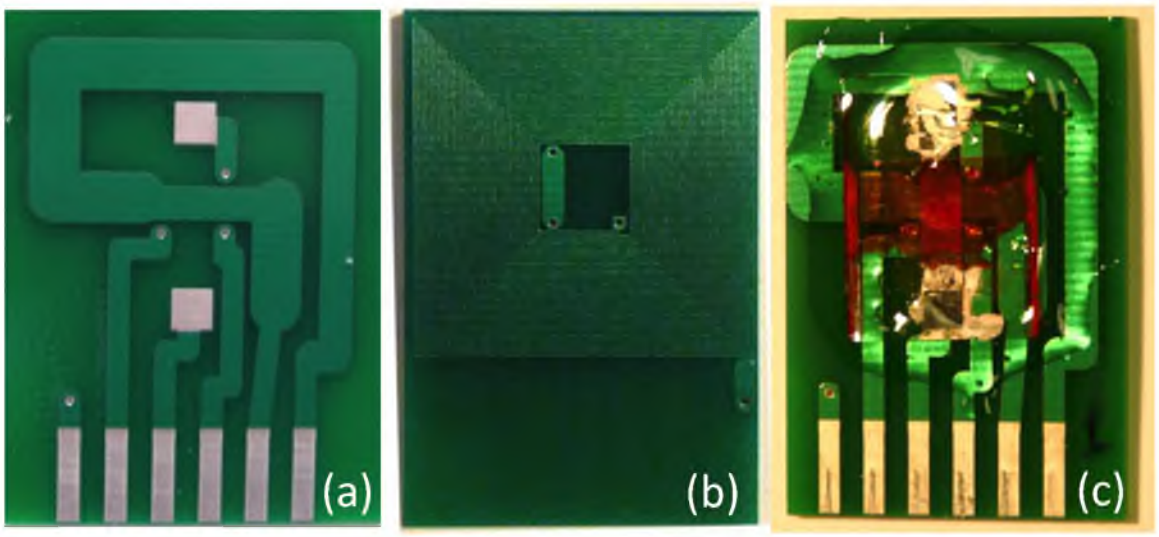


**Figure 3.5**. PCB design used for frequency sweep EDMR experiments. (a) Top of the PCB containing the two-diode contacts, the broadband low-Q stripline (between the contacts) as well as the vias that connect the modulation coil. The six contacts at the bottom allow for connections of $B_{mod}$, $B_1$, and diode current. (b) Bottom of the PCB, which contains the coil used to create the modulation field $B_{mod}$. (c) Picture of the finished setup containing a glass substrate with the organic device structure placed upside down on the PCB such that the contacts of the device shown in Figure 3.2(a) connect with the PCB contacts shown in (a).

On the opposite side of the PCB, there is a low-frequency magnetic field coil, which allows for the generation of an AC magnetic field that is superimposed onto the externally applied static magnetic field. The modulation coil is a crucial part of this setup because it allows for a magnetic field modulation combined with a lock-in detection of the spin-dependent device current. The discrimination of the inductively-induced artifact signals and the resonantly changed spin-dependent current becomes possible using this approach [3] because the small magnetic field changes generated by the modulation coil introduce changes to the magnetic resonance condition (and thus the spin-dependent currents); they have no influence on the inductively-induced current changes.

In order to calibrate the modulation coil, lock-in detected, frequency sweep

cwEDMR experiments were carried out on an MEH-PPV diodes in the presence of a random magnetic field caused by a NiFe paramagnet located in close proximity of the OLED (more details about this experiment in Chapter 5). For the experiment, an arbitrary (uncalibrated) modulation current was applied to the modulation coils, just large enough to make the EDMR signal detectable. The experiment was then repeated with the ac modulation current being superimposed by a constant offset current which would cause a magnetic offset field to be generated and thus, a shift of the observed magnetic resonance spectrum. Due to the lock-in detection scheme, both recorded magnetic resonance spectra are derivative spectra for which the crossing of the magnetic-resonantly induced current change from a positive to a negative signal (or vice versa, depending of the applied modulation phase) indicates the resonance line maximum. Thus, from the shift between the two spectra's zero-crossing frequencies, the magnitude of the magnetic field offset produced by the modulation coil can be determined. Figure 3.6 displays the two frequency sweep spectra with (red) and without (black) an applied current bias $I_{bias}$ = 140mA. The resulting frequency shift of the zero crossing was determined to be $\Delta f$ = 1.80MHz, corresponding to a modulation coil calibration factor of $\alpha$ = 1.28(3) mT/$A_{rms}$.

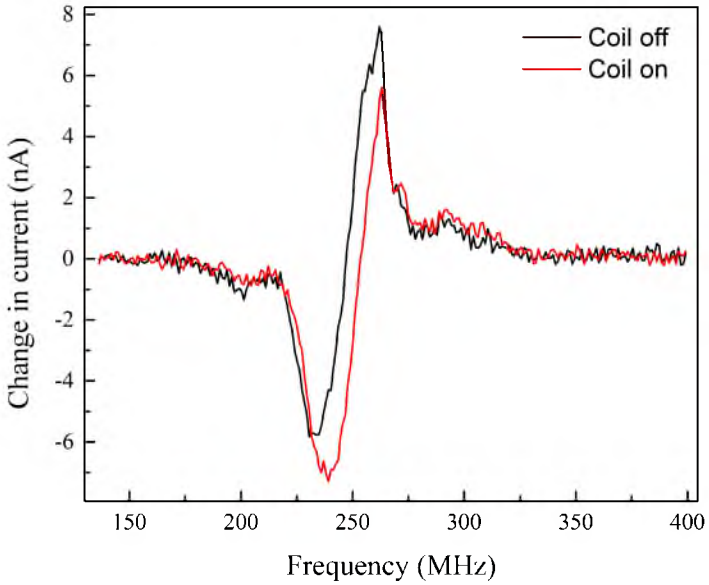


**Figure 3.6**. Magnetic field modulated room temperature frequency sweep cw EDMR experiments recorded on an MEH-PPV device using the PCB stripline setup for the calibration of the modulation coil. The device operated at a constant forward current of $I$ = 50μA, a modulation frequency of 2kHz, and a modulation ac current $I_{mod}$ = 140mA.

# CHAPTER 4

# OBSERVATION OF SPIN COOPERATIVITY UNDER STRONG MAGNETIC RESONANT AC DRIVING CONDITIONS USING ORGANIC MAGNETORESISTANCE[2]

## 4.1 Motivation

Macroscopic phase coherence of single-particle excitations is a hallmark of many exotic states of matter such as superconductivity, ferromagnetism, or Bose-Einstein condensation. Cooperativity, another manifestation of phase coherence, may be mediated by electromagnetic fields as described by the Dicke effect in collisional narrowing [184] and super-radiance [188], or arise directly through coherent interactions of the field with itself in weak localisation of photons [189] or random lasing [190]. Electron spins constitute perfect two-level systems. Under appropriate conditions – small local hyperfine fields $B_{hyp}$, large magnetic resonant driving fields $B_1$, and low static fields $B_0$ that define Zeeman splitting – the super-radiant spin-Dicke regime has been predicted [4]. However, this parameter range is extremely challenging to probe by conventional magnetic resonance spectroscopy as thermal magnetic polarisation is negligible. However, spin-dependent electrical currents in organic semiconductors [103] allow for

[2] The content of this chapter was taken from a manuscript coauthored by G. Joshi, M. Kavand, M. E. Limes, H. Malissa, P. L. Burn, J. M. Lupton, and C. Boehme that has been submitted for publication.

low-field magnetic resonance detection, removing the requirement of thermal spin polarisation. Room-temperature steady-state magnetoresistance of an organic light-emitting diode (OLED) reveals an *ac*-Zeeman effect for driving fields $B_1$ exceeding $B_{hyp}$. For ultrastrong coupling [191] of the spins to the driving field (i.e., when $B_1$ approaches $B_0$ and Rabi and Zeeman splitting become comparable), the electromagnetic field couples individually resonant spins together. A new regime of macroscopic spin cooperativity emerges where radiation-assisted charge trapping reverses the sign of magnetoresistance, offering a unique test bed for macroscopic room-temperature quantum coherence phenomena.

## 4.2 Introduction

At room temperature, charge carrier spins in the common OLED material poly[2-methoxy-5-(2'-ethylhexyloxy)-1,4-phenylenevinylene] (MEH-PPV) are characterised by long spin coherence and relaxation times, $T_2 \approx 350$ns and $T_1 \approx 40\mu$s, respectively [2]. These parameters ensure that even tiny magnetic fields, below nuclear hyperfine-field strengths, modify spin precession of localised carriers, thereby altering yields of electron-hole recombination and dissociation [2,132,192-194]. In an OLED, electrically-injected electrons and holes capture each other coulombically, forming carrier pairs [122]. Magnetoresistance [40,81,134] can arise from spatial variations in the local magnetic field experienced by these pairs due to interactions with the hydrogen nuclei.

A sketch of the experimental setup is depicted in Figure 3.4. Figure 4.1 contrasts $B_0$-sweeps of the steady-state OLED current at room temperature with and without an oscillating radio-frequency (*RF*) field of strength $B_1$. Two MEH-PPV derivatives [108], with hydrogenated (**1**) and deuterated (**2**) side groups, are compared.

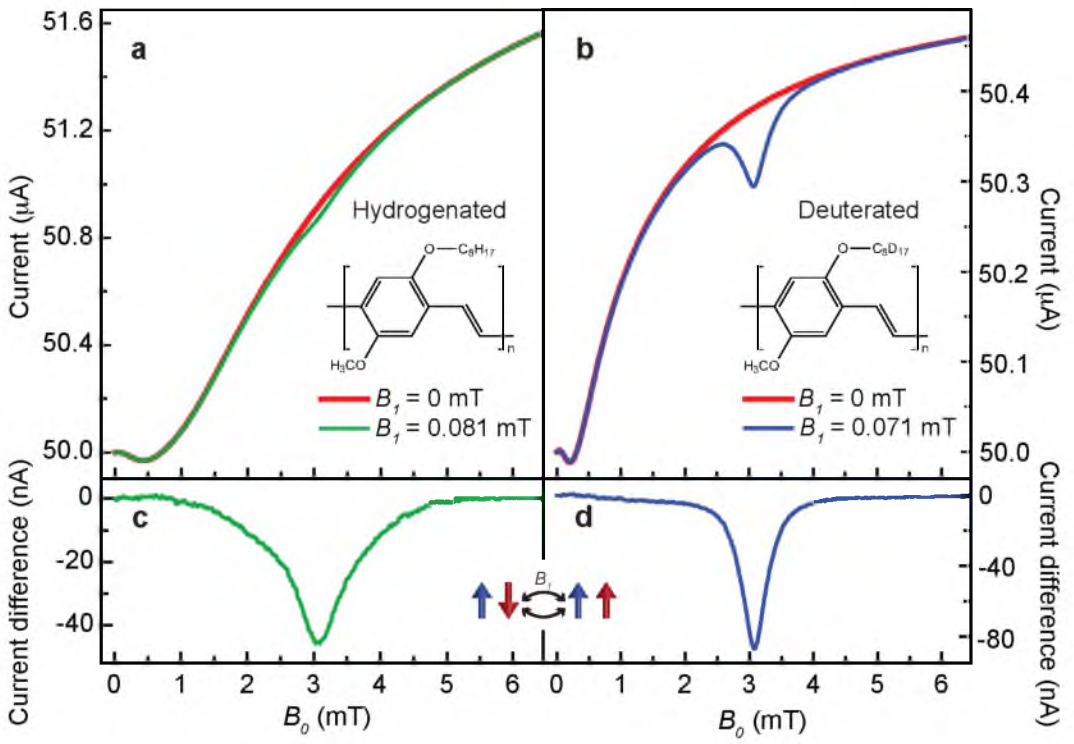


**Figure 4.1**. Magnetoresistance and magnetic resonance in the steady-state current of an OLED at room temperature. (a),(b) Magnetoresistance of MEH-PPV devices (5V bias) without (red) and with (blue, green) the *RF* field applied at 85MHz, for samples with hydrogenated and deuterated side chains. (c),(d) Difference between magnetocurrent curves with and without the *RF* field revealing an electrically-detected magnetic resonance spectrum in the steady-state device current. The cartoon illustrates the electron-hole pair resonance-induced transition between singlet and triplet manifolds.

For **1**, in panel (a), a small initial dip occurs close to the origin, followed by a large increase (negative magnetoresistance). The dip has been assigned to spin-dipolar interactions within carrier pairs, which partially shield the effective local hyperfine field $B_{hyp}$ [78,195]. As $B_0$ increases from 0-6mT, the current rises since fewer pairs recombine rapidly through the singlet channel as more experience Zeeman energies in excess of hyperfine splitting [105,132]. This effect is reversed by an 85MHz *RF* field, which exhibits a magnetic resonance around $B_0 \approx 3.1$mT, corresponding to an electron-hole *g*-factor of 2.002. On resonance, triplets are converted to singlets [103,196,197],

quenching the current. The difference between $B_0$-sweeps with and without *RF* radiation gives the characteristic magnetic-resonance line-shape in Figure 4.1(b), which corresponds to a hyperfine-broadened double-Gaussian function associated with electron and hole spin resonance [108]. The influence of $B_{hyp}$ on magnetoresistance can be tested by deuterating the 2-ethylhexyl side-chains of MEH-PPV, shown in Figure 4.1(b),(d). The magnetoresistance curve appears steeper, since local hyperfine fields are weaker and screened at smaller $B_0$ [105,108]. Under *RF* irradiation, the dip in **2** is more pronounced than in **1** because the hyperfine-broadened resonance narrows [105,108]. Parallels of this *RF* effect exist due to solution-based reaction-yield-detected magnetic resonance of pair processes [5,198,199], with the crucial difference being that the OLED current reveals *absolute* population changes, allowing for steady-state detection. This signal amplitude allows us to time-resolve excitation and detection to uncover spin-Rabi oscillations and spin beating due to correlated precession of electrons *and* holes. Prior experiments on OLEDs were carried out at much higher $B_0$ (≈340mT), using pulsed X-band microwaves and detected in current transients [1]. To demonstrate that steady-state magnetoresistance arises from *coherent* spin precession, the *RF* coil was pulsed and the current change as a function of pulse length was measured (see Figure 4.2). The Rabi frequency increases with the square root of the *RF* power, as expected [157], allowing for the direct calibration of the resonant driving field $B_1$ as described in the following.

### 4.3 Determination of the *RF* field strength

In order to calibrate the amplitude $B_1$ of the *RF* field, the frequency of magnetic resonance-induced spin-Rabi oscillation (i.e., precession of spin states about the *RF* field under magnetic resonance) was measured. As this experiment was conducted on the

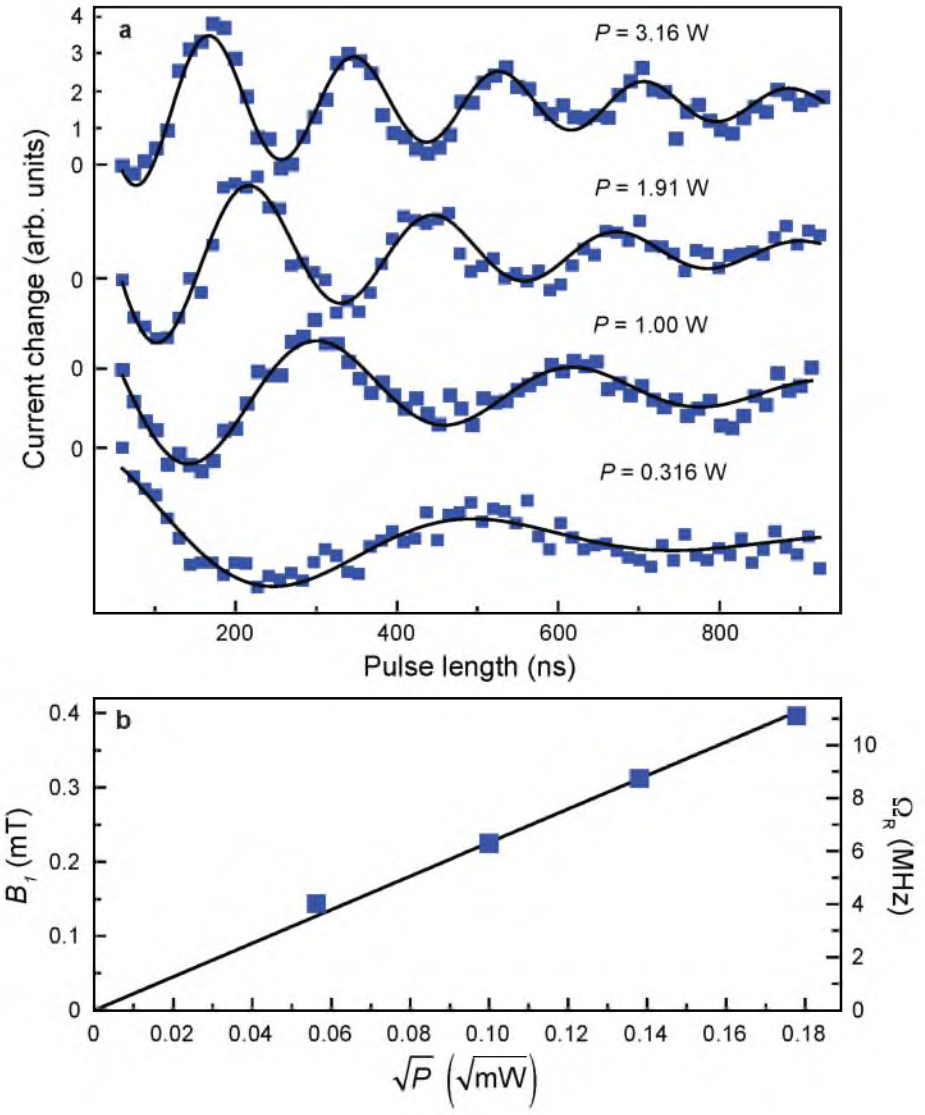


**Figure 4.2**. Rabi oscillations at varying powers plotted to determine $B_1$ field strength. (a) Plot of the device current change at 26.8μs after the device was irradiated with a short RF pulse as a function of the applied pulse length. The current reveals spin-Rabi oscillation. (b) Plot of the spin-Rabi oscillation frequency $\Omega_R$ as a function of the square root of the applied power P. The data reveal agreement with the expected linear dependence.

paramagnetic states that control the sample current, the spin-Rabi oscillation could be detected by sample current measurements. The frequency of the electrically detected spin-Rabi oscillation was then converted to the magnitude of the driving field by using the known gyromagnetic ratio [3] of the polymer's charge carrier states (for MEH-PPV, $\gamma$ = 28.03(4) GHz/T). This $B_1$ calibration followed the previously reported electrical detection of spin-Rabi oscillation at high $B_0$ fields [1]: the oscillating field was applied as a short pulse under magnetic resonant conditions ($B_0$ = 3.1mT, with an *RF* frequency of 85MHz), and the device current change in response to this pulse at a time $t_0$ = 26.8μs after the end of the pulse was determined as a function of the applied pulse length. The result of this series of measurements is displayed in Figure 4.2(a) for various applied *RF* powers. Each data set reveals an oscillatory dependence of the measured current change, which is due to the control of the current by coherent spin motion of the charge carrier spins. Each data set is displayed along with the result of its fit by an exponentially decaying sine function. The data were obtained for pulse lengths ranging from 60ns (the lower cutoff of the Pulseblaster pulse generator) to about 900μs in steps of 14ns (the minimal interval of the Pulseblaster). Figure 4.2(a) reveals the expected increase of the oscillation frequency.

Figure 4.2(b) displays a plot of the Rabi-frequencies $\Omega_R$ obtained from the fits of the data in Figure 4.2(a) as a function of the square root of the applied *RF* power. As expected for spin-Rabi oscillation for which $B_1 = 2\pi\,\Omega_R/\gamma$, the dependence of $\Omega_R$ on $\sqrt{P} \sim B_1$ shows excellent agreement with a linear function through the origin. From the linear fit of the power dependence displayed in Figure 4.2(b), one can extrapolate the relationship between the *RF* power and $B_1$ for any arbitrary *RF* power.

### 4.4 Magnetoresistance under different AC drive power regimes

Magnetoresistance and magnetic resonance-induced resistance are equivalent. Probing magnetic resonance directly with the magnetoresistive steady-state current allows for the exploration of interactions between carrier spins as well as their field-mediated equilibration. We distinguish three regimes of interaction between the relevant magnetic field strengths $B_0$, $B_{hyp}$, and $B_1$, as illustrated in Figure 4.3(a)-(c). For $B_1 << B_{hyp} < B_0$, the domain of conventional magnetic resonance [103], only one spin of the electron-hole pair is in resonance with the driving field. For the ensembles of weakly-coupled pairs, this means that singlet states flip to triplets and *vice versa*. While spin resonance controls spin-permutation symmetry, which determines conductivity through the underlying spin-dependent transitions [157], the net spin polarisation in the device remains zero. As the driving field is increased to $B_1 \sim B_{hyp}$, local magnetic disorder arising from hyperfine interactions is screened so that both electron and hole spins are in resonance, leading to spin beating [1]. Again, there is no connection between the individual carrier pairs, which have random spin orientations with respect to the driving field. However, in the ultrastrong-coupling regime [191], where the Rabi frequency approaches the Zeeman splitting (frequency), i.e., $B_1 \approx B_0$, the Dicke effect sets in [4]; the driving field defines the axis for the spin-Bloch sphere, voiding the rotating wave approximation [5]. In the Dicke regime, all particle spins act together, generating collective behaviour. As predicted by Roundy and Raikh [4], the spin-pair ensemble in this regime splits into two subensembles, a small superradiant set, which assumes collective pure-singlet character; and a dominant subradiant set consisting of triplet states. Under these conditions, it is the generation of the subradiant triplet ensemble that

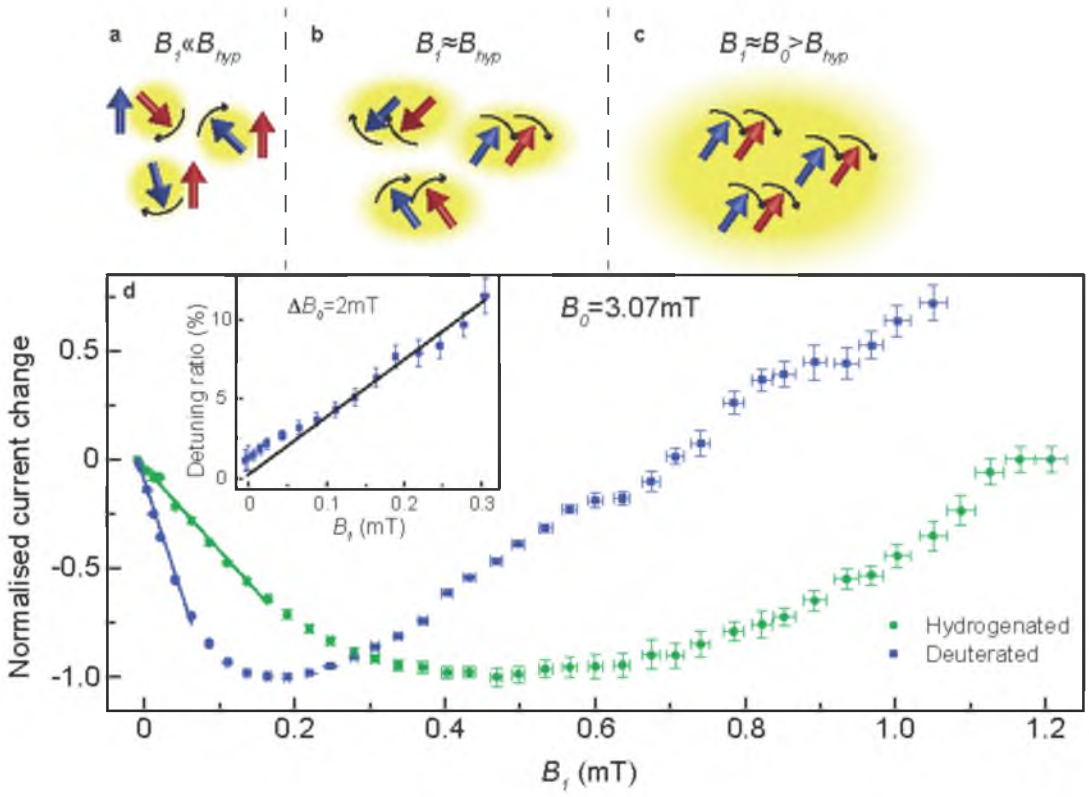


**Figure 4.3**. Emergence of spin cooperativity in OLEDs as a function of driving field $B_1$. (a) For low driving fields weaker than the local hyperfine fields, only the electron or the hole within a carrier pair is resonantly excited. (b) As $B_1$ increases to exceed $B_{hyp}$, both electron and hole within a pair become resonant, gradually cancelling out the effect that spin-dependent transitions have on conductivity. (c) For very large driving fields on the order of the static field $B_0$, the spins across the ensemble form a cooperative state, a manifestation of the Dicke effect. (d) Current change $\Delta I$ normalised to the magnitude of current change at saturation as a function of driving field $B_1$ exhibiting the three regimes described above, for hydrogenated and deuterated samples. Linear fits to regime a) are indicated, based on the theory described in Ref. [4]. The inset shows the effect of detuning $\Delta B_0$ = 2mT off-resonance, with the difference ratio in resonance strength ($\Delta I$) between on-resonance and off-resonance plotted against $B_1$. The linear dependence on $B_1$ predicted by theory is observed.

leads to radiation-induced Pauli-blocking of pair recombination into excitons, a phenomenon described as radiation-induced charge trapping [4]. The net result of collective driving-field-mediated sub- and superradiance effects, which are analogous to light-driven mesoscopic coherences [188], is a reversal of current change due to a strong *antiquenching* condition since the field-induced Pauli-blockade lowers the pair recombination rate. Roundy and Raikh [4] used the terms sub- and superradiance in this context for quenching and enhancement of spin-dependent radiative recombination rates.

### 4.5 Results

This theoretical description of OLED magnetoresistance under *ac*-drive in different $B_1$-regimes [4] allows for several predictions. First, the resonance magnitude (current change $\Delta I$) initially scales linearly with the amplitude $B_1$ of the driving field rather than quadratically, as would be expected for electromagnetically-induced absorption. A linear increase of magnetoresistance on resonance is shown in Figure 4.3(d) for hydrogenated and deuterated samples, where $\Delta I$ is normalised for direct comparison. The linear increase with *amplitude* rather than power ($\sim B_1^2$) arises since $\Delta I$ is controlled by spin-permutation symmetry [157]. The spectral overlap of the power-broadened radiation field with the resonance therefore translates directly to the number of pairs modulating transition probability, resulting in a proportionality in transition rate. Theory predicts the linear slopes to be antiproportional to hyperfine field strength [4], which is confirmed by experiment (see section 4.7). Following the linear rise of $\Delta I$ with $B_1$, saturation of magnetoresistance should occur, followed by a linear decrease [4]. The confirmation of this linear rise is found by dividing each $B_1$ field by their respective

hyperfine fields $B_{hyp}$. Another test of the theory comes from the effect of $B_0$-detuning on $\Delta I$. Off-resonance, $\Delta I$ should be zero, but as $B_1$ increases, the change of the resonance line-shape due to power broadening is predicted to lead to a quadratic rise in $\Delta I$ with $B_1$ for small $B_1$ below saturation [4]. We tested this prediction by considering detuned current change $\Delta I_d$ normalised to the on-resonance current change $\Delta I_r$. Since $\Delta I_r \sim B_1$ and $\Delta I_d \sim B_1^2$, the detuning ratio $\Delta I_d/\Delta I_r$ is proportional to $B_1$. This relation, which agrees with the linear $B_1$-dependence, is shown in the inset of Figure 4.3(d) for $\Delta B_0$=2mT detuning. The deviation close to the origin results from hyperfine broadening of the resonance, which compromises one of the conditions set by theory that the detuning $\Delta B_0$ be large ($\Delta B_0 >> B_{hyp}$) [4]. We conclude that the theory [4] withstands experimental scrutiny and note that the observations differ fundamentally from conventional spin-locking invoked to describe inversion of reaction-yield-detected *RF* resonances [5] since the resonance line-shape depends on $B_1$.

### 4.6 Testing the validity of the Roundy-Raikh predictions for small $B_1$

A rigorous theoretical description of the phenomena explored experimentally here was given recently by Roundy and Raikh [4]. This work described analytical expressions for spin-dependent transition rates controlled by the Pauli blockade of pairs of spins with s = 1/2 in the presence of a constant, low magnetic field $B_0$ and a perpendicular, oscillating field $B_1$ under steady-state conditions. The work by Roundy and Raikh therefore provides several counter-intuitive quantitative predictions that can be scrutinised experimentally. We do this by comparing hydrogenated and deuterated samples of (i) the slopes of the initial linear increase of the recombination rate (decrease

in current); (ii) the saturation maximum; (iii) the linear decrease of the slope in the spin-locking regime; (iv) the detuning; and (v) the onset of the Dicke regime.

The tests (ii), (iv), and (v) are discussed in the main text. With regard to (i), this is confirmed by the agreement of the ratio $m_1^D / m_1^H = 2.74(9)$ of the initial linear current decay slopes $m_1^H = -3.87(6)\mathrm{mT}^{-1}$ and $m_1^D = -10.6(3)\mathrm{mT}^{-1}$ for the hydrogenated and the deuterated samples, respectively, obtained from the fits in Figure 4.3(d). Further, the ratio is $w^H / w^D = 2.32(15)$ of the hyperfine broadened resonance line full widths at half maximum, with $w^H = 1.09(5)\,\mathrm{mT}$ for the hydrogenated and $w^D = 0.47(2)\,\mathrm{mT}$ for the deuterated sample. These values were obtained from the hyperfine-broadened magnetic resonance lines shown in Figure 4.1(c),(d).

With regard to (iii), the decrease of the rate (increase of the current) is evident in the intermediate region of the plot in Figure 4.3(d). Note that theory also predicts a proportionality of this decay with $B_1$, with a slope that is inversely proportional to the hyperfine field strength [4], yet overall smaller than the slope of the linear increase at small $B_1$. For the deuterated sample, the fit of the rate decrease yielded good agreement with a linear function and a slope of $m_2^D = 2.31(5) mT^{-1} < m_1^D$. For the hydrogenated samples, the fit of the rate decrease (the current increase) yielded a poor result, which can be attributed to the circumstance that the experimentally available $B_1$ range is insufficient to cover the drop in resonance amplitude beyond the rate inversion point (the onset of the Dicke regime) that is needed to define an adequate fit range. However, qualitatively, Figure 4.3(d) does confirm the theoretical prediction [4] that the slope of the decrease in mixing rate with increasing $B_1$ is smaller for the hydrogenated sample compared to the deuterated sample and, similarly, that it is much smaller than the slope of the initial linear

rise in mixing rate at small $B_1$.

### 4.7 Detection of spin-cooperativity

Given the confirmation of the predictions for *ac*-responses of OLED current at low to intermediate $B_1$ driving fields [4], we tested the theory for high $B_1 \approx B_0$. At a critical $B_1$, the resonances should vanish [4], beyond which the Dicke regime emerges, manifested by $\Delta I$ sign-reversal and a collapse of the resonance line-shape (collisional narrowing). Resonances of the two devices are plotted as a function of $B_1$ in Figure 4.4(a),(b). To obtain the data in these plots, the current measurement for each combination of $B_0$ and $B_1$ was repeated on the order of 20 times. Each run was recorded separately so as to obtain an accurate measurement of the fluctuations in the current at each field. By determining the current on resonance for each individual run, the standard deviation of the sample current through the estimator for an unbiased sample variance was found. The error of $B_1$ was determined from the error of the square-root of power to $B_1$ conversion factor that was obtained from the linear fit of the data in Figure 4.2(b).

When the data sets in Figure 4.4 are compared, it becomes clear that for (a), the dominant effect is power broadening, which decreases in strength as the fundamental and harmonic spin precession [1] cancel out their mutual impact on $\Delta I$ for large $B_1$. At $B_1$=1.1mT, the resonance vanishes. $B_1$ was limited by constraints on the *RF* amplifier and coil design. For (b), the critical field $B_1 > B_{hyp}$ is approximately halved and the resonance is narrowed, so that the underlying structure becomes visible. The spectrum in panel (b) shows the same power broadening as in (a), but exhibits bifurcation above $B_1 \approx 0.4\text{mT} > B_{hyp}$. This splitting is a consequence of the *ac*-Zeeman effect induced

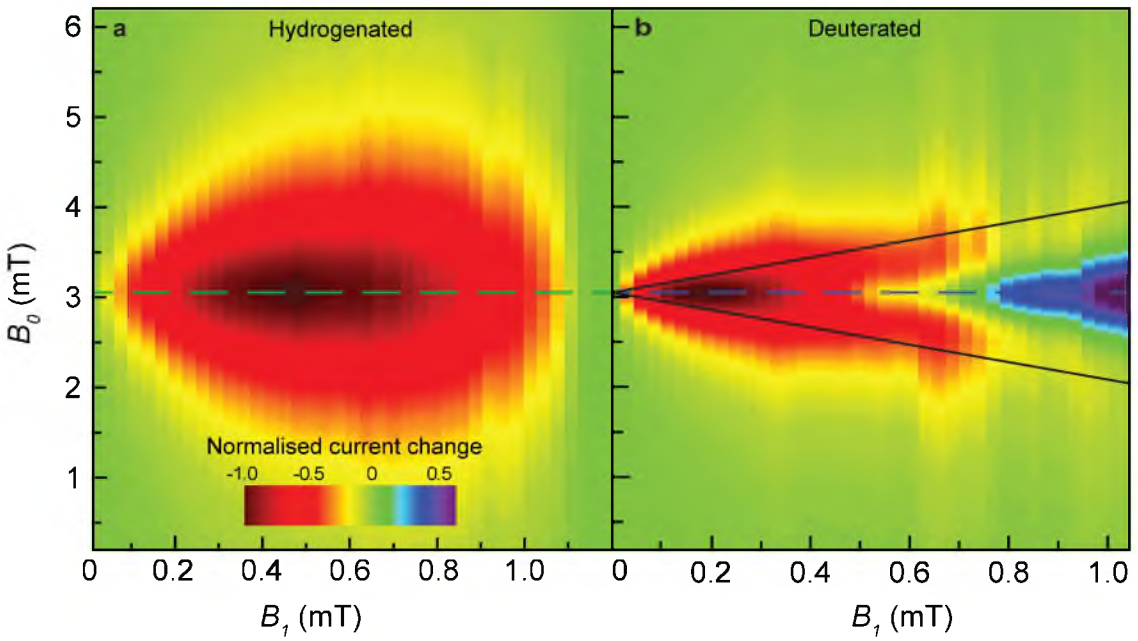


**Figure 4.4**. Plots of normalised OLED current change under *RF* irradiation as a function of $B_0$ and $B_1$ for hydrogenated and deuterated samples. Besides power broadening, the deuterated sample with smaller $B_{hyp}$ reveals a splitting of the resonance due to the *ac*-Zeeman effect, and an inversion of signal amplitude at the onset of the Dicke regime. The black lines indicate the magnetic field correction to $B_0$ arising from the $B_1$-induced Zeeman splitting.

on the spin-pair transition by the oscillating field. The expected splitting induced by $B_1$ on the scale of $B_0$ is shown as black lines. Since *ac*-Zeeman splitting constitutes a quantum-optical correction to the resonance energy, it is more appropriate to describe the coupling in terms of a spin polariton. The two branches of the resonance reveal nonlinear anticrossing behaviour around $B_1 \approx 0.6$mT, characteristic of the polaritonic nature [191] of coupling. At higher fields, the resonance suddenly inverts, coinciding with spectral narrowing. Above $B_1 \approx 0.7$mT, most electron-hole spin pairs precess in phase, leading to spin cooperativity, which inverses the effect of spin precession on spin-dependent transport. This macroscopic spin coherence, arising from the transfer of oscillator strength of a collection of two-level (spin) systems to one effective transition [184,188],

entangles the quantum-mechanical basis set responsible for spin-selection rules and spin-dependent conductivity [4,157]. Entanglement gives rise to a new resonance condition, the creation of collective triplet (subradiant) and singlet (superradiant) spin ensembles and the associated current increase due to radiation-induced trapping of recombining electron-hole pairs that quench the recombination rate.

### 4.8 AC drive induced off-magnetic resonance signals

The deuterated MEH-PPV device in the high AC driving field regime $B_1 \approx B_0$ shows, in response to the radiation, additional magnetoresistance changes that are not RF artifacts but are far off of magnetic resonance. First, for $B_1 > 8$mT, a signal appearing to be a higher harmonic of the excitation frequency is seen that is centred at double the resonant magnetic field of $B_0 \approx 6$mT, as displayed by the blue data set in Figure 4.5. To determine if this effect is caused by magnetic resonance (if it is due to spin-dependent processes) or a different artifact (e.g., magnetic induction), the experiment was repeated with the *RF* coil and sample being rotated within the static magnetic field such that the orientations of $B_1$ and $B_0$ would become parallel within an estimated error of approximately 3° (due to the experimental setup being rotated manually). The idea behind this experiment is to test whether the dependence of a magnetic resonance signal on the mutual orientation of $B_1$ and $B_0$ influences the observed signal. The result of this experiment is shown by the red data in Figure 4.5. When $B_1 \| B_0$, the observed signal disappears, indicating that it is caused by a weak higher harmonic of the excitation setup, which becomes dominant only at very high RF powers. The weak higher harmonic could be a result of small RF-amplifier nonlinearities. Note that while the higher harmonic

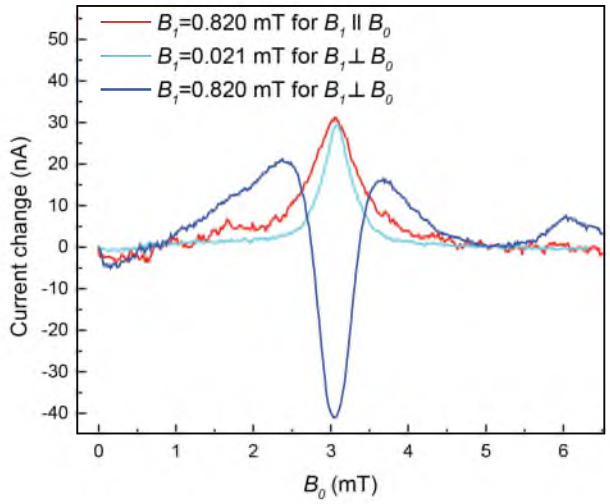


**Figure 4.5**. Plots of OLED current change under *RF* irradiation as a function of the applied static magnetic field $B_0$ for very large $B_1$=0.82mT with $B_0$ and $B_1$ perpendicular (dark blue) and parallel (red) as well as for weak $B_1$=0.21μT with $B_0$ and $B_1$ perpendicular (light blue).

signal disappears entirely when $B_1 \| B_0$, the main signal caused by the RF generators fundamental mode can still be observed. This is expected because of the estimated error of the $B_0$-turning angle as well as the strong power. If $B_1$ and $B_0$ are angled by only 3°, the residual projection of $B_1$ onto the plane that is normal to $B_0$ is approximately 21μT, enough to produce a significant on-magnetic resonance magnetoresistance change as can be seen by the light blue data set in Figure 4.5 recorded with $B_1$ and $B_0$ mutually perpendicular. Thus, due to the high power, the signal strength from an OMAR measurement shows little to no change in the orientation of the sample with respect to the $B_0$ field [200,201] magnitude. The signal is fully saturated, and changes to the relative orientation of the $B_0$ and $B_1$ fields have no effect anymore.

A second magnetic resonantly induced magnetoresistance change can be observed for very small values of $B_0$. Similar to the higher harmonic, the signal appears when $B_1$

and $B_0$ are mutually perpendicular, and it disappears when they become parallel. However, in contrast to the higher harmonic, this signal occurs for both large and small $B_1$. This signal can be explained by a superposition of the very small externally applied field $B_0$ and the local hyperfine fields of a small, randomly defined subensemble of charge carriers within intermediate pairs.

# CHAPTER 5

# ORGANIC SEMICONDUCTOR BASED MAGNETIC RESONANCE MAGNETOMETRY IN PRESENCE OF GRADIENT MAGNETIC FIELDS

Spin-dependent currents in organic semiconductor materials allow for the electrical detection of magnetic resonance at very low magnetic fields. This realization has opened up the possibility to extend the range of magnetic resonance magnetometry (MRM) to magnetic fields significantly below 100mT. This chapter focuses on how organic (O) MRM can be conducted in the presence of gradient magnetic fields. It is studied how the magnetic field gradients affect the accuracy and resolution of OMRM and whether the frequency sweep-based detection schemes of the OMRM can be utilized for the determination of magnetic field distributions throughout the gradient field applied to an OMRM device.

The content of this chapter was taken from a manuscript coauthored by C. Boehme that is to be submitted for publication.

## 5.1 Introduction

In contrast to magnetoresistance- [202], Hall effect-, or tunnel junction-based magnetometry [203], the utilization of magnetic resonance based magnetometers (MRMs) allows for high resolution (e.g., of up to 2fT/√Hz for single NV-center based magnetometers [204,205]) without the need for calibration or repeated recalibration of

the sensor even under changing temperature-, environmental- or device-conditions. This "built-in" robustness of MRMs is because the robustness of the gyromagnetic ratios of the electrons and nuclei, which are essentially constants of nature. Traditionally, MRMs have been based on the inductive detection of nuclear magnetic resonance, a technologically straight forward approach which has worked well for the measurement of high magnetic field magnitudes at low temperatures when the utilized probe spins are sufficiently polarized. However, for low-magnetic field (<100mT) and room temperature domains where spin-polarization is small for both electron as well as nuclear spin ensembles, this approach fails and nonpolarization dependent MRM schemes are needed. In recent years, a number of such low-field MRM concepts using spin-selection rules rather than spin-polarization have been reported [NV centers, silicon EDMR, organic EDMR]. Spin-selection rules on electronic transitions allow for significantly more sensitive spin-detection for two reasons: (i) Electronic transitions such as charge or radiative transitions are easier to detect [150] and (ii) spin-selection rules are oftentimes not polarization dependent [157]. An example for a spin-selection rule utilizable for MRMs is the Pauli blockade, where, in absence of strong spin-orbit coupling (as given by low-Z materials like carbon and silicon based solids), an electronic transition between two paramagnetic states with s=1/2 (e.g., two charge carriers) is governed by the permutation symmetry state of the spin-pair state and not polarization. Examples for devices that allow for spin selection rule-detected magnetic resonance magnetometry includes single NV center-based magnetometers, which have achieved unrivalled resolution but require nano-optics. Other examples for spin-selection rule-based MRMs concepts are electrically detected MRMs based on silicon and organic semiconductors.

The latter have proven to allow for integrated and scalable high-resolution sensors as well as operation over large temperature ranges [3]. In particular, the permutation symmetry-dependent currents in organic semiconductor thin-film devices have been shown to allow for the electrical detection of electron paramagnetic resonance at very low magnetic fields. This realization has opened up the possibility to use MRM also in the low to intermediate field range (<100mT).

The work presented in this chapter is focused on the question of how the recently reported organic semiconductor based magnetic resonance magnetometer (OMRM) using electrically detected magnetic resonance can be applied in the presence of inhomogeneous magnetic fields. Two questions are addressed, namely:

(i) How well can the applied magnetic field range and the applied magnetic field mean be determined and how is the measurement accuracy affected when a magnetic field gradient is present?

(ii) Can the existing OMRM concept be extended to the measurement of magnetic field distributions within an inhomogeneous magnetic field?

Experimentally, this study will focus on spatial magnetic field fluctuations across a 1mm x 1mm active area of an organic semiconductor thin-film device. Changes of a constantly biased forward current of an organic diode structure (equivalent to an organic light emitting diode, OLED) based on a glass/indium tin oxide/ Poly(3,4-ethylenedioxythiophene) polystyrene sulfonate/ Poly[2-methoxy-5-(2-ethylhexyloxy)-1,4-phenylenevinylene]/Ca/Al stack will be monitored as a function of an on-printed circuit board induced oscillating magnetic field. The idea behind this measurement approach is to monitor lock-in detected current changes $\Delta I(f)$ in the OLED as a function

of the oscillating magnetic field frequency *f*. Since these changes are governed by the magnetic resonance condition of recombining electron-hole polaron pairs with well-defined gyromagnetic ratios, the frequency dependence of the measured current change can reveal magnetic field distributions throughout the active device area.

The measurement scheme discussed in the following is illustrated in Figure 5.1. It is a device with six terminals, the anode and cathode of the OLED, the two leads of a radio-frequency (RF) excitation stripline, and two leads for the modulation coil on the back of the PCB. Since the measurement involves a frequency sweep (an extra dimension of the observable), this device scheme is able to reveal information about the magnetic field distribution function *D(B)* with a single sensor pixel, without the need for a large array of individual magnetic field sensors which would resolve the field spatially.

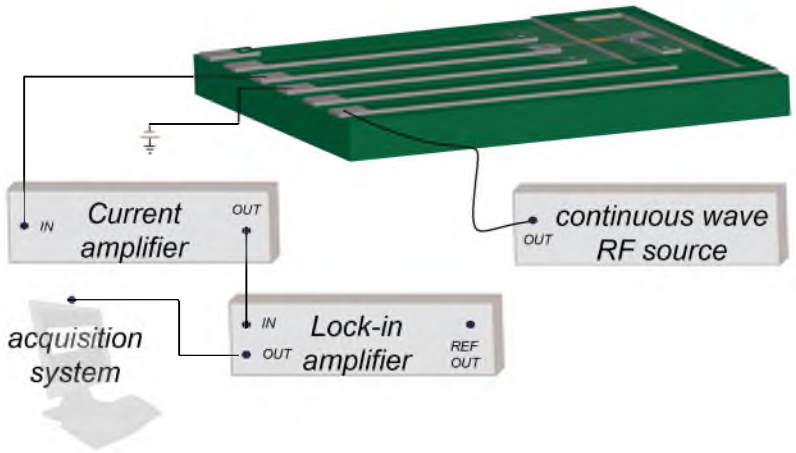


**Figure 5.1**. Sketch of the device and measurement concept for organic semiconductor based magnetic resonance magnetometry (OMRM). A small organic polymer thin-film diode (orange area) is placed on top of a copper stripline that is held in place by a printed circuit board. The magnetometry approach utilizes $B_0$ modulated frequency sweep EDMR spectroscopy, the illustrated devices is implemented by the setup discussed in 3.2.2. The stripline is connected to an RF frequency source. The diode is biased with a constant voltage in the forward direction, and the resulting constant current is fed into a lock-in amplifier that is modulated by the same source as the modulation coil (not shown here as they are on the bottom side of the PCB).

## 5.2 The influence of magnetic field distributions on OMRMs

Figure 5.1 illustrates the structure of an OMRM device as previously discussed for calibration free magnetometry [3]. A vertical-stacked organic diode with a square-shaped active area (the $\hat{x}-\hat{y}$-plane) is located above a copper strip line directed in the $\hat{y}$-direction that can be used to induce a linearly polarized magnetic AC field with amplitude $B_1$ in the $\hat{x}$-direction. The active material in the diode stack is MEH-PPV, in a ~100nm thick layer that is sandwiched between a thin (<10nm) Ca electron injection layer and a ~100nm thick Poly(3,4-ethylenedioxythiophene) polystyrene sulfonate (PEDOT:PSS) hole injection layer.

Under bipolar injection, long-lived intermediate pairs [KSM] of Coulombically coupled electrons and holes can form, which will either recombine or dissociate [Frankevich, pEDMR papers]. The recombination and dissociation probabilities of these weakly spin-spin coupled pairs strongly depend on their permutation symmetry [157]. Triplet pairs are generally significantly longer lived than singlet pairs. Thus, in the presence of a steady-state forward device current, triplet polaron pairs will accumulate and a magnetic resonant manipulation of either electron or hole spins within these pairs will lead to a quenching of the high triplet content. This quenching will lead to an enhancement of the singlet content and thus an overall increase of the recombination rate. This can be detected by the observation of the DC device current when magnetic resonance is established. With exact knowledge of the gyromagnetic ratio of charge carriers in MEH-PPV ($\gamma$ = 28.03(4) GHz/T), this effect can be used for robust (against temperature- and operating point-fluctuations as well device degradation) absolute OMRM [3].

As discussed in Ref. [3], when the OMRM device is exposed to a homogeneous magnetic field $B$, the magnitude can be determined in principle by a measurement of the change of the DC device current as a function of the frequency $f$ of an applied harmonic AC field. When the current change becomes maximal due to magnetic resonance (when $f/\gamma=B$ is at the center of the overlapping electron and hole spin-resonance lines that are broadened by random hyperfine fields [1]), the magnetic field $B$ can be established from the knowledge of $f$ For technical reasons (in order to suppress current changes due to inductive resonances [109]), the determination of the current change function $\Delta I(B,f)$ must be conducted in the presence of a low-frequency AC-modulation field whose orientation is perpendicular to the orientation of $B_1$. The modulation allows for filtering of any artifact currents induced by the strong fluctuations of the AC field throughout the scanned frequency range of $f$ that are technically difficult to avoid.

In the presence of homogenous fields $B$, $B_{\mathrm{mod}}$ and $B_1$, the lock-in detected current change in the actual MRM device is

$$\Delta I_{MRM}(B,f)=\frac{\partial \Delta I(B,f)}{\partial B}B_m=\frac{B_m\Delta I_0}{\sqrt{2\pi}}\left\{\frac{\left(\frac{f}{\gamma}-B\right)}{\delta B_e^{\,2}}e^{-\frac{\left(\frac{f}{\gamma}-B\right)^2}{2\delta B_e}}+\frac{\left(\frac{f}{\gamma}-B\right)}{\delta B_h^{\,2}}e^{-\frac{\left(\frac{f}{\gamma}-B\right)^2}{2\delta B_h}}\right\} \quad (5.1).$$

Equation 5.1 represents the superposition of two Gaussian derivative lines corresponding to the electron and hole resonances. Note that $\Delta I_0$ is an arbitrary current prefactor (which depends on the device size) while $\delta B_{\mathrm{e}}$ and $\delta B_{\mathrm{h}}$ are the widths of the hyperfine field distributions experienced by electron and hole polarons. Note that $\Delta I(B,f)$ will deviate from this analytically well-defined double Gaussian behavior if either $B_1$ or $B$ becomes inhomogeneous throughout the device area. The dependence on the homogeneity of $B$

becomes clear from Eq. 5.1. Utilization of this dependence is proposed for the measurement of a magnetic field distribution.

Note that the dependence of Eq. 5.1 on $B_1$ lies in the induced current changes by the driving field [i.e., $I_0 = I_0(B_1)$], which becomes significant in particular when small thin-film excitation strip lines are used for OMRM devices. This significance is in contrast to more bulky Helmholtz-RF coils, which produce a significantly more homogeneous field. A strong inhomogeneity of $B_1$ may prevent an explicit analytical representation of $\Delta I(B,f)$, yet even for this general case, the lock-in detected current change measured in the presence of an additional inhomogeneity of $B_0$ can be represented by

$$\Delta I_{MRM}(f) = \int_0^\infty dB D(B) \frac{\partial \Delta I(B,f)}{\partial B} B_m . \qquad (5.2)$$

The magnetic field distribution $D(B)$ here is determined by the relative fraction $D(B)dB$ of the active sample that senses a magnetic field with a magnitude in the interval $[B, B+dB]$. $D(B)$ is therefore strongly determined by the magnetic field magnitudes $B(x,y)$ that are sensed throughout the coordinates $(x,y)$ on the rectangular active sensor area. Note that the sensed magnitude $B(x,y) = \vec{B}(x,y,0) \circ \hat{x}$ is not the magnitude of the magnetic field $\vec{B}(x,y,0)$ at the position $(x,y)$ of the generally inhomogeneous magnetic field to which the device is exposed. It is the *projection* of this field into the plane that is perpendicular to the spin excitation field $B_1$ whose orientation we have assigned to the $\hat{x}$ – direction (see Figure 5.1). This realization becomes important for the determination of the direction of the gradient magnetic field vectors as it is conceivable to deduce the gradient from knowledge of magnetic field distributions within three mutually

perpendicular planes defined by the active areas of three mutually perpendicularly oriented OMRM devices.

For homogeneous static magnetic fields whose component perpendicular to $B_1$ has a magnitude $B_0$, the magnetic field distribution function $D(B) = \delta(B - B_0)$ and Eq. 5.2 will then revert to Eq. 5.1. In contrast, when inhomogeneous magnetic fields are present, *D(B)* can assume arbitrary forms that may or may not be analytically treatable. However, for any given inhomogeneous field and any given size of the active sensor area, there will always be a finite magnetic field range $\Delta B = B_{max}$-$B_{min}$. This range is defined by the maximal and minimal magnetic field magnitudes $B_{max}$ and $B_{min}$, respectively, which are experienced by the sensor. Outside of the interval [$B_{max}$, $B_{min}$], $D(B) = 0$, and thus within the interval, *D(B)* can always be expanded into a power series such that

$$D(B) = \begin{cases} \sum_{i=0}^{N} c_i \left( \frac{B - B_{min}}{\Delta B} \right)^i & for \quad B \in [B_{min}, B_{max}] \\ 0 & otherwise \end{cases} \tag{5.3}$$

for which only a finite number *N* of orders are physically relevant. The value of *N* depends on the magnitudes of the measured gradient, the direction of the area with regard to the magnetic field direction penetrating the area, the size of the active device area, the shape of the area, and the orientation of the shape with regard to the applied magnetic field direction. When the field distribution can be linearized across the active device area (e.g., the device is small and rectangular and the device boundaries are parallel to the field gradient), then $N=0$ and $D(B) = c_0 = 1/\Delta B$ for $B \in [B_{min}, B_{max}]$, since the normalization condition $\int_{B_{min}}^{B_{max}} D(B) dB = 1$ applies. Under these conditions, the integral in Eq. 5.2 dramatically simplifies and the current change assumes the form

$$\Delta I_{MRM}(f) = \frac{B_m}{\Delta B}\left\{\Delta I(B_{\max}, f) - \Delta I(B_{\min}, f)_1\right\}. \quad (5.4)$$

When the sensor area is chosen to be small in order to keep the number N of relevant orders of the magnetic field distribution small, $\Delta B$ and therefore the minimal detectable gradient will become small as well. The active device area size of an OMRM will always have to range between the smallest possible and the largest necessary dimensions, with both being determined by the magnitude of the detectable magnetic field gradients and the spatial resolutions of the measured field fluctuations. However, even when the gradient fields fluctuate weakly on the size scale of an OMRM sensor, the sensor shape and orientation with regard to the magnetic field still influence $D(B)$ and thus, in general, $D(B)$ has to be determined by a careful fit of $\Delta I_{MRM}(f)$ with a convolution of $\frac{\partial \Delta I(B,f)}{\partial B}$. Under the assumption of homogeneous modulation and excitation fields, $B_m$ and $B_1$, respectively, have the shape of a double Gaussian derivative function, as described by Eq. 5.1.

### 5.3 Frequency resolved EDMR of a 1mm x 1mm active area

An MEH-PPV based OLED, similar to the structure used for the experiments discussed in Chapter 4, was integrated in the frequency domain EDMR setup based on the PCB stripline design from Chapter 3. This allowed for the measurement of the change in current $\Delta I_{MRM}(f)$ in the presence of an inhomogeneous magnetic field produced by a coin-shaped NiFe permanent magnet with 3.2mm thickness and 12.7mm diameter. The magnet was placed on a delron spacer 8.5mm below the back side of the PCB. Using this spacer, it was possible to change the horizontal alignment of the permanent magnet in the plane parallel the PCB surface, as illustrated in Figure 5.2(a). The active area of the diode

device was 1mm x 1mm. With this arrangement, several lock-in detected frequency sweep cw-measurements were conducted for 9 different horizontal alignments of the permanent magnet. A horizontal array of 3 x 3 positions was used, as indicated in Figure 5.2(a), with a lateral spacing of 3(3)mm between the individual positions. The absolute alignment of the array was made such that at its center position (position 5 in Figure 5.2(a)), the center of the permanent magnet was brought closest to the center of the OLED. However, note that the array alignment relative to the OLED at the front side of the PCB was made through visual inspection, leaving an estimated error in the array position, relative to the diode, of approximately 1mm. The precision of the array positions with regard to each other is estimated to be 0.3mm. The measurements were conducted at room temperature, a steady state diode forward current of $I$=50μA, a modulation frequency of $f_{\mathrm{mod}}$=2kHz and a modulation current $I_{\mathrm{mod}}$ = 0.119A (rms), corresponding to a modulation field amplitude of $B_{\mathrm{mod}}$ = 0.153mT.

## 5.4 Experimental results

Figure 5.2(b) displays the results of the lock-in detected measurement of $\Delta I_{MRM}(f)$ at the center position (black line). The plot also displays a fit of the experimental data with the difference of two double Gaussian functions as given by Eq. 5.4 (red line). The fit was carried out using the peak positions on the frequency scale. The two standard deviations of the double Gaussian function were not fit parameters but werefixed values taken from the literature based on room temperature hyperfine field distributions within polaron pairs in MEH-PPV [1] that are found to be $dB_{\mathrm{e}}$ = 2.7mT and $dB_{\mathrm{h}}$ = 0.79mT. The fit function displays only very limited agreement with the experimental data; a realization that implies that for the given experiment, the assumption

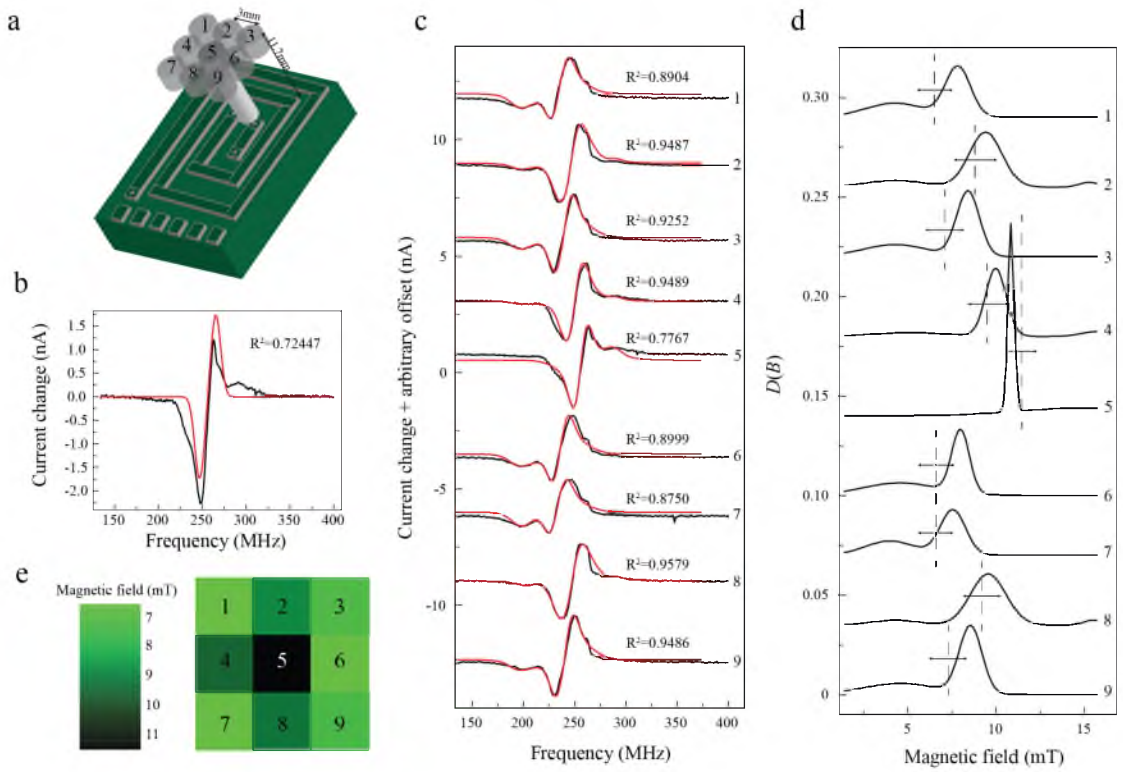


**Figure 5.2**. Magnetic field gradient distributions as measured with an array of permanent magnet positions. (a) Sketch of various positions of the permanent magnet relative to the PCB setup for which frequency sweep experiments were conducted. (b) The room temperature lock-in detected current change $\Delta I_{MRM}(f)$ as a function of the applied frequency $f$ recorded with the permanent magnet located in position 5 (black line) and the fit with Eq. 5.4 (red line). The two functions reveal poor agreement. (c) Similar experiments as in (b) for all positions 1-9 (black line) and fits (red line) with the assumption of a nonconstant magnetic field distribution that allow for complex distributions *D(B)* of the magnetic field throughout the active device area. As revealed by the coefficients of determination, the agreements of these fits are significantly better than in (b). (d) Plots of the magnetic field distribution *D(B)* throughout the active area as a function of the magnetic field as obtained from the fits in (c). The dashed lines indicate the mean magnetic field within the given distributions, the horizontal line indicates the estimated standard deviations for the given magnetic field distributions. (e) Color display of the magnetic field at the OMRM as a function of the magnet position within the array.

of a constant magnetic field distribution does not apply.

Measurements conducted at each of the 9 magnet positions are displayed in Figure 5.2(c). Here, the data were fit by a nonconstant magnetic field distribution function according to Eq. 5.2. The fit procedure was to generate a continuous trial function for $\widetilde{D}(B)$ and generate the corresponding trial function $\Delta\widetilde{I}_{MRM}(f)$ following Eq. 5.2. The trial function was generated using $\Delta I(f,B)$, the double Gaussian function described by Eq. 5.1 under consideration of the literature parameters for the polaron hyperfine fields $\delta B_e$ and $\delta B_h$ mentioned above. Once $\Delta\widetilde{I}_{MRM}(f)$ was calculated, a coefficient of determination $R^2$ was obtained by comparison with the experimental data and by iteration (repeated new generation) of $\widetilde{D}(B)$. Through this process, a gradual increase and eventual saturation of $R^2$ was achieved. For the generation of the trial function $\widetilde{D}(B)$, a series of Gaussian distributions was used. Following this procedure, for the experimental data for all 9 magnet positions, the fit functions displayed in Figure 5.2(c) [red lines] were generated. They show a consistently better agreement with the experimental data compared to the fit in Figure 5.2(b). However, as seen from the coefficients of determination displayed along with the fit results, there is still a considerable difference between the fit functions and the experimental results. Nevertheless, the iteration process for $\widetilde{D}(B)$ eventually converged for all data sets and yielded best-fit magnetic field distribution functions $D(B)$ for each magnet position. These functions $D(B)$, displayed in Figure 5.2(d), were used to generate the fit functions $\Delta I_{MRM}(f)$ displayed in Figure 5.2(c).

## 5.5 Discussion

The functions $D(B)$ for the different magnet positions are plotted in Figure 5.2(d) along with the mean values of the magnetic field distributions (vertical dashed lines) and the standard deviations obtained from these distributions (horizontal lines). As seen from Figure 5.2(d), all distributions include a pronounced maximum in the range of approximately 7 to 11mT and broadly distributed lower field values with small magnitude. This means these field strengths exist only within small fractions of the sensor area. Most of the mean magnetic field values are close to the respective maxima, yet depending on the extent to which broadly distributed features exist in $D(B)$, they also can deviate from the maxima significantly.

Figure 5.2(e) displays a color-coded 3 x 3 array that corresponds to the magnet positions. The colors represent the mean values obtained from the data in Figure 5.2(d). As expected, at the center of the matrix (position 5), the permanent magnet produced the largest magnetic field magnitudes at the sensor position. The diagonal positions (positions 1, 3, 7, and 9) lead to the lowest mean fields that were measured, and at the same time, they also lead to very similar $\Delta I_{MRM}(f)$ due to symmetry reasons [see panel (c)]. For the positions directly adjacent to the center [positions 2, 4, 6, and 8], intermediate mean field values are observed, as expected, with the exception of position 6 whose measurement is not symmetric with positions 2, 4, and 8.

The coefficients of determination between the experimental data and the fit functions $\Delta I_{MRM}(f)$ are significantly lower than what would be expected from the signal noise of the experimental data >98%. This is even though the fits are based on random distribution functions $D(B)$ that convolute the double Gaussian derivative functions

$\Delta I(f,B)$ expected for current changes in the presence of a homogeneous magnetic field $B$. It is concluded from this observation that the assumed double Gaussian derivative behavior is not an accurate description of the OMRM frequency response even in the presence of a fully homogeneous magnetic field.

### 5.5.1 $\Delta I_{MRM}(f)$ in presence of homogeneous magnetic field

The conclusion that a double Gaussian derivative is not an accurate description of the $\Delta I_{MRM}(f)$ in the presence of a homogeneous magnetic field can been tested. To test this, the OMRM setup [OLED and PCB as displayed in Figure 3.4(c)] was placed in an EPR magnet (Bruker E073 ion core copper coil magnet) with relative inhomogeneity below $10^{-5}$/mm over an area >25cm$^2$. Under this condition, the magnetic field distribution is not expected to influence $\Delta I_{MRM}(f)$; it can be considered a delta function $D(B)=\delta(B-B_0)$ with $B_0$ being the field generated by the EPR magnet.

Figure 5.3 displays the $\Delta I_{MRM}(f)$ measured in the presence of a homogeneous magnetic field of $B_0$=9.5mT (black data points) as well as a double Gaussian derivative fit. As expected, there are significant discrepancies between the experimental data and the fit function.

It is known (e.g., from Figures 1.2, 1.4, and 4.1) that the EDMR signal of polaron pairs in MEH-PPV have nearly ideal double Gaussian characteristics (within the accuracy of the measurement given in this dissertation or the literature [122]). Because of this, it is concluded that the deviation from the double Gaussian behavior in the presence of a homogeneous static magnetic field $B$ is inherent to the chosen measurement approach, the magnetic field modulated lock-in detected frequency sweep spectroscopy. There are three

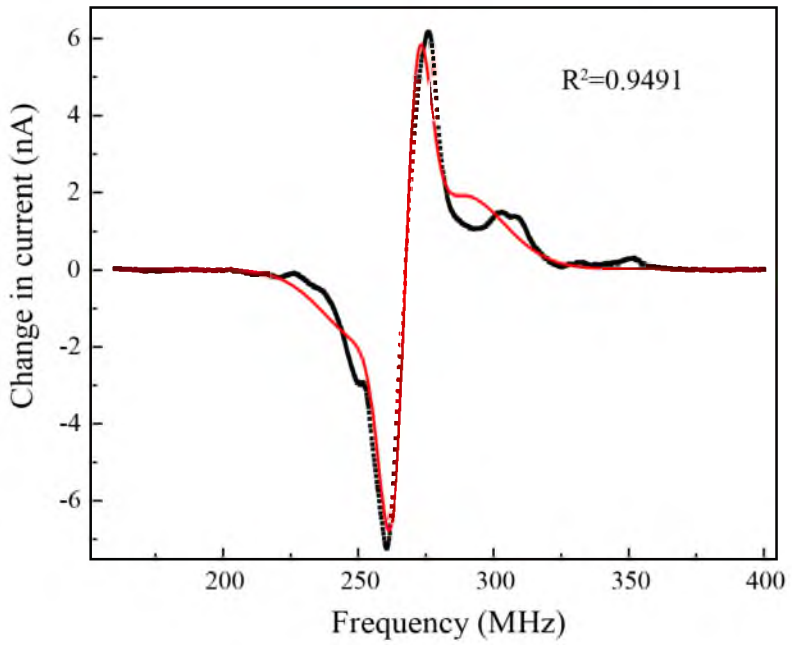


**Figure 5.3**. Lock-in detected frequency sweep cw EDMR measurement in the presence of a homogeneous static magnetic field of $B$=9.5mT (black data points) with a fit of the experimental data (red) using the expected double Gaussian derivation function (see Eq. 5.1). The error of the current change measurements is small (negligible to the magnitude of the displayed experimental values). The measurements were conducted at room temperature with an MEH-PPV diode device, a steady state forward current of $I$=50μA in the diode, a modulation frequency of $f_{mod}$=2kHz, and a modulation amplitude of $B_{mod}$ = 0.193A (rms), corresponding to a modulation amplitude of 0.248mT.

conceivable causes discussed in the following: residual inhomogeneities of $B_{mod}$ or $B_1$ or inductive coupling of inductive resonances of the RF stripline to the OLED devices. For either one of these three hypotheses, the reduced ability to resolve the probed magnetic field distribution as revealed by the reduced coefficients of determination shown in Figure 5.2(c) would be a direct result of the design parameters of the used OMRM device and not a principle limitation of the measurement approach. Nevertheless, these observed distortions not only reduce the accuracy of measurements of $D(B)$, they also pose limitations to the absolute accuracy of the OMRM device. As seen from Figure 5.3, the

reduced agreement of the fit of Eq. 5.1 with the experimental data raises the question on whether the value for $B$, which is revealed by the fit, is correct.

### 5.5.2 Influence of $B_{\mathrm{mod}}$ inhomogeneities on OMRM

When the magnetic modulation field $B_{\mathrm{mod}}$ is distributed, Eq. 5.1 must be changed to an integral

$$\Delta I_{MRM}(B,f) = \int_{B_m^{\min}}^{B_m^{\max}} dB_m D_m(B_m) \frac{B_m \Delta I_0}{\sqrt{2\pi}} \left\{ \frac{\left(\frac{f}{\gamma} - B\right)}{\delta B_e^2} e^{-\frac{\left(\frac{f}{\gamma}-B\right)^2}{2\delta B_e}} + \frac{\left(\frac{f}{\gamma} - B\right)}{\delta B_h^2} e^{-\frac{\left(\frac{f}{\gamma}-B\right)^2}{2\delta B_h}} \right\} \qquad (5.5)$$

representing the convolution of the distribution $D_m(B_m)$ of the modulation field components perpendicular to the orientation of the RF field $B_1$ and the double-Gaussian derivative function given by Eq. 5.1. This procedure is similar to the integration of the static magnetic field distribution given by Eq. 5.2, however, there is one crucial difference: when the double-Gaussian derivative function does not explicitly depend on $B_{\mathrm{m}}$, the integral $W_m = \int_{B_m^{\min}}^{B_m^{\max}} dB_m D_m(B_m) B_m$ can be reduced to a simple factor in the expression for $\Delta I_{MRM}(B,f)$. It is noted that Eq. 5.1 and thus Eq. 5.5 apply only for the assumption that the modulation amplitude is smaller than the line width ($B_m < \delta B_e, \delta B_h$) so that over-modulation does not take place. Thus, as long as over-modulation is not present, the inhomogeneities of $B_{\mathrm{m}}$ will distort neither the current change $\Delta I_{MRM}(B,f)$ for a homogeneous magnetic field $B$ nor the convoluted current change $\Delta I_{MRM}(f)$ for a magnetic field distribution.

### 5.5.3 Influence of $B_1$ inhomogeneities on OMRM

As for cw EPR spectroscopy, in stark contrast to pulsed EPR spectroscopy, the presence of inhomogeneities of $B_1$ poses little detriment for the spectroscopy of cw EDMR spectra. Thus, the ability to reveal absolute magnetic fields and magnetic field distributions is not affected by the homogeneity of the stripline RF fields. The argument for this is analogue to the argument for the insensitivity to inhomogeneities of the modulation field: Any influence of $B_1$ on $\Delta I_{MRM}(B, f)$ will enter through the prefactor $\Delta I_0 = \Delta I_0(B_1)$ in Eq. 5.1. Thus, a convolution of $\Delta I_{MRM}(B, f)$ across a distribution of $B_1$ will equal a superposition of identical line-shapes. Moreover, for strong $B_1$ fields well within the saturation regime of the excited polaron spins, there will not even be a dependence of $\Delta I_0$ on $B_1$. In contrast to cw EPR signals, EDMR signals remain constant once their saturation regime is established.

### 5.5.4 Influence of inductive resonances on the OLED current

For any conceivable design parameter set of the $B_1$ stripline, there will always be frequencies around which inductive resonances occur and for which the current within the stripline is either strongly enhanced or strongly quenched. For the application of these striplines for the generation of RF frequencies within a broad frequency spectrum, strong intensity fluctuations are therefore unavoidable and consequently, the coupling of these resonances to the measured OLED sample current is unavoidable as well. Since inductive resonances reflected by the OLED current change $\Delta I_{MRM}(f)$ are distinguishable from magnetic resonances only through their magnetic field dependence, the lock-in detection scheme based on magnetic modulation is used here in order to filter inductively-induced resonances from the OLED currents. While this filter scheme works excellently at

frequencies that are well outside of magnetic resonances, the overlap of magnetic and inductive resonances on the frequency spectrum can cause second order effects related to the inductive resonances. For example, the strong enhancement of $B_1$ within an inductive resonance line can cause the current change induced by a magnetic resonance to increase. Thus, if part of a magnetic resonance line overlaps with an inductive resonance line, then the magnetic resonantly induced current changes within the overlapping frequency range will be significantly stronger compared to the magnetic resonantly induced current changes outside the overlap region. In essence, whenever the lock-in detected signal is nonvanishing, the presence of an inductive artifact current can distort the measurement value. This realization has two important implications:

(i) Current-detected magnetic resonance line-shapes can be strongly distorted and this is consistent with what is seen for the data presented in Figure 5.3. It also explains the finite fit accuracy for arbitrary magnetic field distributions as seen in Figure 5.2.

(ii) While measured magnetic field distributions are distorted, absolute magnetic field measurements of homogeneous magnetic fields are not. Since the influence of the inductive currents vanishes in the absence of a lock-in detected current change, the crossing of the zero-level by the lock-in signal occurs for a distorted resonance line exactly at the same frequency as for a resonance line that is not distorted by inductive artifacts. Hence, for the data set in Figure 5.3, where the zero crossing occurred at f = 267.4MHz, a homogeneous magnetic field of $B_0$ = 9.54mT is measured. This is in agreement with reference measurements using the built-in Hall probes. Thus, in spite of a distorted double-Gaussian derivate

resonance line that is seen in Figure 5.3, an accurate magnetic field measurement is possible.

### 5.6 Sensitive detection of small magnetic field changes by environmental fields

The presence of inhomogeneous magnetic fields does not influence the ability of OMRM to measure small magnetic field changes. This is illustrated when the PCB setup described above is moved within the environmental magnetic fields consisting of the natural, geomagnetic field as well as local fields, (e.g., large, unshielded superconducting magnets within laboratory building, etc.). A permanent magnet is installed at a fixed position with regard to the PCB. Locally, within the size of the sensor device, environmental magnetic fields are entirely homogeneous. However, due to the presence of the magnet close to the PCB, an inhomogeneous magnetic field is applied to the sensor pixel and a distribution of fields is present. The PCB is then moved along with the permanent magnet that is placed at a fixed position relative to the PCB. (Illustrated in Figure 5.4(a) at a location corresponding to approximately positions 4 or 5 in Figure 5.2(a).) The homogeneous magnetic field is then changed relative to the reference frame of the PCB. However, the inhomogeneous field does not change in the course of this movement, and thus it is expected that the observed current change as a function of frequency, $\Delta I_{MRM}(f)$, will simply be shifted by an amount that corresponds to the magnitude change of the natural magnetic field component that is perpendicular to $B_1$.

Figure 5.4(b) displays a photo of the PCB setup (including connecting cables, the OLED as well as the attached permanent magnet) as it is held by a goniometer whose orientation can be adjusted into any spatial direction. With this setup, repeated measurements of

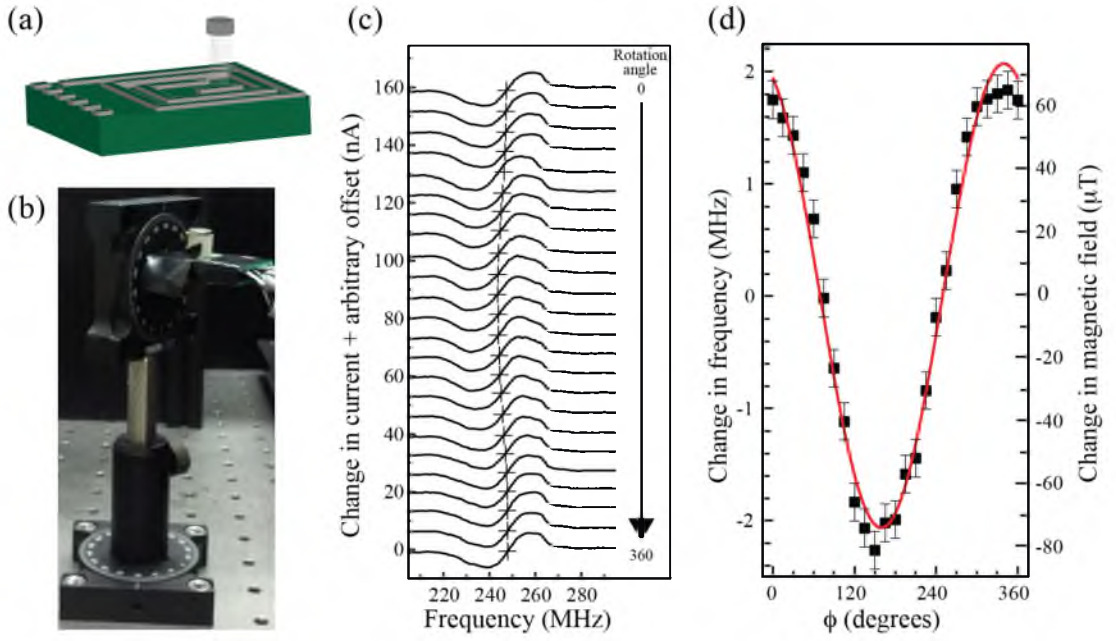


**Figure 5.4**. Measuring of the local magnetic field by changing the orientation of the magnetometer. (a) A permanent magnet is attached on the back side of the PCB in order to generate a static offset magnetic field. (b) The PCB/OLED/Permanent Magnet setup is installed on a goniometer, which allows for the accurate rotation of the PCB with regard to the laboratory. (c) Measurements of magnetic resonance induced current changes as a function of frequency and the orientation angle of the PCB with regard to the surface of the Earth. The measurements were conducted at room temperature, a steady state forward current of $I$=100μA in the diode, a modulation frequency of $f_{mod}$=2kHz, and a modulation amplitude of $B_{mod}$ = 0.119A (rms), corresponding to a modulation amplitude of 0.153mT. The data reveal a slight shift of the zero-crossing frequency of the derivative function as a function of the angle. The data also show a slight shift of the line-shape. (d) Plot of the zero-crossing frequency as a function of the PCB orientation angle (black data points). The plot includes a fit with a sine function expected for the net magnetic field. The fit consists of the constant offset field generated by the permanent magnet (and which is constant with regard to the PCB) and the small offset by natural magnetic fields which rotate with regard to the reference frame of the PCB.

$\Delta I_{MRM}(f)$ are performed for various angles $\theta$ around the axes perpendicular to the horizontal (the surface of Earth) and angles $\phi$ between the PCB surface and the horizontal. Figure 5.4(c) displays the results for 24 measurements corresponding to step increases of $\phi$ between $\phi = 0°$ and $\phi = 360°$ with a step of 15° increase in between. This set of measurements was recorded for an angle $\theta$ at which the most pronounced change within the recorded set of spectra was observed.

The measurements presented in Figure 5.4(c) reveal two observations: (i) The relative PCB orientation with regard to the environmental field causes a significant shift of the frequency spectrum. (ii) While a sole shift of the function $\Delta I_{MRM}(f)$ is expected, not only a shift but also a change of the line-shape is observed (e.g., compare data sets for 180° and 360°). It is concluded that this change of the line-shape is caused by a combination of the shift of the resonance lines with the changing direction of the external geomagnetic field and the magnetic field independence of the inductive artifacts.

From the data in Figure 5.4(c), the zero crossing frequencies of $\Delta I_{MRM}(f)$ were determined for values of $\phi$. The results of this analysis are plotted in Figure 5.4(d) which displays the measured zero crossing frequencies and their corresponding magnetic fields as a function of the angle $\phi$ (black data points). The experimental data set was fit by a sinusoidal function which is also plotted (red line) and which shows a good agreement within the experimental uncertainty range. As expected, the rotation of the geomagnetic field $B$ relative to $B_1$ causes a harmonic oscillation of the projection of $B$ onto the plane perpendicular to $B_1$. In spite of the presence of a strongly inhomogeneous magnetic field, OMRM is capable of recognizing changes of the probed natural environmental magnetic field. The sinusoidal fit has revealed extrema of the sinusoidal function for $\phi$=150(15)°

and $\phi$=330(15)°. These are the PCB orientations at which the geomagnetic field orientation is perpendicular to the surface of the PCB. Furthermore, the difference between the two detected magnetic field extrema, corresponding to twice the magnitude of the environmental magnetic field is 150(6)μT. The observed natural environmental magnetic field is 75(6)μT, a value that is larger than the geomagnetic field magnitude of 54 μT of Salt Lake City, UT where the experiments took place [206]. The discrepancy of about 21 μT is accounted for by local environmental magnetic fields within the physics laboratory building, which have been confirmed by Hall probe measurements.

# CHAPTER 6

# SUMMARY AND OUTLOOK

The study of spin-dependent recombination-controlled magnetoresistance effects of polymer based OLEDs in the presence of weak static magnetic fields and high-power ac magnetic fields presented in this thesis has experimentally confirmed a variety of phenomena that are of importance for both the fundamental understanding of electronic and spin processes in organic semiconductors and also for the exploration of potential spintronics applications based on this materials group.

The most fundamental results of this work are the first experimental confirmation that the spin-cooperativity and the spin Dicke regime of charge carrier spin states in OLEDs can be observed through magnetoresistance measurements. The implications of this result for the understanding of magnetoresistance are profound: Spin cooperativity, as revealed in Chapter 4, should emerge spontaneously in a device, without an external oscillatory field. This cooperativity should emerge given sufficiently small $B_{hyp}$ and large spatiotemporal fluctuations in local magnetic field strength (an effective $B_1$), such as due to spatial variations in dipolar and exchange spin-spin couplings experienced by a migrating charge. The spin Dicke effect may therefore contribute to the order-of-magnitude molecular magnetoresistance reported in constricted nanoscale transport channels [46] where carriers should experience extreme local-field fluctuations. The ability to form collective states of radical-pair spins – rather than individual pair states –

may find application in coherent control of chemical reactions, but also offers an alternative room-temperature route to permutation-symmetry-based concepts for electrically-addressable qubit operations [207] and resonance-based magnetometry [3]. Finally, the electromagnetically-induced transition to a collective excitation within operating OLEDs raises interesting questions regarding spin-bath entropy and temperature and may allow solid-state cooling by adiabatic demagnetisation.

Beyond the exploration of the high driving field regime, the work presented in this thesis has also led to the derivation and experimental demonstration of how magnetometers based on organic magnetic resonance magnetometry can be utilized for the measurement of magnetic field distributions in the presence of inhomogeneous magnetic fields. Challenges of this measurement approach have been discussed and are attributed to the limited ability to fit experimentally obtained sensor current changes as functions of the applied sensor frequency by expected convolutions of double-Gaussian derivative functions. While inhomogeneities of the magnetic modulation field and the RF driving field are not significantly responsible for this problem, the influence of inductive resonances on the detected spin-dependent current is significant. The existence of inductive resonances within the application spectrum of the RF striplines is unavoidable since a broad band RF spectrum must be applied to sensor striplines. While this poses a significant limitation for the detection of magnetic field distributions, it is of limited detriment for the observation of very subtle magnetic field changes as demonstrated by the detection of subtle changes of the environmental fields. Thus, magnetic resonance based magnetometry using organic semiconductors holds the promise to be developed in truly technologically applicable organic spintronics devices.

# APPENDIX

## PUBLICATIONS BY DAVID P. WATERS

### A.1 List of publications

1. H. Malissa, M. Kavand, **D. P. Waters**, K. J. van Schooten, P. L. Burn, Z. V. Vardeny, B. Saam, J. M. Lupton, C. Boehme, Room-temperature isotopic fingerprinting and nuclear magnetic resonance control of electrical current in an organic light-emitting diode, Science **345**, 6203 (2014).

2. H. Morishita, W. J. Baker, **D. P. Waters**, R. Baarda, J. M. Lupton, C. Boehme, Mechanisms of spin-dependent dark conductivity in films of a soluble fullerene derivative under bipolar injection, Phys. Rev. B **89**, 125311 (2014)

3. W. J. Baker, K. Ambal, **D. P. Waters**, R. Baarda, H. Morishita, K. van Schooten, D. R. McCamey, J. M. Lupton, C. Boehme, Robust absolute magnetometry with organic thin-film devices, Nature Commun. **3**, 898 (2012).

### A.2 Pending manuscripts

1. **D. P. Waters**, G. Joshi, M. Kavand, M.E. Limes, H. Malissa, P. L. Burn, J. M. Lupton, C. Boehme, Room-temperature spin cooperativity in molecular magnetoresistance, (Submitted).

2. **D. P. Waters**, C. Boehme, Organic semiconductor based magnetic resonance magnetometry in presence of gradient magnetic fields, (Pending).

3. K. Ambal, A. Payne, **D. P. Waters**, C. C. Williams, C. Boehme, Synthesis of thin silicon dioxide layers with high E' center densities and investigation of the E' center spin relaxation dynamics for single spin readout applications, *arXiv* **1310**, 94 (2013).

## REFERENCES


[1] D. R. McCamey, K. J. van Schooten, W. J. Baker, S.-Y. Lee, S. Paik, J. M. Lupton, and C. Boehme, Phys. Rev. Lett. **104**, 017601 (2010).

[2] W. J. Baker, T. L. Keevers, J. M. Lupton, D. R. McCamey, and C. Boehme, Phys. Rev. Lett. **108**, 267601 (2012).

[3] W. J. Baker, K. Ambal, D. P. Waters, R. Baarda, H. Morishita, K. J. van Schooten, D. R. McCamey, J. M. Lupton, and C. Boehme, Nat. Commun. **3**, 898 (2012).

[4] R. C. Roundy and M. E. Raikh, Phys. Rev. B **88**, 125206 (2013).

[5] C. J. Wedge, J. C. S. Lau, K.-A. Ferguson, S. A. Norman, P. J. Hore, and C. R. Timmel, Physical Chemistry Chemical Physics **15**, 16043 (2013).

[6] L. E. Hueso, V. Dediu, P. Graziosi, I. Bergenti, A. Riminucci, F. Borgatti, C. Newby, F. Casoli, M. P. de Jong, C. Taliani, and Y. Zhan, Phys. Rev. B **78**, 115203 (2008).

[7] W. Xu, G. J. Szulczewski, P. LeClair, I. Navarrete, R. Schad, G. Miao, H. Guo, and A. Gupta, Applied Physics Letters **90**, 072506 (2007).

[8] D. D. Djayaprawira, D. D. Djayaprawira, K. Tsunekawa, K. Tsunekawa, M. Nagai, M. Nagai, H. Maehara, S. Yamagata, N. Watanabe, S. Yuasa, Y. Suzuki, and K. Ando, Applied Physics Letters **86**, 092502 (2005).

[9] I. Appelbaum, B. Huang, and D. J. Monsma, Nature **447**, 295 (2007).

[10] W. Wagemans, J. Schoonus, P. Lumens, J. Kohlhepp, P. A. Bobbert, H. Swagten, and B. Koopmans, Phys. Rev. Lett. **103**, 146601 (2009).

[11] Z. H. Xiong, D. Wu, Z. V. Vardeny, and J. Shi, Nature **427**, 821 (2004).

[12] M. R. Bennett and J. G. Wright, Physics Letters A **38**, 419 (1972).

[13] H. Yuasa, M. Yoshikawa, Y. Kamiguchi, K. Koi, H. Iwasaki, M. Takagishi, and M. Sahashi, J. Appl. Phys. **92**, 2646 (2002).

[14] N. Sergueev, Q.-F. Sun, H. Guo, B. Wang, and J. Wang, Phys. Rev. B **65**, 165303 (2002).

[15] M. Urdampilleta, S. Klyatskaya, J. P. Cleuziou, and M. Ruben, Nature Materials **10**, 502 (2011).

[16] W. Thomson, Proceedings of the Royal Society of London **8**, 546 (1856).

[17] N. W. Ashcroft and N. D. Mermin, *Solid State Physics*, 1st ed. (Cengage Learning, 1976).

[18] A. Paul, M. Buchmeier, D. E. Bürgler, and P. Grünberg, J. Appl. Phys. **97**, 023910 (2004).

[19] G. Binasch, P. Grünberg, F. Saurenbach, and W. Zinn, Phys. Rev. B **39**, 4828 (1989).

[20] H. Mell and J. Stuke, Journal of Non Crystalline Solids **4**, 304 (1970).

[21] B. Movaghar and L. Schweitzer, Journal of Physics C: Solid State Physics **11**, 125 (1978).

[22] A. Kurobe and H. Kamimura, Journal of Non Crystalline Solids **59-60**, 41 (1983).

[23] K. Klitzing, G. Dorda, and M. Pepper, Phys. Rev. Lett. **45**, 494 (1980).

[24] H. L. Stormer, A. Chang, D. C. Tsui, J. Hwang, A. C. Gossard, and W. Wiegmann, Phys. Rev. Lett. **50**, 1953 (1983).

[25] H. L. Stormer and D. C. Tsui, Science **220**, 1241 (1983).

[26] J. De Boeck, W. Van Roy, J. Das, V. Motsnyi, Z. Liu, L. Lagae, H. Boeve, K. Dessein, and G. Borghs, Semiconductor Science and Technology **17**, 342 (2002).

[27] M. N. Baibich, J. M. Broto, A. Fert, F. N. Van Dau, and F. Petroff, Phys. Rev. Lett. **61**, 2472 (1988).

[28] J. S. Moodera, L. R. Kinder, T. M. Wong, and R. Meservey, Phys. Rev. Lett. **74**, 3273 (1995).

[29] J. M. Daughton, J. Appl. Phys. **81**, 3758 (1997).

[30] J. De Boeck and G. Borghs, Physics World **12**, 27 (1999).

[31] M. Johnson, IEEE Spectrum **37**, 33 (2000).

[32] M. Mallary, A. Torabi, and M. Benakli, IEEE Transactions on Magnetics **38**, 1719 (2002).

[33] S. Baranovski, *Charge Transport in Disordered Solids with Applications in Electronics* (John Wiley & Sons, 2006).

[34] S. Baranovskii, O. Rubel, and P. Thomas, Thin Solid Films **487**, 2 (2005).

[35] P. Hapke, M. Luysberg, R. Carius, and M. Tzolov, Journal of Non Crystalline Solids **198-200**, 927 (1996).

[36] S. Yoshizumi, T. Geballe, M. Kunchur, and W. McLean, Phys. Rev. B **37**, 7094 (1988).

[37] N. A. Asadullayev, N. B. Brandt, S. M. Chudinov, S. N. Kozlov, and I. Ciric, Solid State Communications **61**, 515 (1987).

[38] M. Pope and C. E. Swenberg, *Electronic Processes in Organic Crystals and Polymers* (Oxford University Press, USA, 1999).

[39] A. Schnegg, J. Behrends, M. Fehr, and K. Lips, Physical Chemistry Chemical Physics **14**, 14418 (2012).

[40] K. Morgan and R. Pethig, Nature **213**, 900 (1967).

[41] G. Veeraraghavan, T. D. Nguyen, Y. Sheng, Ö. Mermer, and M. Wohlgenannt, Electron Devices, IEEE Transactions on **54**, 1571 (2007).

[42] S.-T. Pham, Y. Kawasugi, and H. Tada, Applied Physics Letters **103**, 143301 (2013).

[43] P. Desai, W. P. Gillin, P. Shakya, and T. Kreouzis, Phys. Rev. B **76**, 235202 (2007).

[44] J. M. Lupton and C. Boehme, Nature Materials **7**, 598 (2008).

[45] B. Hu and Y. Wu, Nature Materials **6**, 985 (2007).

[46] R. N. Mahato, H. Lülf, M. H. Siekman, S. P. Kersten, P. A. Bobbert, M. P. de Jong, L. De Cola, and W. G. van der Wiel, Science **341**, 257 (2013).

[47] V. A. Dediu, L. E. Hueso, I. Bergenti, and C. Taliani, Nature Materials **8**, 707 (2009).

[48] R. Laiho, S. Majumdar, H. S. Majumdar, and R. Österbacka, Journal of Alloys and Compounds **423**, 169 (2006).

[49] F. J. Wang, C. Yang, Z. V. Vardeny, and X. G. Li, Phys. Rev. B **75**, 245324 (2007).

[50] G. W. Morley, D. R. McCamey, H. A. Seipel, L. C. Brunel, J. van Tol, and C. Boehme, Phys. Rev. Lett. **101**, 207602 (2008).

[51] D. Sun, L. Yin, C. Sun, H. Guo, Z. Gai, X. G. Zhang, and T. Z. Ward, Phys. Rev. Lett. **104**, 236602 (2010).

[52] J.-W. Yoo, H. W. Jang, V. N. Prigodin, C. Kao, C. B. Eom, and A. J. Epstein, Synthetic Metals **160**, 216 (2010).

[53] S. Sanvito, Nature Materials **6**, 803 (2007).

[54] W. J. M. Naber, S. Faez, and W. G. van der Wiel, J. Phys. D: Appl. Phys. **40**, R205 (2007).

[55] C. K. Chiang, C. R. Fincher, Y. W. Park, and A. J. Heeger, Phys. Rev. Lett. **39**, 17 (1977).

[56] H. Shirakawa, E. J. Louis, A. G. MacDiarmid, C. K. Chiang, and A. J. Heeger, in *J. Chem. Soc., Chem. Commun.* (The Royal Society of Chemistry, 1977), pp. 578–580.

[57] H. Okabe, *Photochemistry of Small Molecules* (New York, 1978).

[58] W. Harneit, C. Boehme, S. Schaefer, and K. Huebener, Phys. Rev. Lett. **98**, 216601 (2007).

[59] S. Iijima, Nature **354**, 56 (1991).

[60] S. Iijima and T. Ichihashi, Nature **363**, 603 (1993).

[61] E. Ehrenfreund, A. Devir-Wolfman, B. Khachatryan, B. Gautam, N. Tessler, and Z. V. Vardeny, in *Bulletin of the American Physical Society* (American Physical Society, 2014).

[62] D. R. McCamey, H. A. Seipel, S. Paik, M. J. Walter, J. M. Lupton, N. Borys, and C. Boehme, Nature Materials **7**, 723 (2008).

[63] C. Boehme and J. M. Lupton, Nature Nanotechnology **8**, 612 (2013).

[64] G. Salis, S. Alvarado, M. Tschudy, T. Brunschwiler, and R. Allenspach, Phys. Rev. B **70**, 085203 (2004).

[65] W. Wagemans, F. L. Bloom, M. Kemerink, and B. Koopmans, Phys. Rev. Lett. **103**, 066601 (2009).

[66] J. S. Jiang, J. E. Pearson, and S. Bader, Phys. Rev. B **77**, 035303 (2008).

[67] W. Wagemans and B. Koopmans, Phys. Stat. Sol. (B) **248**, 1029 (2010).

[68] N. Tombros, C. Jozsa, M. Popinciuc, H. T. Jonkman, and B. J. van Wees, Nature **448**, 571 (2007).

[69] P. A. Bobbert, T. D. Nguyen, F. W. A. van Oost, B. Koopmans, and M. Wohlgenannt, Phys. Rev. Lett. **99**, 216801 (2007).

[70] A. Riminucci, M. Prezioso, C. Pernechele, P. Graziosi, I. Bergenti, R. Cecchini, M. Calbucci, M. Solzi, and V. Alek Dediu, Applied Physics Letters **102**, 092407 (2013).

[71] P. A. Bobbert, W. Wagemans, F. W. A. van Oost, B. Koopmans, and M. Wohlgenannt, Phys. Rev. Lett. **102**, 156604 (2009).

[72] M. Reufer, M. J. Walter, P. G. Lagoudakis, A. B. Hummel, J. S. Kolb, H. G. Roskos, U. Scherf, and J. M. Lupton, Nature Materials **4**, 340 (2005).

[73] S. Pramanik, C. G. Stefanita, S. Patibandla, S. Bandyopadhyay, K. Garre, N. Harth, and M. Cahay, Nature Nanotechnology **2**, 216 (2007).

[74] C. Boehme, Dynamics of Spin-Dependent Charge Carrier Recombination, 2002.

[75] J. Bergeson, A. J. Epstein, V. N. Prigodin, and D. Lincoln, Phys. Rev. Lett. **100**, 067201 (2008).

[76] J. Kalinowski, M. Cocchi, D. Virgili, P. Di Marco, and V. Fattori, Chemical Physics Letters **380**, 710 (2003).

[77] H. Odaka, Y. Okimoto, T. Yamada, H. Okamoto, M. Kawasaki, and Y. Tokura, Applied Physics Letters **88**, 123501 (2006).

[78] Y. Iwasaki, T. Osasa, M. Asahi, and M. Matsumura, Phys. Rev. B **74**, 195209 (2006).

[79] Y. Wu, Z. Xu, B. Hu, and J. Howe, Phys. Rev. B **75**, 035214 (2007).

[80] E. L. Frankevich, I. A. Sokolik, A. A. Lymarev, F. E. Karasz, S. Blumstengel, R. Baughman, and H. Hörhold, Phys. Rev. B **46**, 9320 (1992).

[81] U. Scherf, G. Veeraraghavan, T. D. Nguyen, Y. Sheng, M. Wohlgenannt, Ö. Mermer, and S. Qiu, Phys. Rev. B **74**, 045213 (2006).

[82] A. J. Epstein, V. N. Prigodin, J. Bergeson, and D. M. Lincoln, Synthetic Metals **156**, 757 (2006).

[83] S. A. Bagnich, U. Niedermeier, C. Melzer, W. Sarfert, and H. von Seggern, J. Appl. Phys. **106**, 113702 (2009).

[84] V. N. Prigodin and A. J. Epstein, Synthetic Metals **160**, 244 (2010).

[85] J. L. Martin, J. Bergeson, V. N. Prigodin, and A. J. Epstein, Synthetic Metals **160**, 291 (2010).

[86] M. Wohlgenannt, W. Wagemans, P. A. Bobbert, F. L. Bloom, and B. Koopmans, J. Appl. Phys. **103**, 07 (2008).

[87] J. Behrends, A. Schnegg, K. Lips, E. A. Thomsen, A. K. Pankey, I. D. W. Samuel, and D. J. Keeble, Phys. Rev. Lett. **105**, 176601 (2010).

[88] P. Desai, P. Shakya, T. Kreouzis, W. P. Gillin, and N. A. Morley, Phys. Rev. B **75**, 094423 (2007).

[89] M. K. Lee, M. Segal, Z. Soos, J. Shinar, and M. Baldo, Phys. Rev. Lett. **94**, 137403 (2005).

[90] Z. V. Vardeny, E. Ehrenfreund, J. Shinar, and F. Wudl, Phys. Rev. B **35**, 2498 (1987).

[91] L. S. Swanson, P. Lane, Q. Ni, J. Shinar, J. Engel, T. Barton, and L. Jones, Phys. Rev. Lett. **68**, 887 (1992).

[92] V. Dyakonov, G. Rosler, M. Schwoerer, S. Blumstengel, and K. Luders, J. Appl. Phys. **79**, 1556 (1996).

[93] I. Hiromitsu, Y. Kaimori, and T. Ito, Solid State Communications **104**, 511 (1997).

[94] T. Eickelkamp, S. Roth, and M. Mehring, Molecular Physics: an International Journal at the Interface Between Chemistry and Physics **95**, 967 (1998).

[95] I. Hiromitsu, Y. Kaimori, M. Kitano, and T. Ito, Phys. Rev. B **59**, 2151 (1999).

[96] K. Murata, Y. Shimoi, S. Abe, T. Noguchi, and T. Ohnishi, Synthetic Metals **101**, 353 (1999).

[97] G. B. Silva, L. F. Santos, R. M. Faria, and C. F. O. Graeff, Physica B: Condensed Matter **308-310**, 1078 (2001).

[98] F. A. Castro, G. B. Silva, L. F. Santos, R. M. Faria, F. Nüesch, L. Zuppiroli, and C. F. O. Graeff, Journal of Non Crystalline Solids **338-340**, 622 (2004).

[99] C. Yang, E. Ehrenfreund, and Z. V. Vardeny, Phys. Rev. Lett. **99**, 157401 (2007).

[100] L. S. Swanson, J. Shinar, A. R. Brown, D. Bradley, R. Friend, P. L. Burn, A. Kraft, and A. B. Holmes, Phys. Rev. B **46**, 15072 (1992).

[101] M. Wohlgenannt, W. Graupner, G. Leising, and Z. V. Vardeny, Phys. Rev. Lett. **82**, 3344 (1999).

[102] V. Dyakonov, G. Rosler, M. Schwoerer, and E. L. Frankevich, Phys. Rev. B **56**, 3852 (1997).

[103] J. Shinar, Laser & Photonics Reviews **6**, 767 (2012).

[104] T. H. Nguyen, G. Mahieu, M. Berthe, B. Grandidier, C. Delerue, D. Stiévenard, and P. Ebert, Phys. Rev. Lett. **105**, 226404 (2010).

[105] Z. V. Vardeny, T. D. Nguyen, G. Hukic-Markosian, F. J. Wang, L. Wojcik, X.-G. Li, and E. Ehrenfreund, Nature Materials **9**, 345 (2010).

[106] W. J. Baker, D. R. McCamey, K. J. van Schooten, J. M. Lupton, and C. Boehme, Phys. Rev. B **84**, 165205 (2011).

[107] H. Morishita, W. J. Baker, D. P. Waters, R. Baarda, J. M. Lupton, and C. Boehme, Phys. Rev. B **89**, 125311 (2014).

[108] S.-Y. Lee, D. R. McCamey, S. Paik, J. Yu, P. L. Burn, J. M. Lupton, and C. Boehme, J. Am. Chem. Soc. **133**, 2019 (2011).

[109] W. J. Baker, Coherently Controlled Spin-Dependent Charge Carrier Transitions in Organic Semiconductors: Properties and Applications, PhD, University of Utah 2012.

[110] J. L. Brédas, D. Beljonne, V. Coropceanu, and J. Cornil, Chemical Reviews **104**, 4971−5003 (2004).

[111] P. Vukusic, B. Hallam, and J. Noyes, Science **315**, 348 (2007).

[112] S. Günes, H. Neugebauer, and N. S. Sariciftci, Chemical Reviews **107**, 1324 (2007).

[113] S. E. Shaheen, C. J. Brabec, N. S. Sariciftci, F. Padinger, T. Fromherz, and J. C. Hummelen, Applied Physics Letters **78**, 841 (2001).

[114] G. Horowitz, Adv. Mater. **10**, 365 (1998).

[115] H. Sirringhaus, Adv. Mater. **17**, 2411 (2005).

[116] D. R. Baigent, R. N. Marks, N. C. Greenham, R. H. Friend, S. C. Moratti, and A. B. Holmes, Applied Physics Letters **65**, 2636 (1994).

[117] J. H. Burroughes, D. Bradley, A. R. Brown, and R. N. Marks, Nature **347**, 539 (1990).

[118] H. Sirringhaus, N. Tessler, and R. H. Friend, Science **280**, 1741 (1998).

[119] G. Silva, L. Santos, R. Faria, and C. F. O. Graeff, Mat. Res. Soc. Symp. Proc. **725**, 105 (2002).

[120] C. J. Neef and J. P. Ferraris, Macromolecules **2000**, 2311 (2000).

[121] D. Braun and A. J. Heeger, Applied Physics Letters **58**, 1982 (1991).

[122] D. R. McCamey, S.-Y. Lee, S. Paik, J. M. Lupton, and C. Boehme, Phys. Rev. B **82**, 125206 (2010).

[123] J. C. Scott, J. H. Kaufman, P. J. Brock, R. DiPietro, J. Salem, and J. A. Goitia, J. Appl. Phys. **79**, 2745 (1996).

[124] J. Liu, T.-F. Guo, and Y. Yang, J. Appl. Phys. **91**, 1595 (2002).

[125] M. Jørgensen, K. Norrman, and F. C. Krebs, Solar Energy Materials and Solar Cells **92**, 686 (2008).

[126] A. Kitai, *Principles of Solar Cells, LEDs and Diodes* (John Wiley & Sons, 2011).

[127] P. F. Weller, J. Chem. Educ. **44**, 391 (1967).

[128] C. Kittel, *Introduction to Solid State Physics* (John Wiley & Sons, 2005).

[129] N. M. Atherton, *Electron Spin Resonance* (Halsted Press, 1973).

[130] R. A. Street, *Hydrogenated Amorphous Silicon* (Cambridge University Press, 1991).

[131] J. Gray, *Handbook of Photovoltaic Science and Engineering* (John Wiley & Sons, Ltd, 2011).

[132] U. E. Steiner and T. Ulrich, Chemical Reviews **89**, 51 (2002).

[133] E. Frankevich, H. Ishii, Y. Hamanaka, T. Yokoyama, A. Fuji, S. Li, K. Yoshino, A. Nakamura, and K. Seki, Phys. Rev. B **62**, 2505 (2000).

[134] E. L. Frankevich, I. A. Sokolik, and D. I. Kadyrov, Soviet Journal of Experimental and Theoretical Physics Letters **36**, 486 (1982).

[135] W. Wagemans, P. Janssen, E. H. M. van der Heijden, M. Kemerink, and B. Koopmans, Applied Physics Letters **97**, 123301 (2010).

[136] S. Majumdar, H. S. Majumdar, H. Aarnio, H. Aarnio, D. Vanderzande, D. Vanderzande, R. Laiho, and R. Österbacka, Phys. Rev. B **79**, 201202 (2009).

[137] R. C. Roundy, Z. V. Vardeny, and M. E. Raikh, Phys. Rev. B **88**, 075207 (2013).

[138] R. C. Roundy and M. E. Raikh, Phys. Rev. B **87**, 195206 (2013).

[139] X. X. Li, X. F. Dong, J. Lei, S. J. Xie, and A. Saxena, Applied Physics Letters **100**, 142408 (2012).

[140] N. J. Harmon and M. E. Flatté, Phys. Rev. B **85**, 075204 (2012).

[141] D. Kaplan, I. Solomon, and N. F. Mott, J. Phyique Lett. **39**, 51 (1978).

[142] D. Lepine, Phys. Rev. B **6**, 436 (1972).

[143] H. Morishita, W. J. Baker, D. P. Waters, R. Baarda, J. M. Lupton, and C. Boehme, Phys. Rev. B **89**, 125311 (2014).

[144] V. Ern and R. E. Merrifield, Phys. Rev. Lett. **21**, 609 (1968).

[145] Y. Meng, X. J. Liu, B. Di, and Z. An, The Journal of Chemical Physics **131**, 244502 (2009).

[146] F. J. Wang, Z. V. Vardeny, and H. Bässler, Phys. Rev. Lett. **101**, 236805 (2008).

[147] A. V. Astashkin and A. Schweiger, **174**, 595 (1990).

[148] C. Michel, C. Boehme, K. Lips, S. Baranovskii, A. Gliesche, and F. Gebhard, Phys. Rev. B **79**, 052201 (2009).

[149] R. Glenn, W. J. Baker, C. Boehme, and M. E. Raikh, Phys. Rev. B **87**, 155208 (2013).

[150] C. Boehme and K. Lips, Journal of Materials Science: Materials in Electronics **18**, 285 (2007).

[151] A. Gliesche, C. Michel, V. Rajevac, and K. Lips, Phys. Rev. B **77**, 245206 (2008).

[152] A. R. Stegner, C. Boehme, H. Huebl, M. Stutzmann, K. Lips, and M. S. Brandt, Nature Physics **2**, 835 (2006).

[153] D. R. McCamey, S.-Y. Lee, T. W. Herring, P. C. Taylor, K. Lips, J. Hu, F. Zhu, A. Madan, and C. Boehme, Phys. Rev. B **79**, 195205 (2009).

[154] M. E. Limes, J. Wang, W. J. Baker, S.-Y. Lee, B. Saam, and C. Boehme, Phys. Rev. B **87**, 165204 (2012).

[155] C. Boehme, D. R. McCamey, K. J. van Schooten, W. J. Baker, S.-Y. Lee, S. Paik, and J. M. Lupton, Phys. Status Solidi B **246**, 2750 (2009).

[156] CODATA values of the fundamental constants, http://physics.nist.gov/cuu/Constants/index.html.

[157] C. Boehme and K. Lips, Phys. Rev. B **68**, 245105 (2003).

[158] W. Heisenberg, Z. Physik **38**, 411 (1926).

[159] P. A. M. Dirac, Proceedings of the Royal Society of London. Series a, Containing Papers of a Mathematical and Physical Character **112**, 661 (1926).

[160] T. D. Nguyen, Y. Sheng, J. Rybicki, G. Veeraraghavan, and M. Wohlgenannt, Journal of Materials Chemistry **17**, 1995 (2007).

[161] C. J. Cochrane, P. M. Lenahan, and A. J. Lelis, J. Appl. Phys. **109**, 014506 (2011).

[162] W. Akhtar, V. Filidou, T. Sekiguchi, E. Kawakami, T. Itahashi, L. Vlasenko, J. J. L. Morton, and K. M. Itoh, Phys. Rev. Lett. **108**, 097601 (2012).

[163] K. Saeedi, S. Simmons, J. Z. Salvail, P. Dluhy, H. Riemann, N. V. Abrosimov, P. Becker, H.-J. Pohl, J. J. L. Morton, and M. L. W. Thewalt, Science **342**, 830 (2013).

[164] M. Steger, K. Saeedi, M. L. W. Thewalt, J. J. L. Morton, H. Riemann, N. V. Abrosimov, P. Becker, and H. J. Pohl, Science **336**, 1280 (2012).

[165] M. S. Brandt, M. Bayerl, M. Stutzmann, and C. F. O. Graeff, Journal of Non Crystalline Solids **227**, 343 (1998).

[166] C. Boehme and K. Lips, Physica Status Solidi(C) **1**, 1255 (2004).

[167] M. Xiao, I. Martin, E. Yablonovitch, and H. W. Jiang, Nature **430**, 435 (2004).

[168] A. Morello, J. Pla, F. Zwanenburg, K. Chan, K. Tan, H. Huebl, M. Möttönen, C. D. Nugroho, C. Yang, and J. van Donkelaar, Nature **467**, 687 (2010).

[169] M. Stutzmann, M. S. Brandt, and M. Bayerl, Journal of Non Crystalline Solids **266**, 1 (2000).

[170] D. Rugar, R. Budakian, H. J. Mamin, and B. W. Chui, Nature **430**, 329 (2004).

[171] J. Köhler, J. A. J. M. Disselhorst, M. C. J. M. Donckers, E. J. J. Groenen, J. Schmidt, and W. E. Moerner, Nature **363**, 242 (1993).

[172] J. Wrachtrup, C. Von Borczyskowski, J. Bernard, M. Orritt, and R. Brown, Nature **363**, 244 (1993).

[173] R. Maxwell and A. Honig, Phys. Rev. Lett. **17**, 188 (1966).

[174] S.-Y. Lee, Pulsed electrically and optically detected magnetic resonance spectroscopy of disordered semiconductors, PhD, University of Utah, 2011.

[175] R. Glenn, M. E. Limes, B. Saam, C. Boehme, and M. E. Raikh, Phys. Rev. B **87**, 165205 (2013).

[176] C. Boehme and K. Lips, Applied Physics Letters **79**, 4363 (2001).

[177] C. Boehme, P. Kanschat, and K. Lips, Nuclear Inst. and Methods in Physics Research, B **186**, 30 (2002).

[178] C. Boehme and G. Lucovsky, Journal of Non Crystalline Solids **299-302**, 1157 (2002).

[179] Z. V. Vardeny, *Organic Spintronics* (CRC Press Llc, 2010).

[180] D. R. McCamey, S. Paik, S.-Y. Lee, and C. Boehme, Phys. Rev. B **86**, 115204 (2012).

[181] D. J. Griffiths, *Introduction to Electrodynamics* (Prentice Hall, 1999).

[182] Jackson, *Classical Electrodynamics, 3rd Ed* (John Wiley & Sons, 2007).

[183] T. D. Nguyen, M. Wohlgenannt, T. L. Francis, G. Veeraraghavan, Ö. Mermer, Y. Sheng, A. Köhler, M. Al-Suti, and M. Khan, Phys. Rev. B **72**, 205202 (2005).

[184] R. H. Dicke, Phys. Rev. Lett. **93**, 99 (1954).

[185] M. Stutzmann and M. S. Brandt, Journal of Non Crystalline Solids **141**, 97 (1992).

[186] M. Stutzmann and M. S. Brandt, Phys. Stat. Sol. (B) **190**, 97 (1995).

[187] A. Schweiger and G. Jeschke, *Principles of Pulse Electron Paramagnetic Resonance* (Oxford University Press on Demand, 2001).

[188] M. Gross and S. Haroche, Physics Reports **93**, 301 (1982).

[189] D. S. Wiersma, P. Bartolini, A. Lagendijk, and R. Righini, Nature **390**, 671 (1997).

[190] D. S. Wiersma, Nature Physics **4**, 359 (2008).

[191] G. Günter, A. A. Anappara, J. Hees, A. Sell, G. Biasiol, L. Sorba, S. De Liberato, C. Ciuti, A. Tredicucci, A. Leitenstorfer, and R. Huber, Nature **458**, 178 (2009).

[192] K. Schulten, H. Staerk, A. Weller, H. J. Werner, and B. Nickel, Zeitschrift Für Physikalische Chemie **101**, 371 (1976).

[193] H. J. Hogben, T. Biskup, and P. J. Hore, Phys. Rev. Lett. **109**, 220501 (2012).

[194] E. M. Gauger, E. Rieper, J. J. L. Morton, S. C. Benjamin, and V. Vedral, Phys. Rev. Lett. **106**, 040503 (2011).

[195] T. D. Nguyen, B. R. Gautam, E. Ehrenfreund, and Z. V. Vardeny, Phys. Rev. Lett. **105**, 166804 (2010).

[196] E. L. Frankevich, A. I. Pristupa, and V. M. Kobryanskiĭ, Soviet Journal of Experimental and Theoretical Physics Letters **40**, 733 (1984).

[197] M. Wohlgenannt, K. Tandon, S. Mazumdar, S. Ramasesha, and Z. V. Vardeny, Nature **409**, 494 (2001).

[198] J. R. Woodward, C. R. Timmel, K. A. McLauchlan, and P. J. Hore, Phys. Rev. Lett. **87**, 077602 (2001).

[199] Kevin B Henbest, Philipp Kukura, Christopher T Rodgers, A. P J Hore, and C. R. Timmel, J. Am. Chem. Soc. **126**, 8102 (2004).

[200] G. Veeraraghavan, M. Wohlgenannt, T. L. Francis, and Ö. Mermer, New J. Phys. **6**, 185 (2004).

[201] A. R. B. M. Yusoff, W. J. da Silva, J. P. M. Serbena, M. S. Meruvia, and I. A. Hummelgen, Applied Physics Letters **94**, 253305 (2009).

[202] C. Reig, M.-D. Cubells-Beltrán, and D. Ramírez, Sensors **9**, 7919 (2009).

[203] M. Tondra, J. M. Daughton, D. Wang, R. S. Beech, A. Fink, and J. A. Taylor, J. Appl. Phys. **83**, 6688 (1998).

[204] L. T. Hall, J. H. Cole, C. D. Hill, and L. C. L. Hollenberg, Phys. Rev. Lett. **103**, 220802 (2009).

[205] A. Cooper, E. Magesan, H. N. Yum, and P. Cappellaro, Nat. Commun. **5**, 3141 (2014).

[206] U. S. Geomagnetism program, *geomag.usgs.gov* (2014).

[207] J. Petta, A. Johnson, J. Taylor, E. Laird, A. Yacoby, M. Lukin, C. Marcus, M. Hanson, and A. C. Gossard, Science **309**, 2180 (2005).